

**MRes in Railway Systems Integration**

**College of Engineering, School of Civil Engineering**

**University of Birmingham**



**Structural Health Condition Monitoring  
of Rails Using Acoustic Emission  
Techniques**

Pinar Yilmazer

September 2012

Supervised by Dr. Mayorkinos Papaalias

Dissertation submitted in partial fulfilment of the requirements for  
the award of MRes in Railway Systems Integration

UNIVERSITY OF  
BIRMINGHAM

**University of Birmingham Research Archive**

**e-theses repository**

This unpublished thesis/dissertation is copyright of the author and/or third parties. The intellectual property rights of the author or third parties in respect of this work are as defined by The Copyright Designs and Patents Act 1988 or as modified by any successor legislation.

Any use made of information contained in this thesis/dissertation must be in accordance with that legislation and must be properly acknowledged. Further distribution or reproduction in any format is prohibited without the permission of the copyright holder.

## **Declaration and Copyright Statement**

---

I declare that no portion of the work referred to in the thesis has been submitted in support of an application for another degree or qualification of this or any other university or other institute of learning.

The following three notes on copyright and the ownership of intellectual property rights:

- I. Copyright in text of this dissertation rests with the author. Copies (by any process) either in full, or of extracts, may be made only in accordance with instructions given by the author. Details may be obtained from the appropriate Graduate Office. This page must form part of any such copies made. Further copies (by any process) of copies made in accordance with such instructions may not be made without the permission (in writing) of the author.
  
- II. The ownership of any intellectual property rights which may be described in this thesis is vested in University of Birmingham subject to any prior agreement to the contrary, and may not be made available for use by third parties without the written permission of the University, which will prescribe the terms and conditions of any such agreement.
  
- III. Further information on the conditions under which disclosures and exploitation may take place is available from the Head of School of Civil Engineering.

## Acknowledgement

---

I would like to acknowledge the support and encouragement given by Dr. Mayorkinos Papaelias. His support and guidance have allowed me to complete successfully this arduous research and degree.

I am extremely grateful to Prof. Felix Schmid and Mrs Joy Grey for their helpful suggestions and support throughout the year.

I would like to thank Mr. David Price and Mr Tim Dole for their help in using the fatigue machines. I am thankful to Mr Hamed Rowshandel and Mr Adnan Zentani for their help with the tests using the motorised rail trolley.

I would also like to acknowledge the financial support by Turkish State Railway Administration (T.C.D.D) and the Birmingham Centre for Railway Research and Education. I am indebted to T.C.D.D for giving me the opportunity to study at the University of Birmingham.

Finally, I am truly thankful to my family and Michael who have always been very supportive of all my endeavours.

## Executive Summary

---

In-service rails can develop several types of structural defects due to fatigue and wear caused by rolling stock passing over them. Most rail defects will develop gradually over time thus permitting inspection engineers to detect them in time before final failure occurs. If rail defects remain undetected they will continue to grow until they reach a critical size leading to the sudden fracture of the rail section affected. Rail defects, once detected, are not immediately removed from the rail network. The maintenance action type, level and timescale depends on the severity of the defect detected, its location and type of rail line concerned (i.e. freight, high-speed, etc.). In the UK, certain types of severe rail defects such as tache ovals, require the fitting of emergency clamps and the imposition of an Emergency Speed Restriction (ESR) until the defects are removed.

It is generally believed that by fitting emergency clamps on certain types of defects and imposing a 20MPH ESR then the defect should stop growing until the affected rail section is removed from service. Unfortunately, there is no way to prove that these defects are not actually growing further after the clamps have been fitted. Moreover, there have been occasional reports, although only very few that clamped defective rails did fracture before the maintenance engineers had been able to complete the renewal of the affected section. However, such incidences where failure has actually occurred after the emergency clamps were fitted have largely been attributed to incorrect evaluation of the actual criticality of the defect detected. If it can be proven that no crack growth takes place after the emergency clamps are fitted on the defective rail section, then the ESR could be potentially raised to 50MPH or even more minimising delays on the rail network.

Acoustic emission (AE) techniques can be applied for the detection and continuous monitoring of defect growth therefore removing the need of imposing strict ESRs. The work reported herewith aims to develop a sound methodology for the application of AE in order to detect and subsequently monitor damage evolution in rails. To validate the potential of the AE technique, tests have been carried out under laboratory conditions on three and four-point bending samples manufactured from 260 grade rail steel. Further tests, simulating the background noise conditions caused by passing rolling stock have been carried out using special experimental setups. The crack growth events have been simulated using a pencil tip break.

# Table of Contents

---

<b>Declaration and Copyright Statement</b> .....	<b>i</b>
<b>Acknowledgement</b> .....	<b>ii</b>
<b>Executive Summary</b> .....	<b>iii</b>
<b>Table of Contents</b> .....	<b>iv</b>
<b>List of Figures</b> .....	<b>vi</b>
<b>List of Tables</b> .....	<b>ix</b>
<b>List of Abbreviations</b> .....	<b>x</b>
<b>1 Introduction</b> .....	<b>1</b>
<b>2 Rail metallurgy, defects and inspection techniques</b> .....	<b>5</b>
2.1 Rail steels .....	5
2.2 Defects in rails .....	6
2.3 Non-destructive testing (NDT) .....	10
<b>3 Fracture and fatigue</b> .....	<b>15</b>
3.1 Elastic and plastic deformation .....	15
3.2 Bending test.....	16
3.3 Fracture mechanism .....	17
3.3.1 Basic fracture modes .....	17
3.3.2 Fatigue fracture.....	24
3.4 Effect of stress ratio (R).....	29
3.5 The effect of the fatigue crack propagation curve .....	30
3.5.1 Region 1 - Threshold .....	30
3.5.2 Region 2 - Paris Regime .....	31
3.5.3 Region 3 - Fracture .....	31
3.6 Energy balance approach .....	32
<b>4 Acoustic Emission (AE) Technique</b> .....	<b>33</b>
4.1 AE method .....	33
4.2 Deformation process and AE method .....	35
4.3 Acoustic emission and crack monitoring in rails .....	36
4.4 Kaiser effect .....	37
4.5 Comparison between AE and other NDT techniques .....	40
4.6 Waveform analysis methods of AE signals .....	41

<b>5</b>	<b>Three-point and four-point bending tests .....</b>	<b>43</b>
5.1	Experimental method and results .....	43
5.2	Pre-cracking method .....	44
5.3	Three-point and Four-point bending test set up .....	47
5.4	AE setup .....	52
5.5	Three-point bending test result .....	54
5.6	Four-point bending test result .....	62
<b>6</b>	<b>Experiments under simulated field conditions .....</b>	<b>71</b>
6.1	Experimental setup .....	71
6.2	Manual inspection .....	72
6.3	Simulated trials using a motorised trolley .....	76
<b>7</b>	<b>Conclusions and future work .....</b>	<b>79</b>
7.1	Word Count .....	81
	<b>References.....</b>	<b>82</b>
	<b>Website Links.....</b>	<b>84</b>

## List of Figures

---

Figure 1 Head checks defect on the rail head surface due to rolling contact fatigue. ....	7
Figure 2 Typical locations of defect in rails(University of Birmingham, 2007; Hocking NDT Ltd, 2012).....	7
Figure 3 Typical service defects which are originating from the surface in rail (Hocking NDT Ltd, 2012).....	9
Figure 4 Trolley mounted crack detection method(Hocking NDT Ltd, 2012) .....	11
Figure 5 EMAT inspection system for automated rail inspection mounted on a hi-rail vehicle(University of Birmingham, 2007).....	12
Figure 6 Schematic showing the principle of MFL inspection(University of Birmingham, 2007).....	13
Figure 7 Hooke's Law (Cyberphysics, Unknown) .....	15
Figure 8 Fatigue Test Specimen (left) and Bending Machine (right) (Texas Tech University, 2012).....	16
Figure 9 $\sigma$ - $\epsilon$ curve for brittle and ductile fracture mode (DoITPoMS, 2008).....	18
Figure 10 Crack propagation mechanisms (Callister, 2006).....	18
Figure 11 Scanning electron fractographs of ductile inter-granular and trans-granular fracture modes (Anderson, 1995).....	19
Figure 12 Ductile fracture stages: a) Initial necking. (b) Small cavity formation. (c) Coalescence of cavities to form a crack. (d) Crack propagation. (e) Final shear fracture at an angle relative to the tensile direction.(Callister, 2006).....	20
Figure 13 Microstructure of Brittle Fracture Mechanism(Anderson, 1995) .....	21
Figure 14 Cup-and-cone (ductile) fracture and Brittle fracture(Anderson, 1995) .....	21
Figure 15 Energy changes associated with incremental crack extension(Roylance, 2001) .....	22
Figure 16 The relationship between energy rates and crack length(James, 2001) .....	23
Figure 17 The modes of crack surface displacement(Ewalds & Wanhill, 1989).....	24
Figure 18 Typical S-N Curves for Ferrous and Nonferrous Metals(Ewalds & Wanhill, 1989).....	25
Figure 19 The external load versus crack length (Labossiere, Flores, & Vant, 2007) .....	26
Figure 20 The relationship between the crack length and number of cycles (James, 2001).....	27
Figure 21 The relationship between the maximum stress and the number of cycles to failure depending on the R-ratio(Pereira, Jesus, Ribeiro, & Fernandes, 2008).....	29

Figure 22 Scheme of the typical fatigue crack propagation curve (Ewalds & Wanhill, 1989) .....	30
Figure 23 Effect of fracture toughness on the governing failure mechanism. (Anderson, 1995).....	32
Figure 24 Principle of AE technique (NDT Education Resource Center, 2001-2012).....	33
Figure 25 Main features of an AE hit (Huang, Jiang, Liaw, Brooks, Seeley, & Klarstrom, 1998).....	34
Figure 26 AE system architecture(Husin, Mba, & Hamzah, 2010) .....	35
Figure 27 Application of acoustic emission for the detection and monitoring of crack initiation and crack growth in an in-service rail. ....	37
Figure 28 Illustration of Kaiser Effect (Puri, 2003) .....	38
Figure 29 An example of a cumulative acoustic emission curve, Region A–B represents the closing of cracks, and B–C the linear elastic deformation. C–D is the stable, and D–F the unstable fracture propagation(Lehtonen, Cosgrove, Hudson, & Johansson, 2012) .....	39
Figure 30 Kaiser Effect and Felicity Effect in a cyclically loaded specimen(Lehtonen, Cosgrove, Hudson, & Johansson, 2012; Pollock, 2003) .....	40
Figure 31 Transient (top) and continuous (bottom) type of AE signal(Vallen Systeme GmbH, 2002).....	42
Figure 32 Specimen extraction for flexural testing .....	43
Figure 33 The microstructure of the rail tested showing ferrite and pearlite (etched using 1% Nital). ....	44
Figure 34 Schematic image of the single centred notch specimen.....	45
Figure 35 Experimental configuration of Vibrophore machine .....	46
Figure 36 Schematic image of the pre-cracked notch specimen .....	48
Figure 37 Four-point bending test using trapezoidal loading cycle .....	48
Figure 38 Experimental configuration for three and four point bending test.....	49
Figure 39 Experimental configuration of Dartec 50 kN servo-hydraulic universal test machine.....	52
Figure 40 AE hit amplitude versus time and associated burst type waveforms .....	55
Figure 41 Cumulative number of hits with amplitude.....	56
Figure 42 Cumulative number of hits recorded with time for the duration of the test.....	56
Figure 43 Duration of hits with time .....	57

Figure 44 Counts per hit with time.....	57
Figure 45 Cumulative number of hits with respect of hit amplitude per sensor .....	58
Figure 46 Amplitude of recorded AE hit with time per sensor .....	58
Figure 47 Hit amplitude and hit duration with test time per sensor .....	59
Figure 48 Density of AE hits with time.....	59
Figure 49 Hit rise time with test time for both sensors .....	60
Figure 50 Crack propagation rate depending on the number of cycles for 3- point bending test.....	60
Figure 51 Amplitude versus time diagram. Bottom burst-type waveforms detected above 40dB related to crack growth events .....	62
Figure 52 Number of AE vector hits recorded versus time.....	63
Figure 53 Replica micrograph showing the crack length at 750 cycles .....	63
Figure 54 Distribution of number of vector hits versus amplitude .....	64
Figure 55 Density of AE hits with test time.....	64
Figure 56 Hit duration versus time.....	65
Figure 57 Hit duration with hit amplitude.....	65
Figure 58 Counts to peak versus hit amplitude .....	66
Figure 59 Hit peak frequency with test time .....	66
Figure 60 Hit amplitude and hit duration with test time per sensor .....	67
Figure 61 Images of the fractured surface of a four point bending sample.....	67
Figure 62 Amplitude with time for overloaded four point bending sample.....	68
Figure 63 Distribution of hits with amplitude per sensor for rapidly broken four point bending sample.....	68
Figure 64 Hit amplitude and duration with test time per sensor .....	69
Figure 65 Hit peak frequency with test time .....	69
Figure 66 Hit duration with test time for rapidly broken four point bending sample .....	70
Figure 67 Experimental configuration for simulated AE tests .....	71
Figure 68 Simplified schematic showing the test concept. ....	72
Figure 69 Equipments used in experiment .....	72
Figure 70 Raw AE waveform associated with rolling noise and moving RMS.....	73

Figure 71 The indication of the second experimental technique at the laboratory conditions .....	74
Figure 72 Raw AE signal from a pencil break and associated RMS.....	74
Figure 73 Repetition test with rolling noise present. The pencil break simulating the crack growth event is clearly visible .....	75
Figure 74 Contaminated signal from occasional contact of the wheel flange giving rise to occasional high amplitude peaks that resemble the one arising from the pencil break... The pencil break is visible at 2.1s.....	76
Figure 75 Experimental configuration on the test rail track at University of Birmingham	77
Figure 76 Raw AE signal and RMS with clearly visible pencil break event simulating a crack growth event. Gain is set at 58dB .....	77
Figure 77 FFT of the raw AE signal arising from the pencil break event .....	78
Figure 78 Raw AE signal with pencil break showing at 7.5s during automatic movement of the trolley.....	78

## List of Tables

---

Table 1 Typical chemical composition of pearlite rail steels (Vitez, Krumes, & Vitez, 2004; Mesteel, Unknown) .....	5
Table 2 Fracture mechanisms and their surface characteristics(The University of Southern Mississippi, 2001).....	25
Table 3 Characteristics of acoustic emission inspection compared with other inspection methods(Pollock, 2003).....	41
Table 4 Typical requirement of mechanical properties(Vitez, Krumes, & Vitez, 2004; Mesteel, Unknown) .....	43
Table 5 The bearable fatigue loads of single centred notch rail specimen.....	47
Table 6 Applied cyclic loading range for the 3 and 4-point bending tests.....	53
Table 7 Characteristics of hits with increasing amplitude.....	61

## List of Abbreviations

---

A glossary is sorted alphabetically:

<b>Term</b>	<b>Explanation / Meaning / Definition</b>
$\Delta K$	The stress intensity factor
a	The fatigue crack growth length
AE	Acoustic emission
ASTM	American society for testing and materials
EMATs	Electromagnetic acoustic transducers
ESR	Emergency speed restriction
G	Strain energy release rate
$G_C$	Toughness or critical value of strain energy release rate
GE	Griffith energy
HLT	Hit lockout time
K	Stress intensity factor
$K_C$	Fracture toughness or critical stress intensity release factor
MFL	Magnetic flux leakage
MPI	Magnetic particle inspection
N	Cycles of failure
NDT	Non-destructive testing
NR	Network rail
PDT	The peak definition time
R	Effect of stress ratio
RCF	Rolling contact fatigue
RMS	Root mean square
S	Surface energy
SCC	Stress corrosion cracking
SEM	Scanning electron microscope
U	Absorbed energy
UIC	International union of railways is in french "union internationale des chemins de fer",
UIC60	Derives its name from the specified weight of $60 \text{ kg m}^{-1}$
UT	Ultrasonic testing
W	Expended energy

# 1 Introduction

## Background

At global scale, rail networks are gradually getting busier with rolling stock travelling at higher speeds and carrying heavier axle loads than ever before. In the UK, Network Rail manages one of the largest and busiest rail networks in Europe as well as in the world. (International Union of Railways (UIC), 2011) This means that the rolling stock density within the UK rail network is one of the highest in the world compared only with that of Germany and Japan. It is therefore very important that the British rail network operates smoothly throughout the year. Any delays should be avoided in every possible way. Where this cannot be achieved, delay times should be kept to an absolute minimum in order to avoid significant disruption and complex rescheduling of passenger and freight trains which in our era can result in significant loss of time and unnecessary costs.

It is estimated that road congestion in the European Union costs the equivalent of 2% of the Gross Domestic Product or in excess of 200 billion Euros annually (HM Treasury Infrastructure UK, 2010). Therefore, rail operations have a strategic importance not only for the UK but for the European Union as a whole. However, in order to maintain healthy and reliable rail operations in the UK, Europe and the rest of the world there are three fundamental parameters that need to be fulfilled. Firstly, passenger numbers and freight loads making use of the rail network should be adequate, thus providing enough funds to maintain healthy rail infrastructure and rolling stock as well as support their modernisation over time. Secondly, the rolling stock travelling on the rail network should always meet the operational specifications set for a particular rail line, particularly in terms of maximum axle loads and speeds. Rolling stock should also be sufficiently maintained in order to be reliable and minimise the likelihood of incurring excessive damage on rail tracks due to damaged or worn wheels, e.g. due to profile irregularities such as wheel flats. Finally and most critically, rail infrastructure should be inspected for the presence of defects or missing components and maintained at a level which ensures the safety and reliability of continuous rail operations day after day without compromising the sustainability of existing and future rail projects.

Rail inspection has become a critical factor for the smooth function of rail infrastructure. The results of inspection campaigns seriously influence the maintenance decisions made by rail infrastructure managers and hence it is important that they are evaluated accurately in order to optimise reliability at the lowest possible cost. In the UK this lesson became very apparent after the Hatfield accident in 2000.

## Objectives

Further investments in European, U.S. and Chinese railways are expected to continue until at least 2020 although the current pace is very likely to be maintained until 2030 (European Commission, 2011). Despite the current economic climate, rail transport in terms of passenger number and freight tonnage has been growing at a global scale. In the UK, the British rail network is getting busier and rail freight is exhibiting strong growth whilst passenger numbers are close to the capacity of the network (International Union of Railways (UIC), 2011).

Increasing fuel prices and climate change are likely to contribute further to the growth of British rail transport in the forthcoming years although they are also expected to also pose new important challenges that will need to be overcome in the medium to long term. A number of high-speed lines are currently being planned with the most prominent project in this area currently being the connection between Birmingham and London (Department for Transport (DfT), 2011). Inspection and damage control of rails will be critical in ensuring the smooth operation of the British rail network in the forthcoming years (Papaelias M. , 2011).

This project is concerned with the development of a sound methodology for the application of acoustic emission (AE) techniques for detecting and monitoring crack growth and structural damage evolution in rails. At the moment rails that are found to be damaged on the network are not immediately replaced. Instead an Emergency Speed Restriction (ESR) of 20MPH or 32km/h is imposed and affected rails are replaced within a few days time. The exact timescale in which certain types of the most severe defects need to be replaced depends on their criticality. Thus defects classified as 1A need to be normally replaced within 36 hours whilst those that are classified as 1B require the replacement of the damaged rail section within 7 days. Classification of defect types and criticality are summarised in detail in the British Railway Standard GC/RT5019 (Railway Group Standard, Railtrack PLC, 1998).

By fitting emergency clamps on certain types of defects and imposing a 20MPH ESR then in theory and under normal loading conditions the defect should stop growing until the affected rail section is removed from service. Unfortunately damaged rails with clamps fitted on them cannot be reliably assessed for further crack growth with any other non-destructive evaluation techniques such as ultrasonic testing (UT), Magnetic Flux Leakage (MFL) or Magnetic Particle Inspection (MPI) and this is the reason that a strict speed restriction is imposed by the rail infrastructure manager along the area of the damaged rail section.

There have been occasional reports, although only very few, where clamped defective rails did fracture before the maintenance engineers had been able to complete the renewal of a particular damaged rail section. Such unexpected incidences where final rail failure has actually occurred after the emergency clamps had been fitted have largely been attributed to incorrect evaluation of the actual criticality of the defect detected. Another reason however could be the occurrence of abnormal loading conditions.

Abnormal loading conditions of rails can easily occur on a busy rail network. Higher than expected loads can occur either due to overloading of some freight trains or more commonly due to the development of wheel defects such as wheel flats. Wheel flats and poor wheel-rail conformity due to wheel and rail profile deterioration caused by wear can result in much higher stresses at the wheel/rail interface. Such high stresses may be sufficient to cause further crack growth even if the damaged rail section of concern has been clamped and finally lead to its final sudden failure in a brittle fashion.

If a sound methodology proving that no crack growth takes place after the emergency clamps are fitted on a defective rail section can be developed, then the existing ESR could be potentially raised to 50MPH or even higher speeds minimising delays on the rail network. In addition, the technique could be used to monitor less severe defects and increase our current understanding regarding their evolution with time further.

AE techniques could potentially be applied for the detection as well as continuous monitoring of further crack growth and structural damage evolution in damaged rails therefore removing the need of imposing speed restrictions as low as 20MPH. Furthermore AE sensors could also be fitted in areas that are suspect to contain defects but the inspection results have not been entirely conclusive. In recent years, there has been an increasing interest in AE and its applications for structural health condition monitoring of various industrial assets. Also it has become an increasingly useful research tool in several mechanical testing laboratories around

the world as a means of improving our understanding regarding the mechanisms of damage evolution in all kinds of materials, particularly metal alloys and fibre-reinforced composites.

AE as discussed in more detail further on offers unique advantages over other structural health condition monitoring and non-destructive testing techniques. Although the use of AE has not been widespread within the railway industry, the results of this project indicate that there are significant opportunities for its widespread application within this sector although there are still several technical challenges to be overcome. The fundamentals of AE structural health condition monitoring are discussed at a later point in this thesis.

## Project Structure

This study has been divided into seven chapters, including this introductory chapter, in which the main motivation for carrying out this project has been discussed. The second chapter deals with the metallurgy of rails, the defect types affecting in rails and the inspection methodologies currently in use by the industry for the non-destructive evaluation of new and in-service rails. Within the third chapter of this study the fundamentals of fracture and fatigue are summarised also in relationship to rail steel grades. Chapter 4 discusses the principle of the acoustic emission technique and provides some insight regarding its general applications as well as use within this study. Chapter 5 is concerned with the discussion of the mechanical testing experiments and the analysis of the AE results acquired during three and four-point fatigue tests on rectangular shaped bars manufactured from rail steel. In Chapter 6, the experimental setup used to simulate the in-service field conditions are discussed. The results associated with these trials are also presented and discussed within the same chapter. Finally, in Chapter 7, a summary of the overall findings, together with some recommendations and suggestions for future work are provided.

## 2 Rail metallurgy, defects and inspection techniques

### 2.1 Rail steels

Rail metallurgy and design has evolved significantly over the years. Modern rail steel grades such as the 260 grade are harder than steel grades used in the past resulting in significantly less wear. However, this has also led to new challenges since Rolling Contact Fatigue (RCF) has become more important. Most rails currently being manufactured have a predominantly pearlitic microstructure. Pearlite colonies consist of two phases, soft and ductile  $\alpha$  ferrite, and harder and brittle cementite forming alternating lamellae. Apparently, the presence of cementite is the reason that pearlitic rail steels exhibit a relatively high wear resistance, whilst the presence of ferrite allows an acceptable level of toughness and ductility. The overall mechanical properties are of course also significantly influenced by the interlamellar spacing. Thus as the interlamellar spacing decreases the steel alloy becomes harder and the ductility decreases slightly (Callister, 2006).

Harder rails with bainitic microstructure are also being put under pilot trials. Their use is not as extensive as typical pearlitic-based rails mainly due to unacceptable toughness properties and higher wear rates (Bhadeshia, 2002). Table 1 summarises the typical chemical composition of the steel grades currently used for manufacturing of rails with a predominantly pearlitic microstructure. The carbon content in typical rail steel grades currently in use is normally between 0.55 and 0.78 in wt %. This means that the final microstructure that will form under normal cooling conditions during manufacturing of rails is predominantly pearlitic.

Table 1 Typical chemical composition of pearlite rail steels (Vitez, Krumes, & Vitez, 2004; Mesteel, Unknown)

C	Si	Mn	S	P	Cr	Ni	Mo	V
0.55	0.2	1	0.018	0.013	0.25			0.03
-	-	-	-	-	-	0.25	0.10	-
0.78	1.9	1.5	0.037	0.035	0.50			0.05

Bainitic rail steels have been under investigation, however, their usage has been limited to pilot trials mainly and therefore their application is not so widespread yet. Bainite is a hard phase which forms upon relatively high cooling of steel during production. It consists of a non-lamellar aggregate of carbides and plate-shaped ferrite. Bainite steels may also have some pearlite and ferrite present however the microstructure is always predominantly bainitic. Depending on the alloying elements carbon content in bainite rail steels can vary from 0.04 to 0.52 in wt %. Some bainite steel grades may contain significant amounts of nickel and chromium. According to a study by J. Garnham in 1989, it was concluded that carbide-free bainite will wear faster. On the other hand carbide containing bainite has better wear performance but causes increased wear on the train wheels which are predominantly pearlitic (Bhadeshia, 2002).

## 2.2 Defects in rails

Over the years the manufacturing process of rails has improved dramatically as the steelmaking process has become much cleaner. This has led to a significant reduction in the number of large internal inclusions which could act as natural crack initiation points at very few loading cycles once the rails have been installed in the field. Moreover, surface defects, as can be seen in Figure 1, arising from the production process has also been reduced significantly as they are readily discovered before even the rails leave the factory. Therefore, production defects can be detected at a very early stage minimising future problems after the rails have entered service (Papaelias, Roberts, & Davis, A review on non-destructive evaluation of rails: state-of-the-art and future development, 2008). Production defects found in modern rails include micro structural damage on the surface of the rails, cold marks, rolled in scale, scratches, protrusions, hot marks, cracking and large inclusions. The latter two defect types have an internal origin whilst all other are found on the surface of the rail (Papaelias, Roberts, & Davis, A review on non-destructive evaluation of rails: state-of-the-art and future development, 2008)

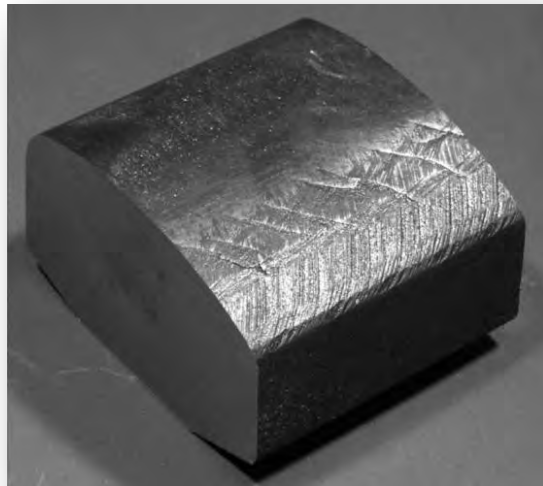


Figure 1 Head checks defect on the rail head surface due to rolling contact fatigue.

In-service, rails can develop several types of defects either due to bending loads, rolling contact fatigue and wear. Defects can be present in the rail head, web or foot of the rail. As seen in Figure 2, typical locations of defects in rail are demonstrated.

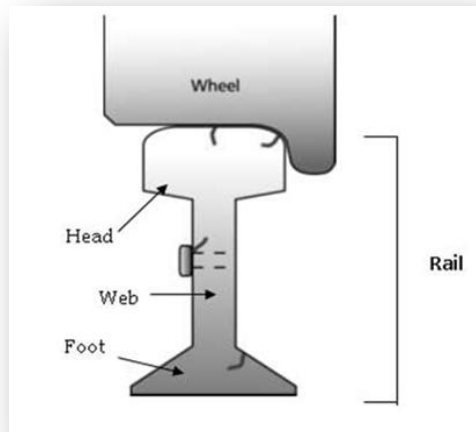


Figure 2 Typical locations of defect in rails(University of Birmingham, 2007; Hocking NDT Ltd, 2012)

In the past most defects found on the network had an internal origin since RCF defects did not have time to develop and were grinded off naturally by passing rolling stock. In modern rail steel grades that exhibit much higher wear resistance, RCF defects have time to initiate and propagate due to the low wear rate. As a result, in modern rails most defects are found on

the rail head either internally or on its surface. Web defects are also more common than rail foot defects. However, rail foot defects are also far more difficult to find due to the awkward for the inspection process shape of rails. RCF defects such as head checks, gauge corner cracking, squats, shelling and corrugation, have become particularly common in modern rail networks (Hocking NDT Ltd, 2012).

RCF was actually the reason behind the Hatfield accident, UK, in 2000, which led to the death of 4 people and the injury of tens more (Reddy, 2007; University of Birmingham, 2007). Before the Hatfield accident took place, inspection engineers examining the rail line in that area had identified a large number of RCF cracks over a long section several tens of metres long (Smith, 2002). Although the maintenance engineers were aware of the problem they decided to proceed with the renewal within two weeks after the inspection had been carried out. Unfortunately, that particular rail section failed after only one week later while an Intercity train was travelling over it at a relatively high speed.

The accident at Hatfield apart from the resulting casualties caused significant disruption and damage on the rail track. The rail line in the area was closed for several months and gave rise to widespread public concern regarding the safety and reliability of rail operations not only within the UK but in Europe overall (Papaelias, Davis, Roberts, Blakeley, & Lugg, 2012). Following, the aftermath of Hatfield accident, the biggest rail renewal in the history of the UK network was initiated with spending exceeding £5 billion. This was due to the fact that several areas of the network had been identified to contain RCF type defects but Railtrack, the UK rail infrastructure manager at the time could not say for sure how many more Hatfield-type accidents were waiting to happen. Moreover, several Railtrack Plc. executives were eventually brought to trial. Finally, the company was partially renationalised and Network Rail was established in its place.

Rail head defects with an internal origin include transverse cracks or tache-ovales, horizontal cracks with or without transverse cracking and longitudinal-vertical cracking. Profile irregularities due to excessive wear of the rail head profile and corrugation are also considered as rail defects and are actually quite important (Hocking NDT Ltd, 2012).

Rail web and foot defects include vertical and longitudinal cracking, star cracking, fish-bolt hole cracking and corrosion (rail foot only). Rail foot corrosion is not an uncommon defect and mainly occurs in tunnels or areas of the networks where water and moisture gets trapped beneath the rail gradually causing the rail foot to corrode. Rail foot corrosion is a particularly

serious defect which is very difficult to detect. Usually, this type of defect remains undetected until it has progressed significantly whilst in some cases it is only found after rail fracture has occurred(University of Birmingham, 2007; Hocking NDT Ltd, 2012).

Defects at the welds may also be present and they have a predominantly internal origin, e.g. micro porosity, shrinkage cavity or inclusions. Rail welds may also break due to excessive contraction of the rails in the winter. Figure 3 shows some typical service defects found in modern rails (Hocking NDT Ltd, 2012; University of Birmingham, 2007).

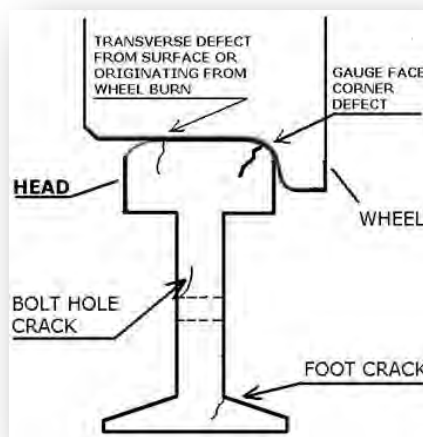


Figure 3 Typical service defects which are originating from the surface in rail (Hocking NDT Ltd, 2012)

Finally, in some cases certain components such as bolts or rail ear-clips may be missing. These are also considered as defects and if they are found missing they need to be replaced as soon as possible with a new one (Papaelias, Roberts, & Davis, A review on non-destructive evaluation of rails: state-of-the-art and future development, 2008).

The defect size tolerance will depend on the specifications of the rail line concerned, i.e. if it is a tram, metro, suburban, intercity, high-speed or freight line. Each rail line type has different allowable maximum loads and speeds. Usually, bigger defects will be tolerable for freight lines in comparison to a high-speed line. Also the requirements for inspection, minimum maintenance action and timescales will vary significantly depending on the rail line type and level of its usage, i.e. tonnage carried per week.

## 2.3 Non-destructive testing (NDT)

As part of quality control new rails are inspected during the production process for the presence of both internal and surface defects using ultrasonic testing (UT), eddy current testing (ECT) and automated vision. This has led into a significant reduction of rail failures due manufacturing defects in recent years. Therefore, most rail failures in modern rails are due to defects that have initiated and propagated due to fatigue from bending and rolling contact stresses while in-service.

Train traffic density, train speeds and axle loads carried on rail network have tremendously increased in the last few decades. Therefore, in-service inspection and maintenance have become a major issue for the safe, efficient and reliable operation of the rail network(Papaelias, Roberts, & Davis, A review on non-destructive evaluation of rails: state-of-the-art and future development, 2008). To extend the lifetime of rails, early crack detection is necessary. Fatigue cracks are not always visible on the rail surface as they can often initiate and grow internally. If cracks reach their critical size sudden failure will take place while a train travels over the damaged rail section. Therefore, various non-destructive testing methods are extensively used to detect and evaluate any defects present on the rail before they lead to failure.

To improve maintenance scheduling, optimise rolling stock operations and minimise unpredicted disruption events due to broken rails, defect rehabilitation should take place before failure has taken place. Initiation of irreversible micro structural damage causes a reduced service lifetime for the railway track (Liu, Stratman, & Mahadevan, 2005). Most defects can be found and evaluated using a variety of manual or automated inspection techniques while the rails are still in-service (University of Birmingham, 2007). These include visual inspection, contact and non-contact ultrasonic testing, liquid penetrate testing, magnetic particle inspection, magnetic flux leakage, eddy current testing, alternating current field measurement and radiography. The manual inspection process is normally carried out either statically or at slow walking-speed pace and involves qualified inspection engineers who deploy manual equipment such as ultrasonic testing walking sticks or push-trolleys on the rail. The photograph in Figure 4 shows an inspection engineer carrying out eddy current inspection using a walking stick in an effort to identify rail head surface and near-surface defects such as RCF cracks.



Figure 4 Trolley mounted crack detection method(Hocking NDT Ltd, 2012)

On the other hand automated inspection can be carried out at speed which can range between 15km/h and 75km/h by deploying the interrogating sensing system either via a hi-rail vehicle or a test train. Hi-rail vehicles do not normally exceed the inspection speed of 15km/h during operation but test trains can reach speeds up to 100km/h if low resolution is acceptable. In the case of automated visual inspection, inspection speeds up to 320km/h are possible (e.g. profile measurements) (Papaelias, Roberts, & Davis, A review on non-destructive evaluation of rails: state-of-the-art and future development, 2008; University of Birmingham, 2007).

Visual inspection can be carried out by experienced personnel that walk along the rail line and notes down any visible defects or missing parts. Automated vision can be carried at speed using cameras and lasers which are normally deployed using a test train. Automated vision systems can be temporarily installed on a normal high-speed passenger train and then removed after the inspection has been completed. Visual inspection does not offer any information regarding internal defects but it does provide substantial information regarding rail head profile wear, gauge distance variations and the presence of corrugation (University of Birmingham, 2007). If excessive rail head profile wear is present then derailments may take place due to poor conformity of the wheel-rail interface. In addition, the presence of corrugation can cause substantial passenger discomfort as well as damage rolling stock.

Magnetic particle inspection and liquid penetrate inspection are both manual techniques which are carried out by expert personnel. Magnetic particle inspection can be used to detect surface and very near-surface defects. Liquid penetrate inspection can be used to detect surface defects only and is commonly applicable on non-magnetic components such as

switches where magnetic particle inspection cannot be used (Hocking NDT Ltd, 2012; University of Birmingham, 2007).

Ultrasonic testing is a fundamental inspection technique and is required for the evaluation of the rails internally. Any internal defects deep in the rail head, web or foot can only be detected ultrasonically. The ultrasonic beam is emitted from a transducer, travels through the rail and back to the sensor after it is reflected by the back wall or any defect present. Ultrasonic testing can be carried out manually with very good results. However, ultrasonic sensors can also be deployed at speed either using hi-rail vehicles or test trains. The quality of the ultrasonic inspection will deteriorate with increasing speed and near-surface and surface defects such as RCF may be very difficult to detect at speed. The use of manual ultrasonic phased arrays has been limited so far. Non-contact techniques using lasers and Electromagnetic Acoustic Transducers (EMATs) are still under investigation (Davis, 2003). One of the EMATs-based inspection systems is demonstrated in Figure 5 (University of Birmingham, 2007).



Figure 5 EMAT inspection system for automated rail inspection mounted on a hi-rail vehicle(University of Birmingham, 2007)

Magnetic flux leakage (MFL) sensors can also be deployed either manually or via hi-rail vehicles and test trains. In most cases magnetic flux leakage testing is carried out at slow speeds using hi-rail vehicles and test trains and is only good for the detection rail head defects, particularly RCF. However, its sensitivity diminishes with increasing speed (University of Birmingham, 2007). In Figure 6, the principle methodology of the MFL is presented.

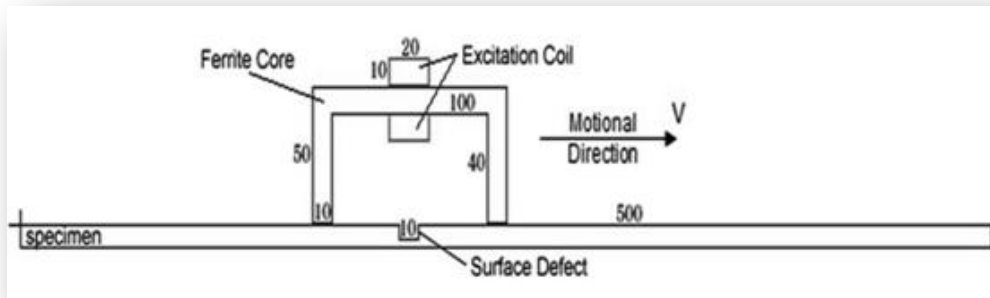


Figure 6 Schematic showing the principle of MFL inspection(University of Birmingham, 2007)

Eddy current testing can be carried out either manually or at speed. Eddy current sensors are more sensitive than magnetic flux leakage sensors but also suffer from high sensitivity to any lift-off variations. Nonetheless, they are very little affected by increasing speed and are very sensitive to near-surface and surface defects, particularly head checks, gauge corner cracking and wheel-burns. Alternating current field measurement has similarities to the eddy current testing but has better lift-off tolerances (University of Birmingham, 2007).

Radiography has only been used occasionally for the verification of welds. This is due to the time required to carry out the inspection, the bulky equipment involved, the health and safety issues and high costs that it involves. Some more extensive pilot trials have been carried out in the past but at the moment radiography remains a restricted inspection tool which is used for the verification of a few tens of welds every year. With the advent of digital radiography and gradual improvement of equipment its usage might become more widespread in the mid-to long-term future. However, this will depend on how ultrasonic phased arrays will fair during weld inspection as their technology also improves over time (University of Birmingham, 2007).

Acoustic emission is a structural health condition monitoring method which has not seen much application in the rail sector so far. The technique can be applied to detect and monitor crack initiation as well as crack growth in structural components. However, it is very important to recognise the useful data from unwanted noise. The source of acoustic emission is related to the application of external loads causing crack growth and subsequently resulting in the emission of elastic waves which can be detected by a piezoelectric sensor (Pollock, 2003).

A damaged rail with a propagating crack during cyclic loading from passing rolling stock traffic will emit acoustic signals which can be detected by the AE sensor. Nonetheless, the AE data will also be contaminated by the rolling noise from the passing train. Unfortunately, the crack will not grow unless rolling stock is travelling over it in order to load it and cause further propagation of the crack. Therefore, it is necessary to investigate to what extent acoustic emission data can be used to reliably detect crack growth in the field which will be contaminated from rolling contact noise generated by the passing trains. The acoustic emission technique is explained in more detail in Chapter 4.

### 3 Fracture and fatigue

#### 3.1 Elastic and plastic deformation

All materials exhibit some degree of elastic and plastic deformation before they fracture. In elastic deformation once the load has been released the material will return in its original shape although in reality some remnant deformation may remain (Ewalds & Wanhill, 1989).

During elastic deformation the stress-strain curve increases predominantly linearly. However, as the deformation increases further and gets closer to the yield strength of the material (also the starting point of plastic deformation) the stress-strain curve becomes non-linear although the overall deformation accumulated is still within the elastic regime. Once the elastic deformation limit or yield strength of the material has been exceeded plastic deformation will occur. The deformation in this case is irreversible once the load has been removed. Some materials may exhibit a considerable amount of plastic deformation prior to final fracture. However, brittle materials will exhibit very limited plastic deformation prior to final failure. The plot in Figure 7 shows the stress-strain curve in the elastic and plastic region and demonstrates the differences between brittle and ductile materials.

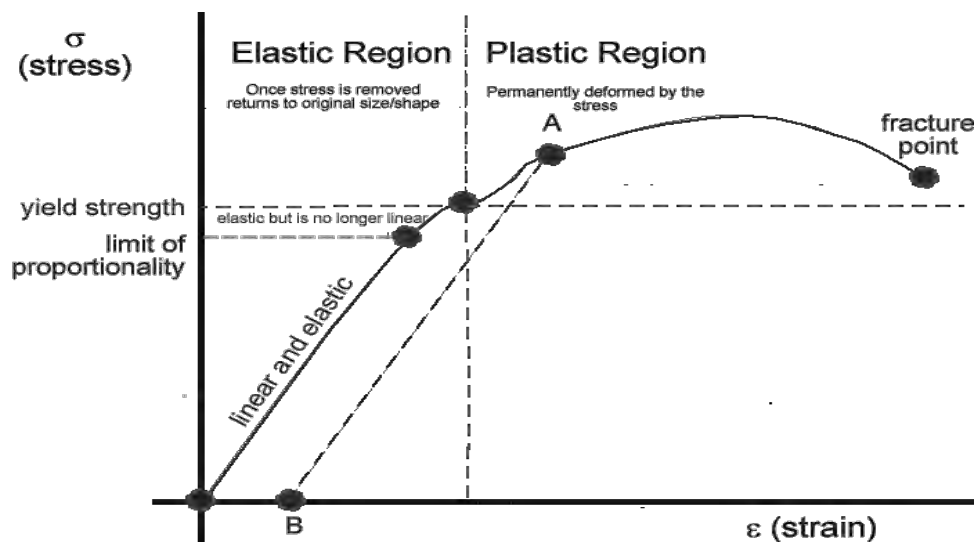


Figure 7 Hooke's Law (Cyberphysics, Unknown)

A reversibly deformed region is also called an elastic deformation region. In elastic deformation the applied force is not sufficient to slide the atoms with respect to each other. Therefore if the load is released, the shape of the specimen reverses to its original shape. In

plastic deformation the applied load is sufficient to cause the atoms bond to break and for crack growth to ensue. Crack growth will only occur after the yield strength of the material has been exceeded. In plastic deformation the linear relationship between stress and strain curve undergoes a change, and the curvature rate of the stress-strain diagram increases.

### 3.2 Bending test

In this project laboratory tests focused on three-point and four-point fatigue bending tests as shown in the photograph and schematic of Figure 8.

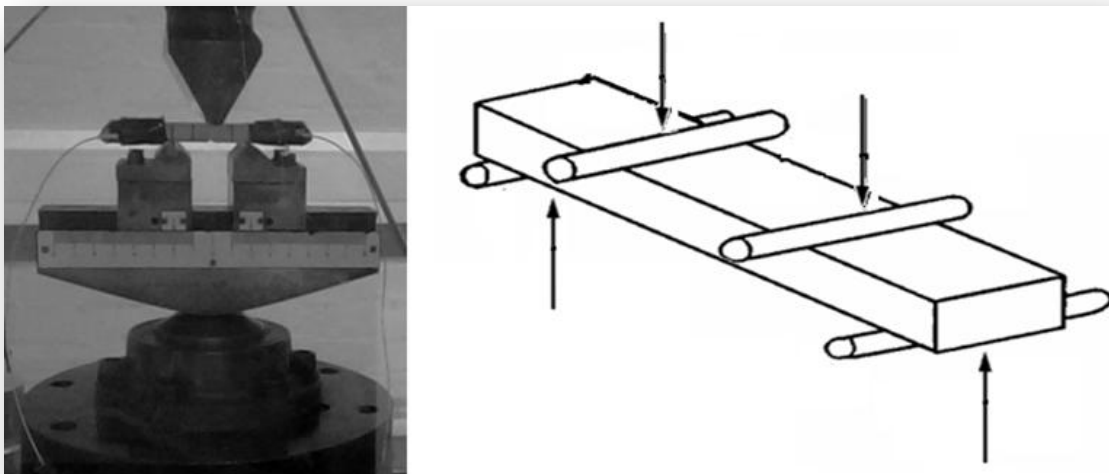


Figure 8 Fatigue Test Specimen (left) and Bending Machine (right) (Texas Tech University, 2012)

Equation 1 is presented below;

Equation 1

$$\sigma_{Max} = \frac{MC}{I} = 1.5P \frac{l}{wt^2}$$

$M$  is maximum moment,  $C$  is the distance from the midpoint of the thickness to the surface, and  $I$  is the area moment of inertia. The area moment of inertia is used to predict the resistance of the cross-section of a beam to bending around an axis that lies in the cross-sectional plane. Thus, the failure stress  $\sigma_{max}$  can be described as a function of the applied force, the beam length over the beam width times the beam thickness squared (Steinzig, 2000; Mechanics and Materials Laboratory, 2008).

Furthermore, the fatigue limit of the specimen is adversely affected once a crack has initiated. A correlation exists between the elastic modulus and the fatigue life of the specimen. If the applied load level exceeds the elastic stress limit (also known as the yield point), deformation will take place (Ewalds & Wanhill, 1989).

### 3.3 Fracture mechanism

#### 3.3.1 Basic fracture modes

Rail steel like all materials can absorb energy up to a certain limit. This limit is known as the toughness of the material. Once the toughness limit of rail steel is exceeded then crack initiation will take place. If the loading levels remain similar then the initiated crack will continue propagating. Crack propagation will gradually accelerate until the crack reaches a critical size and the crack becomes unstable. The energy required to exceed the toughness of rail steel in a typical tensile test is represented by the area below the stress-strain ( $\sigma$ - $\epsilon$ ) curve. Materials with high toughness limit will usually experience a ductile mode of fracture. Ductile fracture involves an appreciable amount of plastic deformation before final failure occurs. On the other hand brittle materials exhibit a lower toughness limit and final failure takes place with no or very little plastic deformation being involved.

Unless a rail already contains a critical defect from the manufacturing process then any crack initiation will take place after an appreciable number of loading cycles as long as the loads sustained remain within the design parameters. Rail steel grades exhibit reasonable ductility and therefore after crack initiation subsequent crack growth will evolve further with every loading cycle. Once a critical crack size has been reached the affected area will fail abruptly in a brittle fracture mode.

Figure 9 shows the  $\sigma$ - $\epsilon$  curve for typical brittle and ductile fracture modes. A ductile material shows significantly more tolerance to plastic deformation than a brittle material before it finally fails (DoITPoMS, 2008).

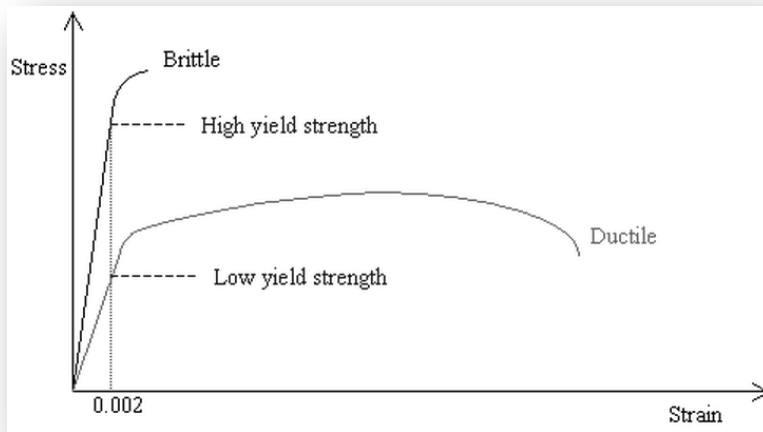


Figure 9  $\sigma$ - $\epsilon$  curve for brittle and ductile fracture mode (DoITPoMS, 2008)

Evolving cracks can propagate either through the grains of the material, i.e. in a transgranular mode of fracture or along the grain boundaries, i.e. in an intergranular mode. In rail steel as with most polycrystalline materials cracks will grow in a transgranular mode moving through the pearlite colonies (Ewalds & Wanhill, 1989).

In trans-granular crack growth the breaking of the atomic bonds takes place along the crystallographic planes due to the applied load. On the other hand during intergranular fracture the bonds between the grain boundaries are broken when the load is applied on the material. (Callister, 2006). The schematics in Figure 10 demonstrate the transgranular and intergranular fracture modes.

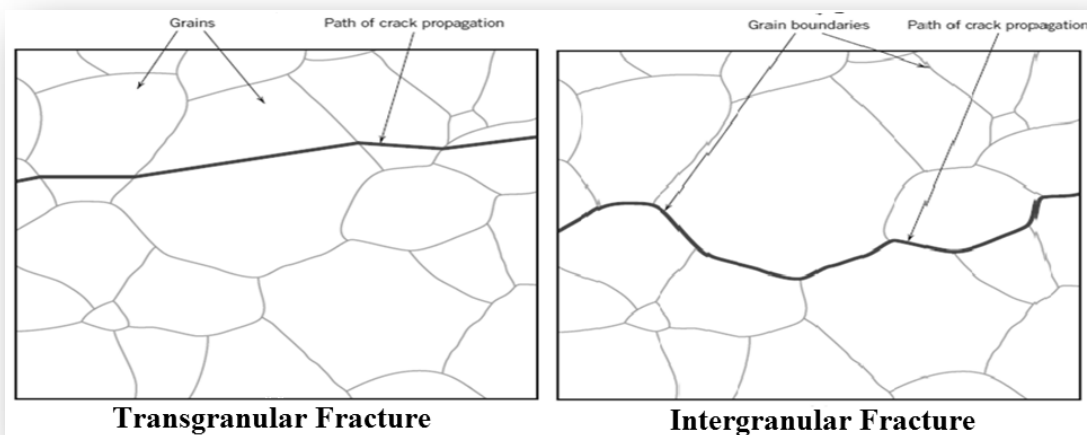


Figure 10 Crack propagation mechanisms (Callister, 2006)

Intergranular fracture involves crack propagation between the grain boundaries of which the separation or breaking does not need as much energy as transgranular fracture. The reason is that the alignment between the grain boundaries is majorly uniform; however the alignment inside of the grains is totally different from each other (Callister, 2006; Ewalds & Wanhill, 1989). The interior of the grains is formed by irregular orientation of the crystal lattice. Although, cracks can easily proceed between the grains, crack propagation needs a high energy to break through the grains. The fractographic image of the scanning electron microscope (SEM) in Figure 11 shows the appearance of ductile intergranular and transgranular fracture modes.

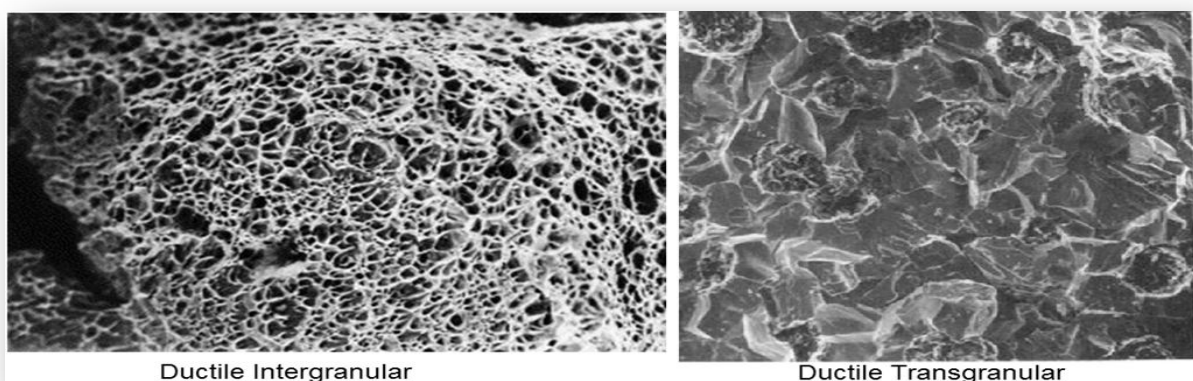


Figure 11 Scanning electron fractographs of ductile inter-granular and trans-granular fracture modes (Anderson, 1995)

If the material is meant to have a long service life, then it needs to experience some ductility in order to avoid sudden brittle fracture. Rail steels are thus required to have apart from good wear resistance, a reasonably good yield strength and toughness.

The crystallographic alignment is deformed when the applied stress levels exceed the yield strength. For ductile materials, final failure takes time due to rubber-like properties. Ductile fracture involves a relatively slow crack propagation process thanks to the plastic deformation tolerance of ductile materials. During the design of industrial load-bearing components, a ductile fracture mechanism is always desired as it involves a low crack propagation velocity rate under loading conditions that do not exceed the design limits. Therefore, there is an opportunity of detecting and evaluating any evolving cracks that may be present in a component before final failure occurs and appropriate maintenance can take place in time to address the problem. In the case of brittle fracture crack growth rates are very high and hence failure takes place extremely rapidly once a crack has initiated without any

appreciable amount of time allowed to detect the problem and schedule appropriate maintenance (Anderson, 1995).

Prior to the crack initiation, ductile materials absorb a high level of energy through the extended plastic region. Plastic deformation during ductile fracture mode is demonstrated in Figure 12. It can be seen that under the applied tensile load once the yield strength of the material has been exceeded the cross-section shape of the specimen changes as plastic deformation progresses further until final failure. The level of plastic deformation experienced by a material will depend on the ductility level it exhibits. Micro structural defects (such as impurities or second phase particles) can provoke the initiation of microvoids inside the material. Then these voids will then grow and merge with each other as the material plastically deforms further leading eventually to cracking. The physical shape will also change under the tensile load (Callister, 2006).

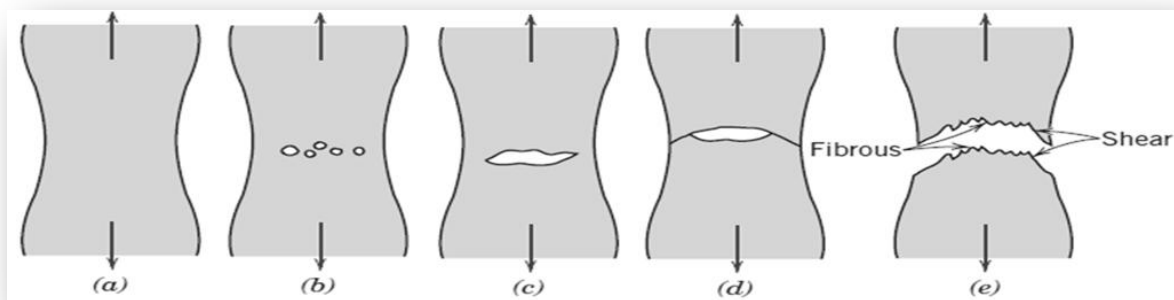


Figure 12 Ductile fracture stages: a) Initial necking. (b) Small cavity formation. (c) Coalescence of cavities to form a crack. (d) Crack propagation. (e) Final shear fracture at an angle relative to the tensile direction.(Callister, 2006)

In brittle fracture the ductility of the material is low, and any crack initiating will become almost immediately unstable causing final failure without warning. The plastic deformation limit of brittle materials is very low and therefore crack growth takes place extremely rapidly through successive breaks of the atomic bonds along specific crystallographic planes. This fracture process is also known as cleavage (Callister, 2006). In a similar fashion with ductile fracture, crack growth can be either trans-granular or inter-granular. The SEM fractographic image in Figure 13 shows the difference in the topography of brittle trans-granular and inter-granular fractured surfaces,

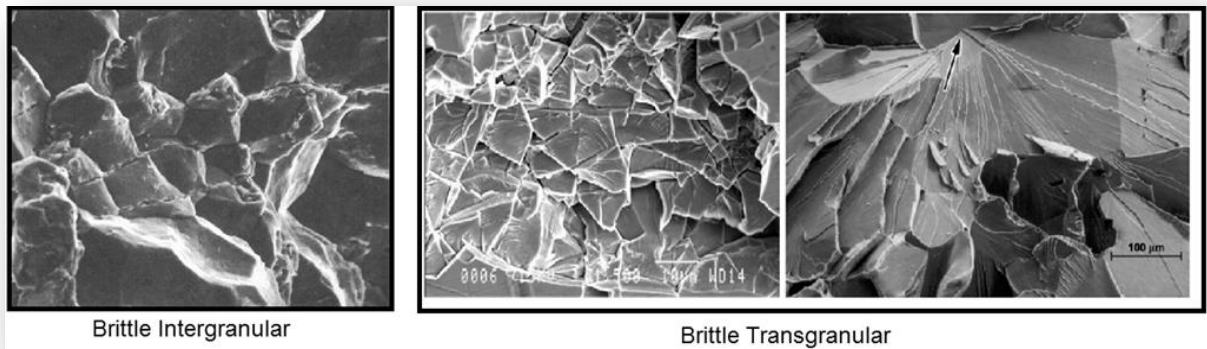


Figure 13 Microstructure of Brittle Fracture Mechanism(Anderson, 1995)

In contrast to ductile materials, the fractured region of brittle materials is shown to have a smoother topography (Anderson, 1995). The photographs in Figure 14 show the appearance of the macroscopic fractured region for ductile and brittle materials.

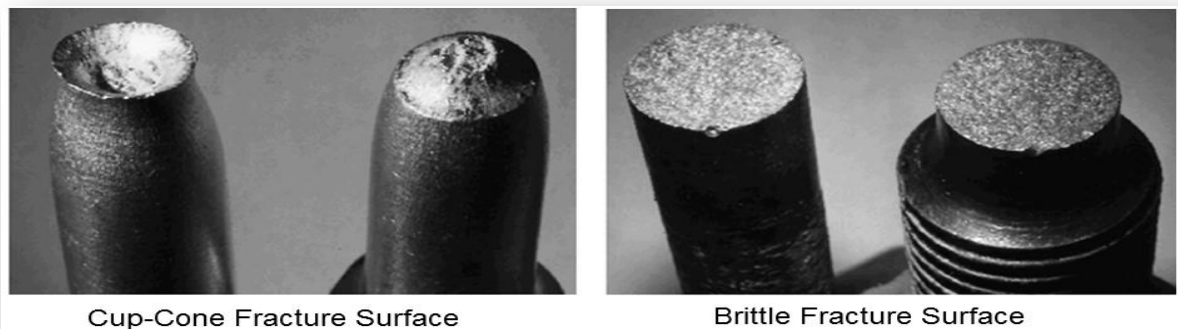


Figure 14 Cup-and-cone (ductile) fracture and Brittle fracture(Anderson, 1995)

To evaluate the relationship of crack length and externally applied load, the Griffith theory of brittle fracture has been developed (Ewalds & Wanhill, 1989). Propagating cracks will release some of the energy stored in the material as it is elastically deformed. This energy is called elastic strain energy (Callister, 2006). The critical stress,  $\sigma_c$ , required for crack propagation in a brittle material can be calculated using this relationship which is dependent on the elasticity modulus, E of the material as can be seen in Equation 2.

Equation 2

$$\sigma_c = \left( \frac{2E\gamma_s}{\pi\alpha} \right)^{1/2}$$

where  $\gamma_s$  is the specific surface energy and  $\alpha$  is the one half the length of an internal crack(Callister, 2006).

To generate the fatigue crack on the specimen, an external cyclic load is used as the driving force. The crack initiation occurs when the surface energy exceeds a critical value at which point the atomic bonds have just been broken. Surface energy can be calculated using Equation 3 (Ewalds & Wanhill, 1989).

Equation 3

$$S = 2\gamma a$$

During the mechanical analysis of the stress field, the strain energy and surface energy of the specimen are crucial to explain the crack evolution. The Griffith theory of brittle fracture provides information about how energy balance affects the crack propagation. Figure 15, the Griffith Theory is ideally explained for brittle materials, and has also been shown that having a critical crack length depends on the surface and strain energy release rate.

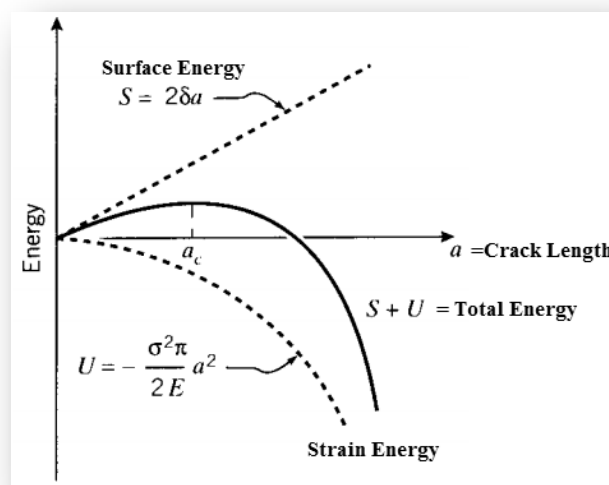


Figure 15 Energy changes associated with incremental crack extension(Roylance, 2001)

Depending on the micro structural properties, the crack propagation may divergently be affected by the value of the released strain energy. This relationship is explained by Equation 4, and  $A$  is the area of the crack surface and the strain energy release rate,  $G$ , is determined with the equation  $(G = dU/dA \approx dU/td\alpha)$ ,

Equation 4

$$\frac{dU}{d\alpha} = \frac{dS}{d\alpha}$$

where  $\alpha$  is the crack length and  $t$  is the thickness of the specimen. The relationship between the absorbed total strain energy ( $U$ ) and surface energy ( $S$ ) with crack length,  $\alpha$ .

Until a critical crack length,  $a_c$ , has been reached, crack extension will occur when the strain energy release rate has reached a critical value,  $G_c$ . During the crack propagation, the fatigue life of the specimen becomes independent of  $G$  (James, 2001). As seen in Figure 16, the total energy increases at a stable rate, due to the fact that the crack length has already exceeded the critical crack length and the fracture toughness has been exceeded. After having a longer crack than the critical crack length, the strain energy release rate cannot be explained with the Griffith theory of brittle fracture. The crack present grows until fatigue failure occurs.

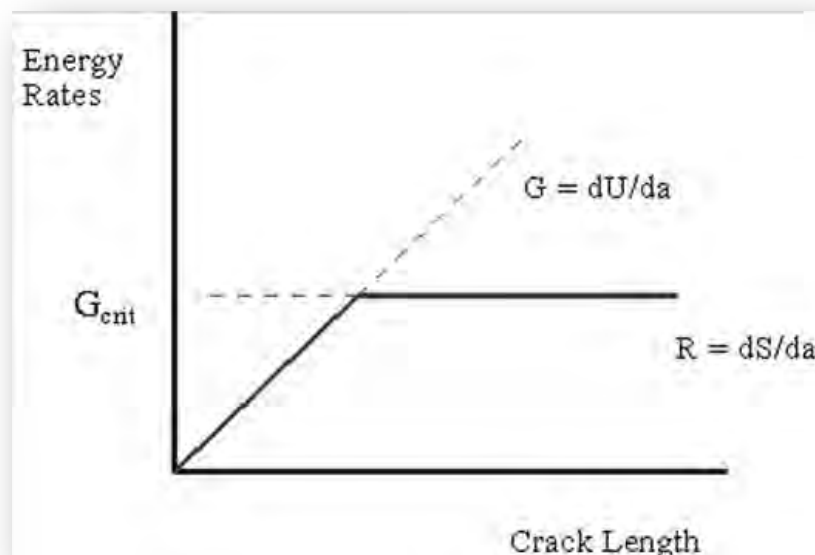


Figure 16 The relationship between energy rates and crack length (James, 2001)

In the case of a perfectly brittle material, if the total energy is equal to zero, a crack can catastrophically propagate. This condition is different for ductile material, because, ductile material should exceed the plastic deformation energy rate (Callister, 2006). The elastic energy release rate for ductile material is equal to the cumulative result of the surface energy and plastic deformation energy.

The schematic in Figure 17 shows the three different modes of crack growth. The type of the applied load influences crack propagation. Mode 1, also known as the opening mode is based on tensile loading and causes the opening of the crack during its propagation. The crack surface, due to the tension load, separates the two parallel planes of the sample. Mode 2 is related to the gradual sliding of the two parallel planes in the area of the crack caused by shear stresses. Finally Mode 3 is related to tearing also caused by shear stresses (Hertzberg, 1976).

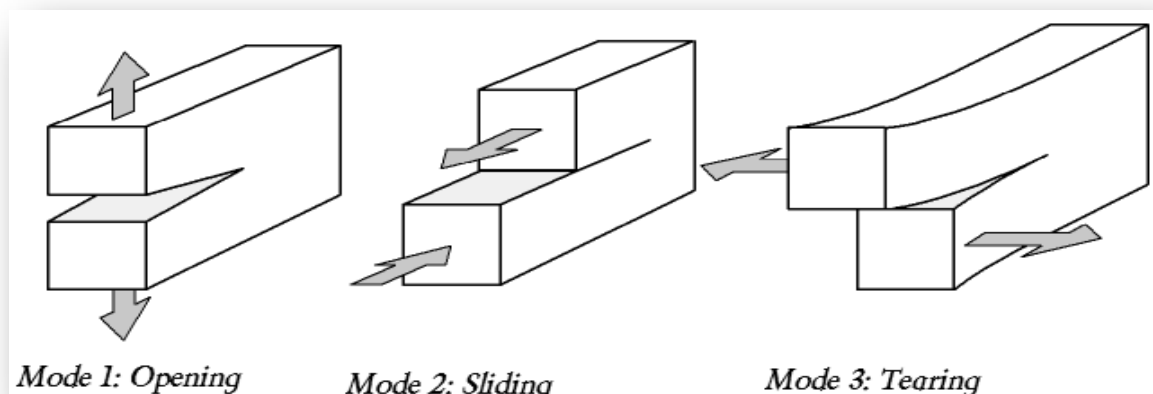


Figure 17 The modes of crack surface displacement (Ewalds & Wanhill, 1989)

### 3.3.2 Fatigue fracture

Fatigue fracture takes place due to repeated load if the cyclic loading sustained by the material exceeds its fatigue limit. The fatigue limit itself will vary from material to material but it typically will lie between 35% and 60% of the tensile strength although some materials may not have a fatigue limit at all (e.g. aluminium) (Callister, 2006). Figure 18 shows typical fatigue limit curves for mild steel and an aluminium alloy (Ewalds & Wanhill, 1989).

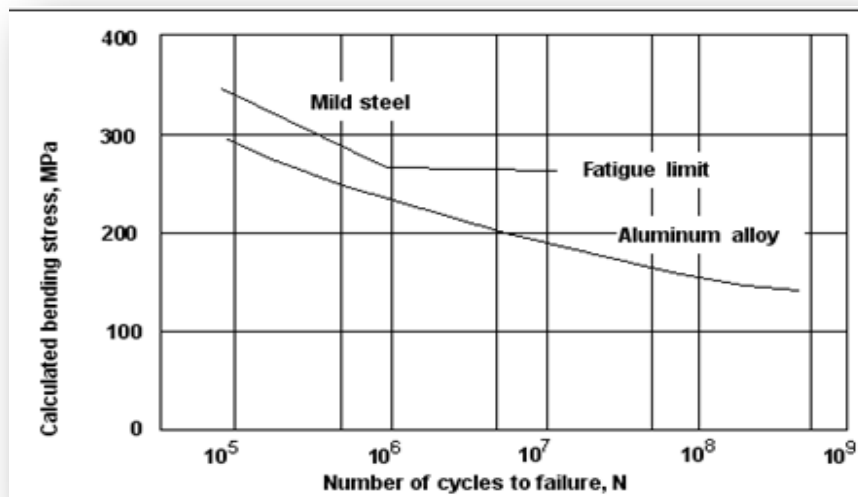


Figure 18 Typical S-N Curves for Ferrous and Nonferrous Metals(Ewalds & Wanhill, 1989)

If the cyclic stresses do not exceed the fatigue limit of the material then fatigue failure will not take place even at an infinite number of loading cycles. However, if the stresses do exceed the fatigue limit then failure will occur at a number of cycles which can be predicted theoretically. The number of cycles that the material will be able to survive before it finally fails will depend on the extent by which the actual stress levels sustained during every loading cycle exceed the fatigue limit of the material. During fatigue final failure will occur due to both ductile and brittle crack propagation. Table 2 shows the typical fracture surface characteristics for each mode of fracture (The University of Southern Mississippi, 2001).

Table 2 Fracture mechanisms and their surface characteristics(The University of Southern Mississippi, 2001)

Mode of Fracture	Typical fracture surface and characteristics
<b>Ductile</b>	Cup and Cone, Dimples, Dull Surface, Inclusion at the bottom of the dimple
<b>Brittle Intergranular</b>	Shiny, Grain Boundary cracking
<b>Brittle Transgranular</b>	Shiny, Cleavage fractures, Flat
<b>Fatigue</b>	Crack initiation, propagation and zone of final fracture

Once a fatigue crack has initiated then it will gradually propagate with every cycle, in the beginning very slowly and then faster until a critical size has been reached after which sudden brittle failure will occur. The tolerance of the component to crack growth will depend both on the amplitude of the applied cyclic stress level as well as the stress ratio. Thus, the number of cycles that a component can sustain will primarily depend on these two factors as long as no unknown crack is already present. The allowable maximum stress will depend on the crack length. Above a certain crack length final failure will occur as shown in Figure 19 (Labossiere, Flores, & Vant, 2007).

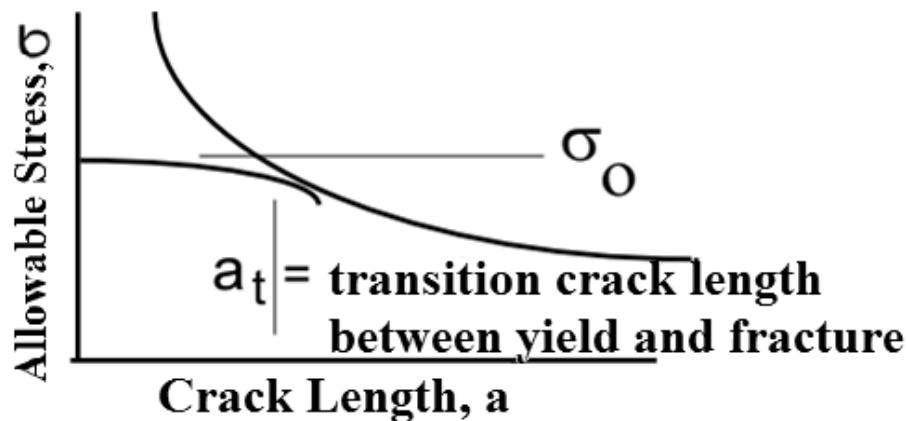


Figure 19 The external load versus crack length (Labossiere, Flores, & Vant, 2007)

The induced crack propagation is arising from the applied cyclic stresses. When the applied stress increases on the specimen, the crack dramatically propagates. To examine the dynamics of the crack propagation, the component under investigation should be subjected to repeated loading cycles (loading and unloading) (International Atomic Energy Agency, 2000). The fracture mechanism will depend on the micro structural characteristics and overall mechanical properties of the material. However, not only micro structural characteristics and mechanical properties but also test environmental conditions (e.g. the presence of salt water or other oxidising atmosphere) can affect the service life of the specimen causing much higher crack growth rates due to stress corrosion cracking (SCC). Thus, the same specimen can fail unexpectedly in much less loading cycles and even lower load levels due to environmental effects (Diener, 2009).

Figure 20 shows the relationship between the number of cycles and the crack propagation rate. As the crack grows the crack growth rate will accelerate under consistent repeating loading cycles. Griffith's theory, discussed in the following section explains the crack growth mechanism.

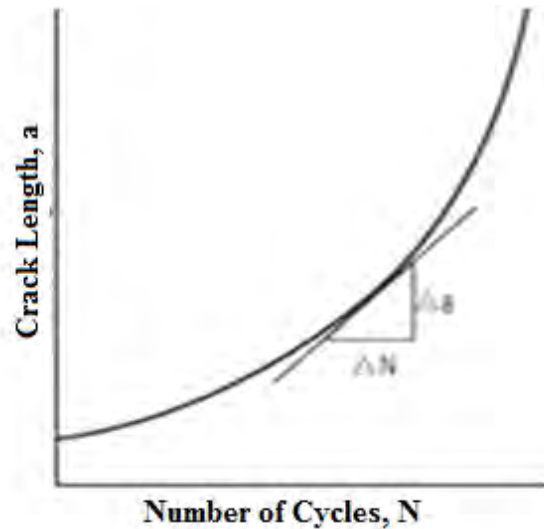


Figure 20 The relationship between the crack length and number of cycles (James, 2001)

Assembled data from various scientific research studies indicates that if the specimen has got any inherent discontinuities or different geometric alignment system, these issues may pose a risk in the future, resulting in unexpected failure and lower fatigue limit. For example, if any notch is present on the specimen, after numerous cyclic loading, stress accumulates around the notch. The crack will initiate on the top of the notch region and will propagate from there until fatigue failure occurs (James, 2001; Roylance, 2001).

The stress intensity factor,  $K$ , and the fracture toughness of the material,  $K_{IC}$ , play a key role in determining the maximum load level that can be sustained by the material above the yield strength and therefore both parameters are taken seriously into account during the design process of any load bearing component. The stress intensity factor is a function of the applied stress, geometrical factor, crack size and load level. Equation 5 indicates the relationship of the stress intensity factor with applied stress, crack length and sample geometry (Ewalds & Wanhill, 1989).

Equation 5

$$K = \sigma \sqrt{(\pi a)} f(a/w)$$

The stress intensity factor is also used to measure the material's fracture toughness,  $K_{IC}$ .  $K_{IC}$  dictates the stress intensity factor level beyond which a crack will become unstable and abrupt brittle fracture will occur. When the crack length exceed the limit, the stress intensity factor,  $K$ , becomes dominant instead of the strain energy release rate,  $G$  (Ewalds & Wanhill,

1989). Since, the crack propagation does not depend on the energy release rate above the yield strength. Equation 5 can be used to calculate the maximum fatigue stress level (Ewalds & Wanhill, 1989). The mathematical equation of the fracture toughness is given in Equation 6, and the unit is  $\text{MPa}\sqrt{\text{m}}$ . Shear stress occurs during the mode 2, thus  $K_{IIc}$  is calculated with the shear stress level,  $\tau$ ,

Equation 6

$$K_{Ic} = \sigma Y \sqrt{a} \quad (\text{for mode 1})$$

$$K_{IIc} = \tau Y \sqrt{a} \quad (\text{for mode 2})$$

The stress intensity factor relies on the linear elastic theory, and the maximum fatigue stress level is called as  $\sigma_f$ . The mathematical explanation of the stress intensity factor can be calculated using Equation 7 for all types of fracture mechanism. Then, the maximum fatigue stress is written as seen in Equation 8.

Equation 7

$$\sigma_{ij} = \frac{K}{\sqrt{2\pi a}} f_{ij}(\theta)$$

Equation 8

$$\sigma_f = \frac{K_{II}}{\sqrt{2\pi r}}$$

In Equation 9, the range of the stress intensity factor,  $\Delta K$ , is depending on the crack size,  $a$ , and the number of load cycles,  $N$ .  $C$  and  $m$  are material constants (Ewalds & Wanhill, 1989).

Equation 9

$$\frac{da}{dN} = C \Delta K^m$$

$\Delta K$  determines the differences between maximum and minimum values of the loading cycles, which is indicated in Equation 10 (Ewalds & Wanhill, 1989).

Equation 10

$$\Delta K = K_{\max} - K_{\min}$$

### 3.4 Effect of stress ratio (R)

The endurance life of a component heavily depends on the ratio of the maximum and minimum stresses sustained. During the reload time, if a vast gap between the maximum and minimum stress level exists, the specimen can easily deform under a few number of cycles. To explain the relationship between the stress level and R-ratio, Equation 11 is given below;

Equation 11

$$R = \frac{K_{min}}{K_{max}} = \frac{\sigma_{min}}{\sigma_{max}}$$

To prevent the catastrophic failure due to the rapid crack propagation, maximum and minimum stress level should be close to each other. Furthermore, the stress intensity factor can also be explained with the R-ratio. Pereira et al. (2008), carried out a number of investigations to indicate the effect of the different R value on the S-N curve. Although the S-N curve is going to be explained later on in this thesis, the results are basically explained in Figure 21. The triangle shape in the plot of Figure 21 represents the highest level of R-ratio (0.3) employed, and it shows that the specimen did not deform until 400MPa. Moreover, the number of cycles to failure is quite higher than the other experiments which were carried out at a lower stress ratio condition.

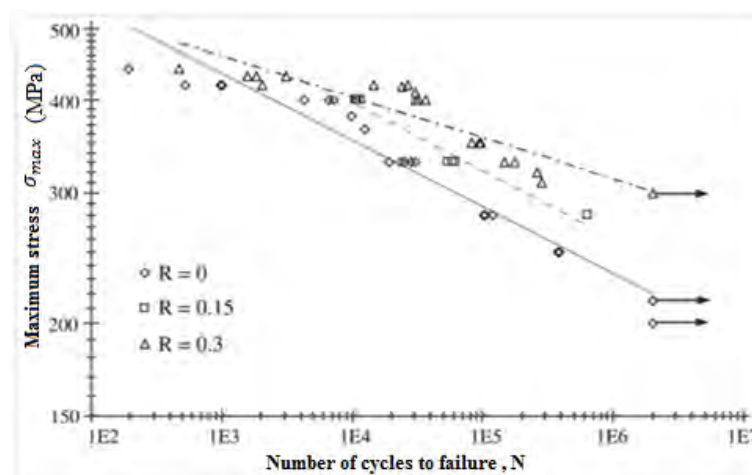


Figure 21 The relationship between the maximum stress and the number of cycles to failure depending on the R-ratio(Pereira, Jesus, Ribeiro, & Fernandes, 2008)

Consequently, the longer service life can be attained via the small gap between the maximum and minimum applied load, which is known as a high level R ratio.

### 3.5 The effect of the fatigue crack propagation curve

The Paris-Erdogan's rule shows the relationship between the stress intensity factor range,  $\Delta K$ , and the crack growth rate,  $da/dN$ . The fatigue crack growth curve is shown in Figure 22 (Ewalds & Wanhill, 1989). clearly shows the direct relationship between  $\Delta K$  and  $da/dN$  and visualises the Paris-Erdogan Law. Below a certain  $\Delta K$  value any pre-existing crack will not propagate further. This known as the threshold for fatigue crack growth and is denoted as  $\Delta K_{TH}$ . The rate of crack growth within the threshold region (Region I) is very slow. In Region II the relationship between  $\Delta K$  and  $da/dN$  is linear and is very well described by Paris-Erdogan's law. Within region III the critical crack length has been reached and crack becomes unstable resulting in the brittle fracture of the material (Beden, Abdullah, & Ariffin, 2009; Ewalds & Wanhill, 1989).

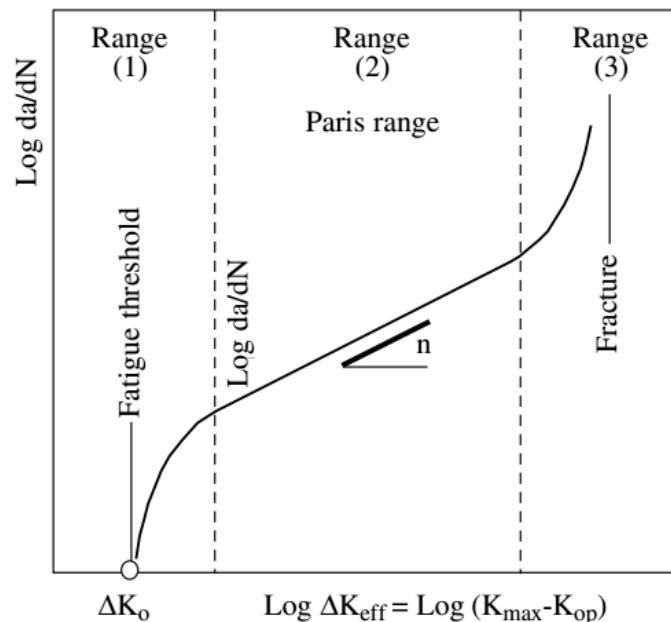


Figure 22 Scheme of the typical fatigue crack propagation curve (Ewalds & Wanhill, 1989)

#### 3.5.1 Region 1 - Threshold

First phase is called as threshold region which represents the low crack growth rates. In theory, the driving force to propagate the crack length is provided above the critical stress intensity factor. However, threshold stress intensity factor is less than the critical stress intensity factor, thus the crack do not propagate (Chaswal, Sasikala, Ray, Mannan, & Raj, 2004). After high cyclic fatigue load exposure of the specimen, fatigue crack initiation is seen.

On the other hand, the number of stress cycles and some external factors (such as grain size, mean stress of the applied load, and environmental effect) may sometimes affect the crack growth ratio. For instance, a corrosive atmosphere leads to a shorter service life of the specimen, having major grain size can cause rapid crack propagation. According to the American Society for Testing and Materials (ASTM) regulation E647, the fatigue crack propagation rate in region I can measure between  $10^{-8}$  to  $10^{-6}$  mm/cycle.

### 3.5.2 Region 2 - Paris Regime

The rate of the crack propagation dramatically increases in the second phase and can be calculated using the Paris-Erdogan law. During this phase the crack growth rate is linearly increasing with  $\Delta K$ . The crack propagates under cyclic loading due to the elastic-plastic fracture mechanism.

Opening, sliding and tearing fracture mode (as seen in Figure 23) can exist in the linear elastic fracture mechanism due to the loading mode at certain stress and certain crack length value. On the contrary to the first stage, the limit of the endurance is less than the specimen of which the toughness value is close to the threshold limit. Due to the existing crack, the specimen is not durable at high load applications. According to the “E647” regulations established by ASTM, they claim that the fatigue crack propagation rate can measure after  $10^{-6}$  to  $10^{-3}$  mm/cycle.

### 3.5.3 Region 3 - Fracture

Crack growth rate in region III is much higher than that in region II and failure is almost immediate once this phase has been reached due to unstable crack growth. The stress intensity factor is much higher than the critical limit of the stress intensity factor. Therefore, overloading conditions cause rapid crack evolution. According to the E647 regulations established by ASTM, fatigue crack propagation rate can measure above  $10^{-3}$  mm/cycle (Beden, Abdullah, & Ariffin, 2009). The service life of the specimen is not sufficiently long enough to analyse the specimen due to the rapid crack propagation conditions. In a large plastic zone near the crack region, fracture toughness ( $K_C$ ) is activated in stage three. Figure 23 shows the effect of fracture toughness on the governing failure mechanism (Anderson, 1995).

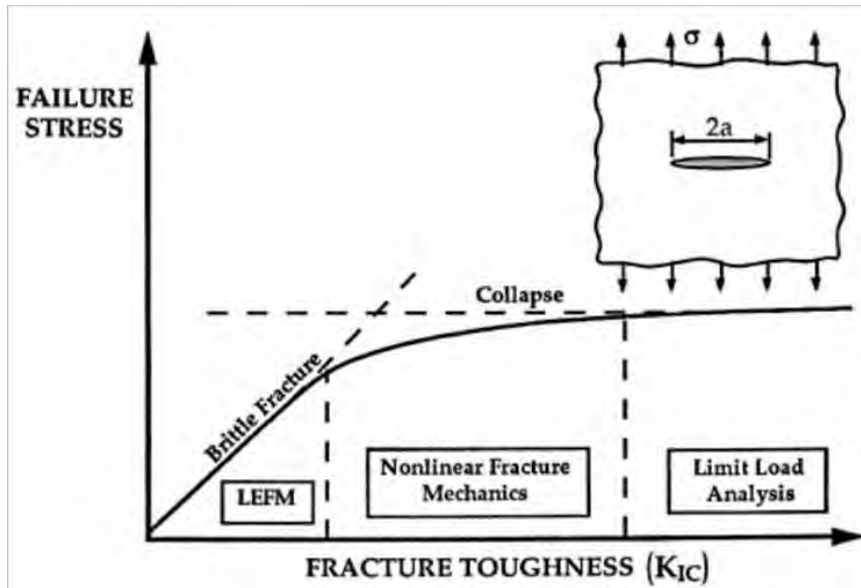


Figure 23 Effect of fracture toughness on the governing failure mechanism. (Anderson, 1995)

### 3.6 Energy balance approach

Industrial applications are commonly subject to dynamic loads instead of static loads. Therefore the yield strength plays a crucial role in the design of load bearing structural components. If the external load applied exceeds the yield strength, the material will deform due to plastic deformation. A substantial number of research studies have focused on the critical assessment of the fatigue crack growth during the dynamic loading tests. As crack length increases the remaining in-service lifetime of the component is reduced substantially and the risk of catastrophic failure increases.

Sometimes discontinuities depending on their distribution and characteristics may cause an increase in the endurance limit. For instance, if the microstructure is reinforced with a second phase particle, the movement function of the particles may not allow the crack propagation. Either dislocations or second phase particles are used to raise the fatigue strength of the structural component. In order to increase the durability of the component against fatigue any microstructure-related problems should be overcome during the design stage of the component. (International Atomic Energy Agency, 2000).

## 4 Acoustic Emission (AE) Technique

### 4.1 AE method

The acoustic emission technique for structural health condition monitoring relies on the detection and evaluation of transient elastic waves produced by sudden redistribution of stress in a material or component when it is loaded beyond a certain limit. Nonetheless, several acoustic emission sources may be of external origin, e.g. impact on the surface of the component or background noise generated from an external source, e.g. a machine. Internal sources of acoustic emission related to the application of an external load are dislocation movement, void formation and expansion, crack initiation, crack growth and corrosion. The principle of acoustic emission technique can be visualised in Figure 24 (NDT Education Resource Center, 2001-2012).

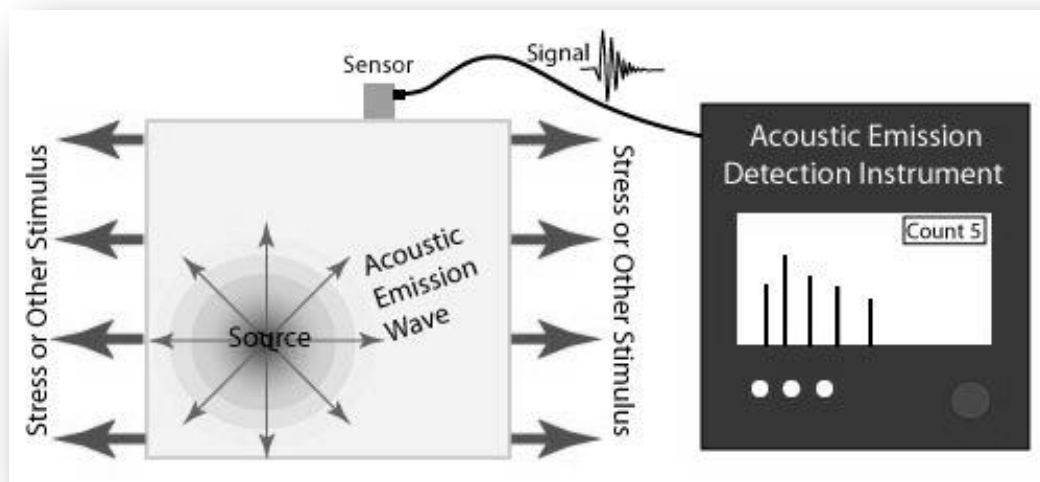


Figure 24 Principle of AE technique (NDT Education Resource Center, 2001-2012)

Acoustic emission can provide extremely useful information regarding the condition of a structural component. It is very successful in detecting crack initiation and crack propagation in a material or component. However, quantification of the actual damage sustained by the component based on acoustic emission data alone can be very tricky. Usually, AE activity will be very high if the defect has reached a critical size but this may not always hold true if testing parameters are not set correctly. Moreover, every effort should be made to remove the effect of unwanted background noise from the measurement.

A typical example of the acoustic emission signal or hit arising from crack growth is shown in Figure 25 below (Huang, Jiang, Liaw, Brooks, Seeley, & Klarstrom, 1998). The main features are the threshold of the signal, amplitude, rise time, duration of the hit, counts to peak and total number of counts.

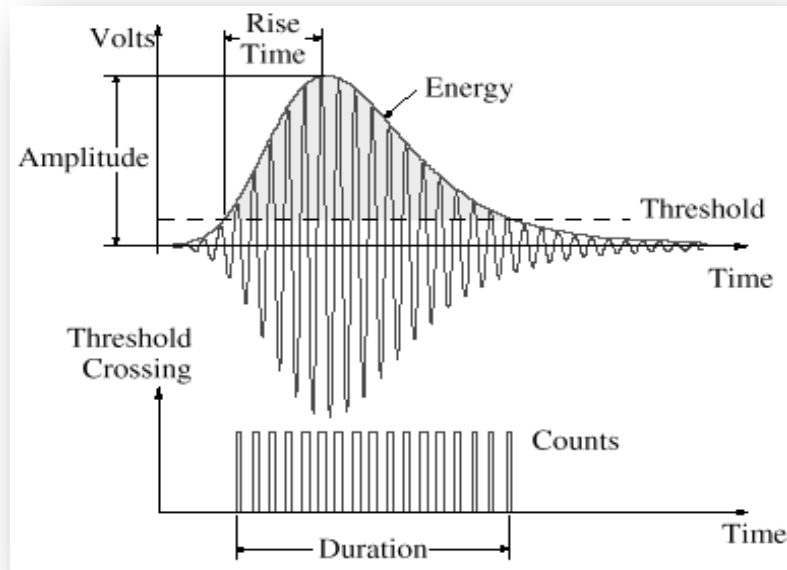


Figure 25 Main features of an AE hit (Huang, Jiang, Liaw, Brooks, Seeley, & Klarstrom, 1998)

The threshold is the lower limit of the AE activity which when exceeded a hit will be recorded by the system. Usually the threshold settings will depend on the background noise levels. The amplitude of the hit is basically the peak of the signal. The count to peak is the number of times that the AE signal exceeds the threshold before it reaches its peak. The total number of counts is the times that the signal exceeds the threshold throughout the hit. Duration is the time from the first threshold crossing to the end of the last threshold crossing. Rise time is the time from the first threshold crossing to the maximum amplitude. The energy of the signal is the integral of the rectified voltage signal over the duration of the AE hit. Finally, the average frequency of the signal is the number of acoustic emission counts over the duration of the hit. The relationship is shown in Equation 12.

Equation 12

$$V_{average} = AE \text{ counts} / \text{Hit duration}$$

A typical acoustic emission system will consist of a piezoelectric sensor mounted on the surface of the material or component under investigation, a pre-amplifier, an amplifier, a data acquisition board and a PC where data are logged and processed using appropriate software. Figure 26 shows the typical architecture of AE systems(Husin, Mba, & Hamzah, 2010).

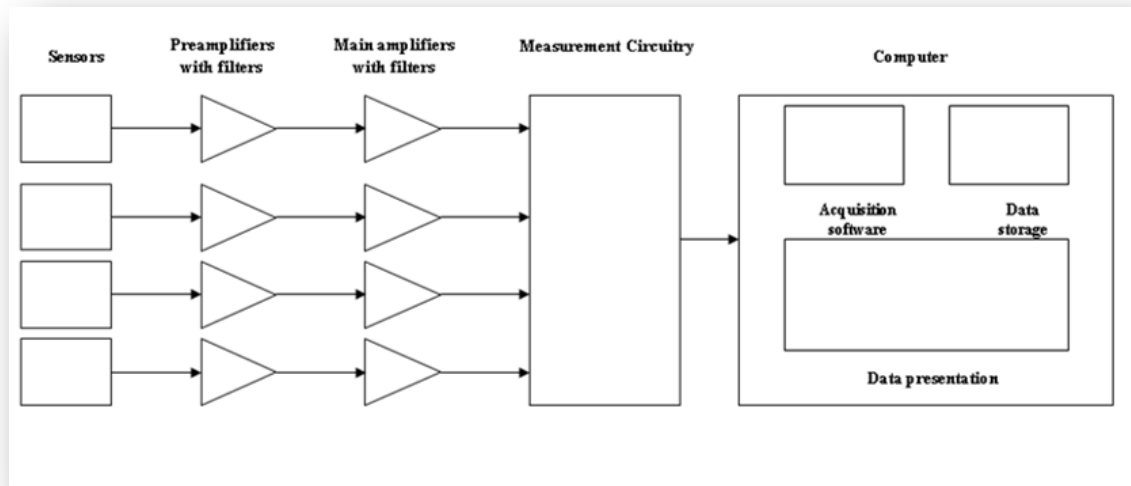


Figure 26 AE system architecture(Husin, Mba, & Hamzah, 2010)

## 4.2 Deformation process and AE method

Crack growth can take place under stable or unstable propagation. The strain rate of the specimen affect the kinetical motion of the dislocation under the fatigue load, and the obtained AE signals are examined to investigate this kinematical movement. When the crack iniation has taken place, the absorbed energy will be released due breaking of the grains or grain boundary sliding. When the strain rate increases, the energy emitted will increase too thus giving rise to higher levels of AE activity. High amplitude AE signals will normally arise in the plastic region (Han, Luo, & Wang, 2011) .

Deformation and crack growth can be detected using the AE method. According to Hooke's Law, the yield point is the separator between elastically deformed and plastically deformed region. To detect the crack propagation with AE sensors, a static or cyclic load of sufficient magnitude needs to be applied by an external means. Throughout the test, miniscule crack growth events will cause the emission of elastic stress waves which can be detected by the AE sensors. Micro structural discontinuities are the only AE sources from which high

amplitude acoustic signals can be generated. For instance, during the atomic bonding breaking, high energy AE events are recorded and AE signals can significantly exceed the threshold limit.

Compression testing is an easy way to show the impact of the deformation changes on the AE recorded data. Puri & Weiss (2006) claimed that low energy AE events are related to elastic deformation. As the specimen enters into the plastic deformation region the generation of higher amplitude AE events is seen. Finally, as final failure approaches the amplitude of the AE signals and their number increase dramatically.

### 4.3 Acoustic emission and crack monitoring in rails

The AE method is widely used as a non directional NDT method. Regardless of the crack characteristic, the AE signals provide assistance for the qualitative investigation of the crack location. Anticipated AE source depends on the crack growth mechanism. When the external loads applied causes crack growth elastic waves emitted from the crack tip. In Figure 27, crack initiation and crack growth caused by train axle loads cause acoustic signals to be emitted. However, acoustic emissions will also be generated due to the rolling noise of the train itself as well as from its suspension movement.

Firstly, elastic waves propagate into all directions, and AE events are caught by the piezoelectric sensors. Finally, all data are transferring to the preamplifier, post amplifier and software program. In the literature, a great number of scientific results proved that several sensors can be mounted to calculate arrival time of the signals to the sensor, observe the frequency alteration during the deformation process, and determine the nature of the crack (Vallen System, 2004).

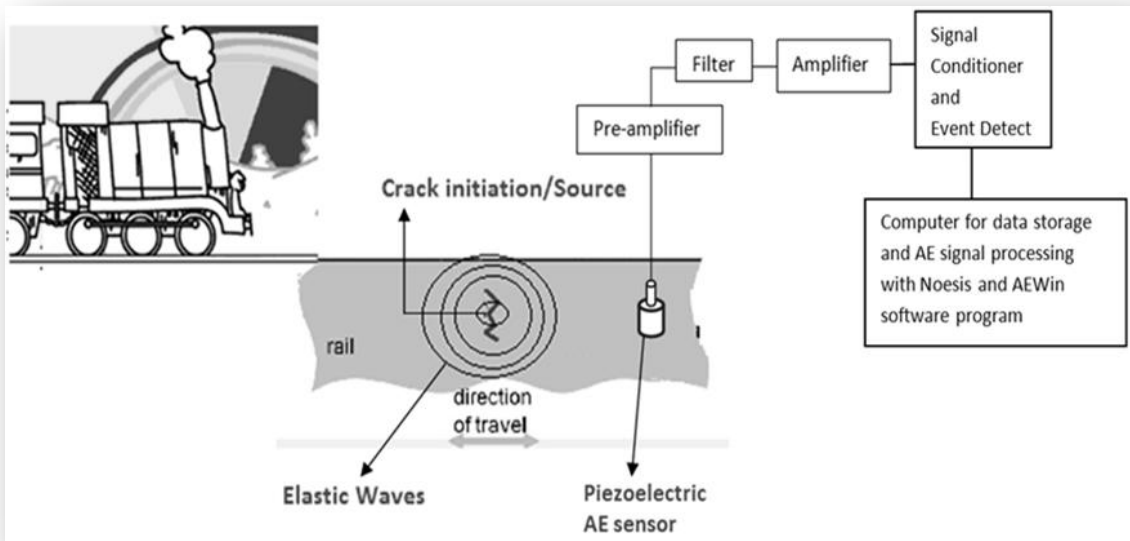


Figure 27 Application of acoustic emission for the detection and monitoring of crack initiation and crack growth in an in-service rail.

#### 4.4 Kaiser effect

Recent AE developments have led to a renewed interest in the effect of cyclic loading. Depending on the properties of the material, Kaiser Effect should be taken into consideration for heavy loaded applications. The impact of the Kaiser effect for this project should be investigated in the sense of the relationship between repeated high load and AE activity. According to previous studies, many scientific papers claimed that the fatigue cyclic load does not affect the AE results until the stress exceeds the previous level of the load. Previous load should be lower than the next load to create new acoustic signal. If the load does not change such as the duration of cycle 1 and cycle 2 seen in the Figure 28, the AE sensor cannot catch the different signal. In terms of the non-load changing situation, the AE events will be stable. In this case, cycle 3 is called as a developer of the AE event due to higher load conditions than the previous one (Puri,2003). Load and cumulative acoustic events are generally seen as an accelerating step, during the overlap loading Loaded and unloaded methods have led to the establishment of the Kaiser Effect, due to the deformation mechanism, when the crack is propagating.

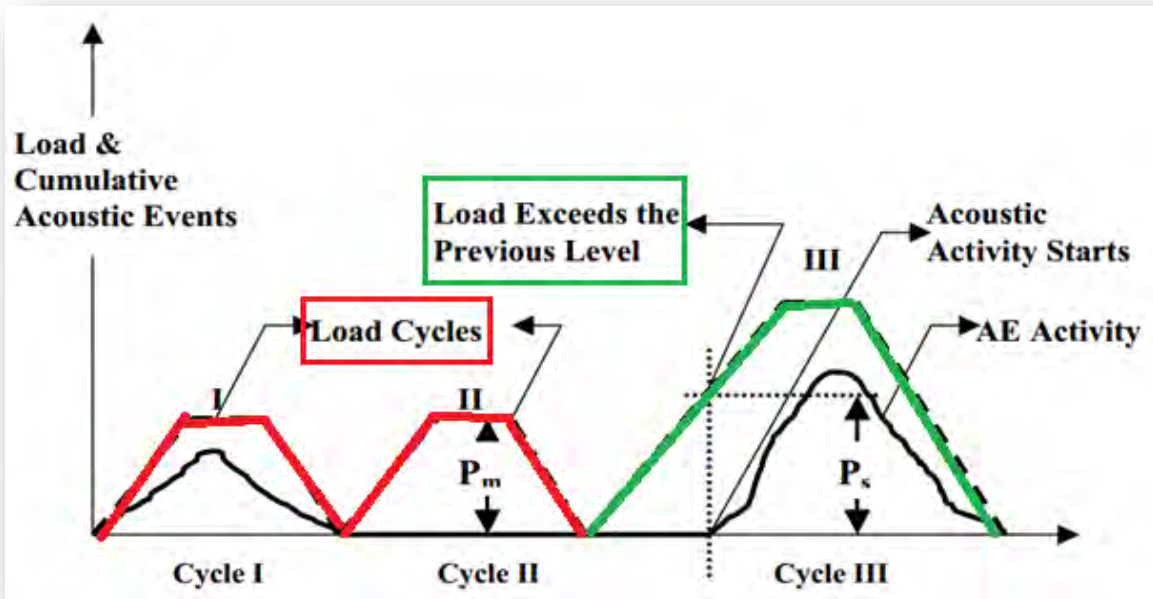


Figure 28 Illustration of Kaiser Effect (Puri, 2003)

Moreover, Puri, et al. (2006) analysed the correlation between acoustic emission and stress value. In Figure 29, stress curve is divided in 4 different regions which are relevant to the elastic and plastic deformation. AE signals are investigated to explain the different energy level due to the different deformation mechanism. Reversible energy transmission on the elastic deformation region does not affect the microstructural properties of the specimen. Thus, stress application increases until severe cracking occurs. If the structural integrity is destroyed due to grain boundary sliding, or grain fracture etc., dislocation can sometimes protect the specimen from failure. This phenomena called as crack closure is seen in Figure 29 from A to B point. Puri, et al. (2006) pointed that crack closure is observed due to the high loading, and then crack initiation was seen from B to C. The curve slope is gradually increasing due to low stress level conditions. This phenomena is generally seen in a linear elastic deformation mechanism. Point C is defined as a Kaiser Effect point. Because, at this point, AE event does not influence by repeated fatigue load. After C point, crack is propagating under the repeated load conditions. Especially, in terms of the D-F region, unstable crack is propagating. Stress dramatically increases, and much more AE event can catch from the sensors due to the high cycle loading phenomena. Finally, stress exceeds the level of the ultimate tensile strength. The high number of hit was detected when permanent distortion occurred at the high fatigue cycle load conditions (Lehtonen, Cosgrove, Hudson, & Johansson, 2012).

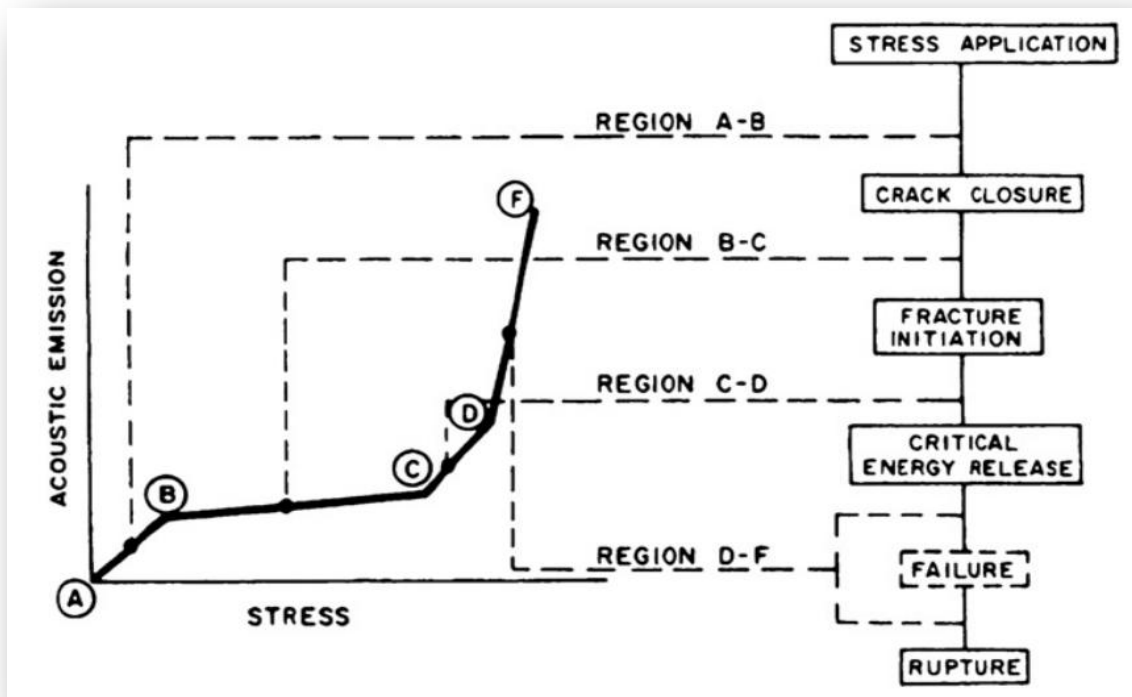


Figure 29 An example of a cumulative acoustic emission curve, Region A–B represents the closing of cracks, and B–C the linear elastic deformation. C–D is the stable, and D–F the unstable fracture propagation(Lehtonen, Cosgrove, Hudson, & Johansson, 2012)

Kaiser effect is dominant at the repeated load, so previous load should be lower than the latest load to collect the AE signal. The number of AE hit can be detected when the load increase. On the other hand, sometimes Kaiser Effect may not be active even if the loads were repeated due to Felicity Effect. During reloading conditions, latest stress level is higher than the previous one, the number of AE event does not increase. (Lehtonen, Cosgrove, Hudson, & Johansson, 2012). To explain the impact of the Kaiser Effect and Felicity Effect on the monitoring of the structural integrity, Figure 30 presents the experimental data.

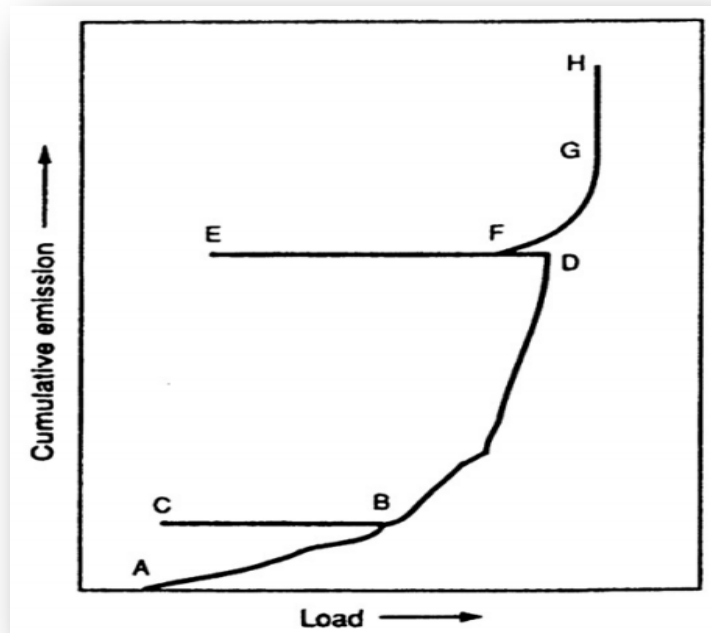


Figure 30 Kaiser Effect and Felicity Effect in a cyclically loaded specimen (Lehtonen, Cosgrove, Hudson, & Johansson, 2012; Pollock, 2003)

In Figure 30, loaded and unloaded impact on the specimen indicated in AB, BC and CB line. AB and CB lines are named as a loaded time. Kaiser Effect is dominant on the BCB repeated load line. Repeated loads implemented during BD, DE part. Load in D part is higher than the load in F part, however cumulative emission is stable. Thus, the Felicity effect is overtaken on the DEF line (Lehtonen, Cosgrove, Hudson, & Johansson, 2012; Pollock, 2003).

#### 4.5 Comparison between AE and other NDT techniques

Acoustic emission offers significant advantages over other conventional inspection techniques when internal cracks need to be monitored and evaluated. This is particularly important when long-term monitoring is required. The most important advantage of AE is that it allows in-service monitoring thus allowing inspection and maintenance cost and time reduction. It does not require personnel to carry out manual labour and can be installed in a one-off operation. AE is highly sensitive to very small crack propagation events which cannot be detected by any other means. This is probably the most important advantage of the acoustic emission technique in relation to this project.

Furthermore, it allows the monitoring of an entire structure being a global testing method. It also permits the localisation of any defects present using linear location, triangulation or zonal location. Under certain conditions quantitative information regarding the crack behaviour and propagation rate may be obtained but this information should be treated with extreme care particularly in the presence of background noise. Table 3 summarises the main differences between conventional inspection methods and AE techniques.

Table 3 Characteristics of acoustic emission inspection compared with other inspection methods(Pollock, 2003)

<b>Acoustic Emission Method</b>	<b>Other NDT Methods</b>
Detects movement of defects	Detects geometric form of defects
Requires stress	Do not require stress
Each loading is unique	Inspection is directly repeatable
More material-sensitive	Less material-sensitive
Less geometry- sensitive	More geometry- sensitive
Less intrusive on plant/ process	More intrusive on plant/ process
Requires access only at sensors	Requires access to the whole area of inspection
Tests whole structure at once	Scan local regions in sequence
Main problems: noise related application	Main problems: geometry related application

#### 4.6 Waveform analysis methods of AE signals

The frequency spectrum of AE signals is associated with the AE source mechanism. There are two different types of signals occurred during the AE method which are called as a transient (burst) and a continuous signal. In Figure 31, Burst signal comprises of a peak when the crack growth event takes place. Continuous signals seem as an endless signal. Continuous signal can complicate data analysis, because background noise and AE signals related to crack growth event cannot be easily separated from each other. Continuous AE signals are having same amplitude level with background noise. If the crack-related signal needs to be distinguished from the back ground noise, a filtering system should set up. In general, having a sharp peak is sufficient to explain whether crack growth has taken place (Vallen Systeme GmbH, 2002).

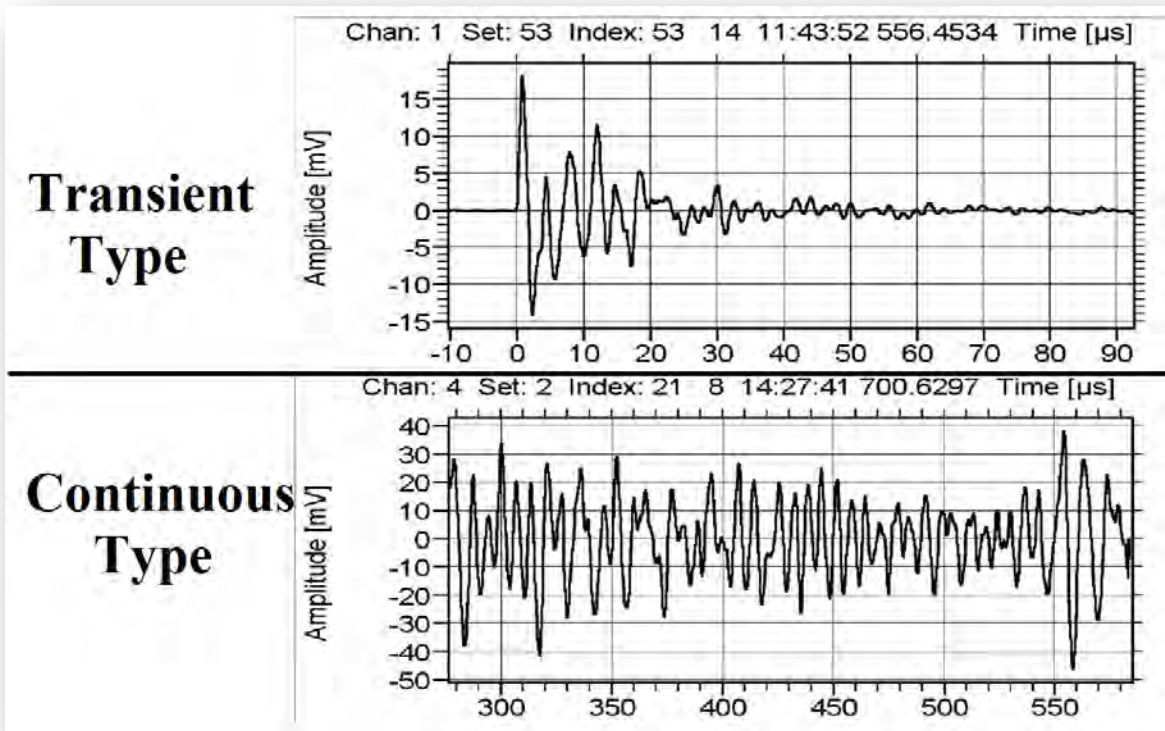


Figure 31 Transient (top) and continuous (bottom) type of AE signal(Vallen Systeme GmbH, 2002)

Amplitude versus time represents the statistical value of the AE signal. Continuous signal comprises of the background noise such as friction or flow noises during the experiment, on the other hand, burst signals give information about the crack propagation. The peak values of the burst signals are higher than the value of the continuous signal. Therefore, burst signals can be used to determine the evolution of the deformation process (Han, Luo, & Wang, 2011).

## 5 Three-point and four-point bending tests

### 5.1 Experimental method and results

In order to assess the applicability of the AE technique for detection and subsequent monitoring of crack growth in steel 3-point and 4-point bending fatigue tests were carried out under laboratory conditions. Several rectangular bar-shaped specimens were extracted from 260 grade rail steel (0.7C and 1.0Mn in wt %) with dimensions 100mm (Length) x 10mm (Width) x 10mm (Height). As can be seen in Figure 32, the specimens were extracted from the web plane of the rail steel. All specimens were cut in the longitudinal orientation of the rail. A centre notch of at 30° angle and 2 mm depth was machined perpendicular to the rail web plane to act as fatigue crack initiation point. The nominal mechanical properties of the 260 grade rail steel are given in Table 4 (Vitez, Krumes, & Vitez, 2004).

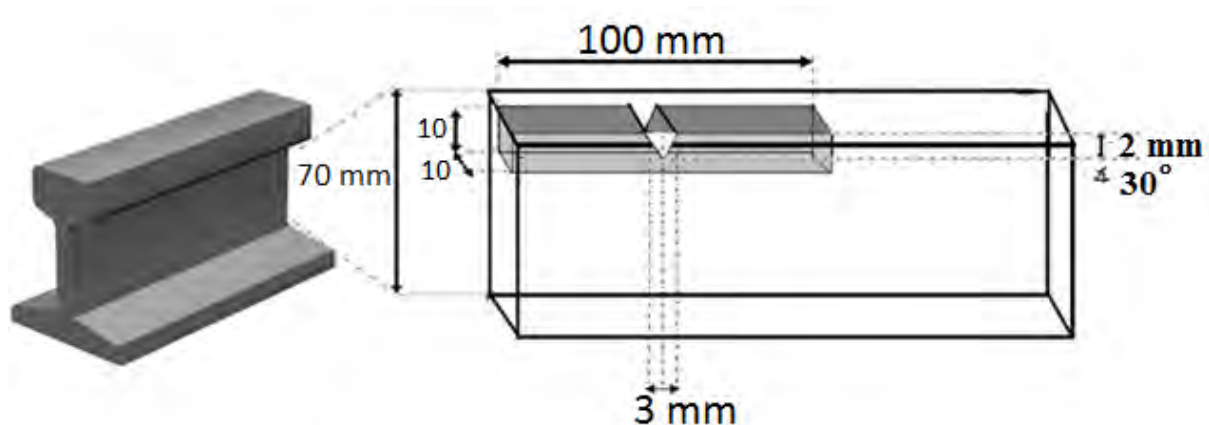


Figure 32 Specimen extraction for flexural testing

Table 4 Typical requirement of mechanical properties(Vitez, Krumes, & Vitez, 2004; Mesteel, Unknown)

<b>Maximum Fracture Toughness</b>	35MPam <sup>0.5</sup>	<b>Minimum Fracture Toughness</b>	30 MPam <sup>0.5</sup>
<b>Minimum Tensile Strength</b>	≥ 1.040 MPa	<b>Minimum Elongation At Rupture</b>	9%
<b>Yield Strength</b>	≥ 608 MPa	<b>Brinell Hardness</b>	320-360HB

Microscopy samples were also cut from the same rail section used to manufacture the rectangular bar specimens in order to assess the microstructure. The samples were mounted on bakelite and then polished down to 1 $\mu$ m using Struers polishing clothes and diamond suspensions. The polished samples were then etched with 1% nital to reveal the microstructure. The etched samples were examined using a Karl Zeiss optical microscope with digital imaging capability. From the optical micrographs shown in Figure 33 the microstructure is clearly predominantly pearlitic. This type of rail steel exhibits relatively good resistance to wear due to the small interlamellar spacing between ferrite and cementite as well as the presence of hard carbides which increase the overall hardness. The average hardness of the samples was found to be 259 HV30 which is within the limits specified by the standards for this particular rail steel grade.

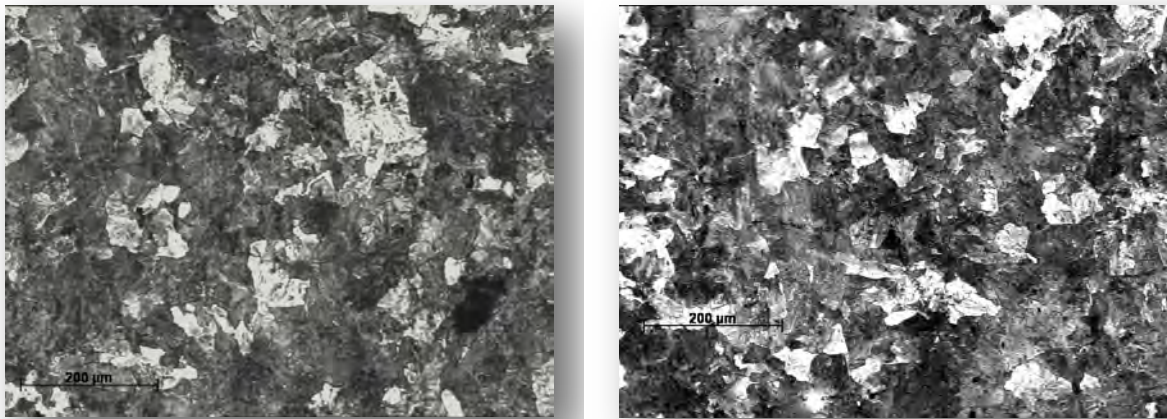


Figure 33 The microstructure of the rail tested showing ferrite and pearlite (etched using 1% Nital).

Three and four-point fatigue bending tests are representative tests for simulating of crack evolution due to the externally applied forces when the train runs over the damaged rail section. Before the fatigue bending tests are carried out the specimens are pre-cracked using a Vibrophore machine using rapid cyclic loading. The crack initiates in the notched area which acts a stress raiser during the pre-cracking process as discussed next.

## 5.2 Pre-cracking method

In order to initiate a crack at the area of the notch the specimens were placed in an Amsler 20kN Vibrophore electro-mechanical high frequency fatigue machine. The testing configuration used was based on 4-point bending with span distances 20mm and 40mm

respectively. To calculate the correct loading parameters so as to initiate a fatigue crack rapidly the maximum fracture toughness of the specimens was considered to be within the range of 30 – 35 MPam<sup>0.5</sup> as mentioned in the British standards for rail manufacturing. The stress intensity factor required to cause crack initiation was calculated using Equation 17 and Equation 18 for three and four point bending respectively. The loading ratio employed was R=0.1. The fatigue loading pattern during the pre-cracking process was sinusoidal, at approximately 100Hz. Crack initiation and crack growth was monitored using microscopy replicas which were taken at various intervals. The cracks were allowed to grow between 0.2-1mm depending on the specimen before being removed from the Vibrophore machine. In Figure 34, the schematic image of the specimen presents that B is named as thickness, W is the width of the specimen, and a<sub>N</sub> is the notch length.

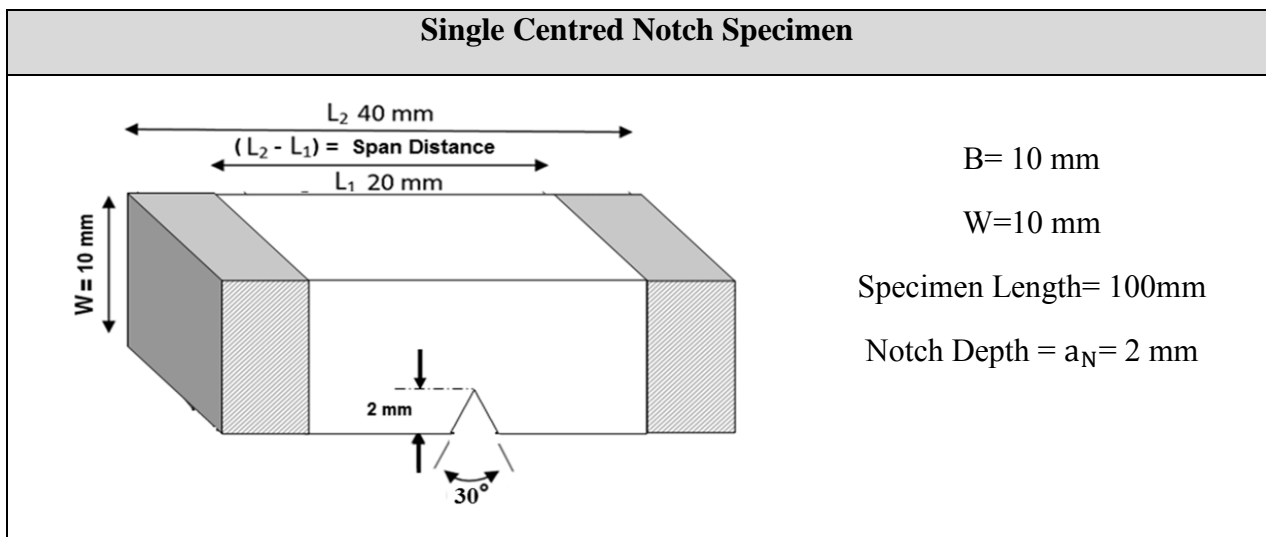


Figure 34 Schematic image of the single centred notch specimen

Obviously AE tests could not be easily carried out during the pre-cracking process due to the high levels of background noise and therefore no AE signals were recorded under these conditions. It may be useful in the future to carry out some AE tests under these conditions in order to evaluate the effect of high-amplitude background noise on the AE signals arising from crack growth events. Figure 35 shows the experimental setup during the pre-cracking process. It should also be noted that continuous crack monitoring during the pre-cracking process was attempted using a portable digital microscope supplied by Proscope. Unfortunately due to the vibrations during cyclic loading it was not possible to resolve the crack itself and therefore microscopy replicas were used instead.



Figure 35 Experimental configuration of Vibrophore machine

The stress intensity factor was calculated for 4-point bending test using Equation 13 (Ewalds & Wanhill, 1989).

Equation 13

$$K = (\sigma\sqrt{a})f(a/W)$$

To calculate the bending stress, Equation 14 is used for four-point bending test (Ewalds & Wanhill, 1989).

Equation 14

$$\sigma = \frac{3P \left( \frac{L - L_i}{2} \right)}{BW^{3/2}}$$

where P is the applied force, L is the supporting span length, Li is the loading span length, B is the thickness and W is the width of the specimen. Using Equation 14, Equation 13 can be written then as follows (Equation 15):

Equation 15

$$K = \frac{3P \left( \frac{L - L_i}{2} \right)}{BW^{3/2}} f(a/W) = \frac{3P \left( \frac{L - L_i}{2} \right)}{BW^{3/2}} Y$$

According to the specimen dimensions then the geometrical factor is calculated using Equation 16 and then maximum and minimum applied load level is found as seen in Table 5. If the maximum allowable value of K is assumed to be between 30 – 35 MPam<sup>0.5</sup> then by solving the above equations below for 4-point bending maximum and minimum tolerable loads are found to be 12kN and 14kN respectively.

Equation 16

$$Y = 1.99(\alpha_N/W)^{1/2} - 2.47(\alpha_N/W)^{3/2} + 12.97(\alpha_N/W)^{5/2} - 23.17(\alpha_N/W)^{7/2} + 24.87(\alpha_N/W)^{9/2}$$

$$Y = 0.835$$

Table 5 The bearable fatigue loads of single centred notch rail specimen

<b>For <math>K_{max} = 35MPam^{0.5}</math></b>	<b>For <math>K_{Min} = 30MPam^{0.5}</math></b>
$P_{MAX} = \frac{K_{Max}BW^{3/2}}{3\left(\frac{(L - L_i)}{2}\right)Y}$	$P_{Min} = \frac{K_{Min}BW^{3/2}}{3\left(\frac{(L - L_i)}{2}\right)Y}$
$P_{MAX} = 14 \text{ kN}$	$P_{Min} = 12 \text{ kN}$

Given the above a cyclic loading of minimum 1.05kN and maximum 10.5kN (R=0.1) was selected in order to cause crack initiation rapidly.

### 5.3 Three-point and Four-point bending test set up

After the desirable crack length had been obtained the specimens were removed from the Vibrophore machine and fixed on a Dartec 50 kN Servo-Hydraulic Universal Test Machine. During pre-cracking with the Vibrophore machine the maximum and minimum applied cyclic loads were determined based on the length of notch which acted as a stress raiser at its tip ( $\alpha_N$ ). However, to calculate the appropriate maximum and minimum load level, the loading range needed to be recalculated for both 3-point and 4-point bending configurations given the new crack length dimensions,  $a_0$  comprising the notch length,  $a_N$  and length of the crack,  $a_p$  that formed during the pre-cracking process. . Because, the geometrical factor is influenced from the length of the crack, henceforth new loading values need to be determined before the fatigue tests are carried out. The schematic image of the pre-cracked notch specimen is given in below.

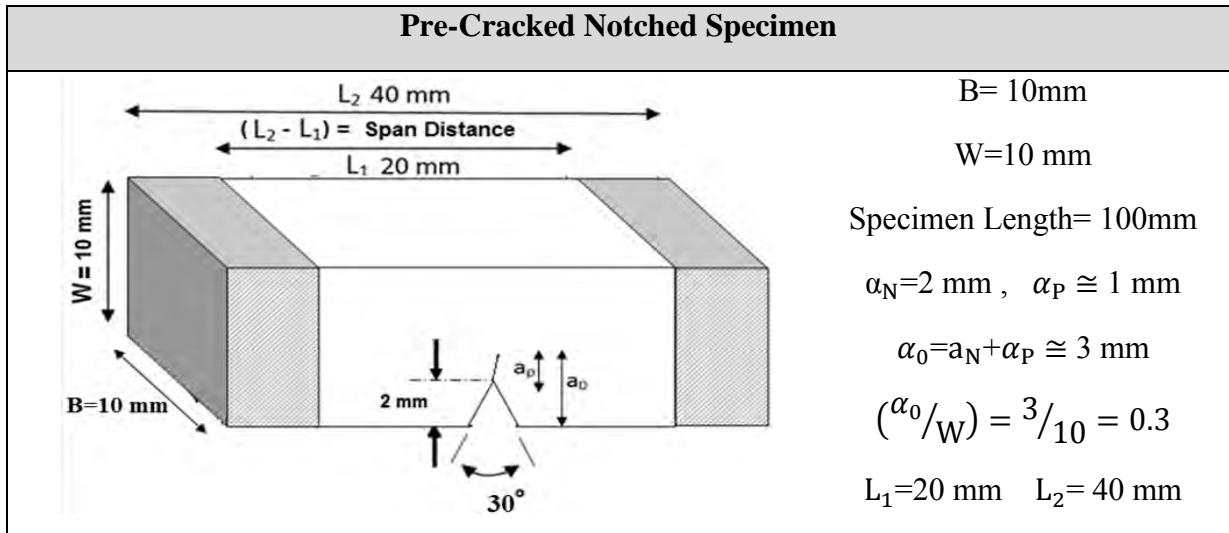


Figure 36 Schematic image of the pre-cracked notch specimen

During 3-point and 4-point fatigue tests, a trapezoidal loading configuration is employed to minimise the effect from machine noise as shown in Figure 37. The load was controlled at 1s intervals thus a complete loading and unloading cycle would take 4s (1s rising, 1s kept at maximum load, 1s dropping, 1s kept at minimum load).

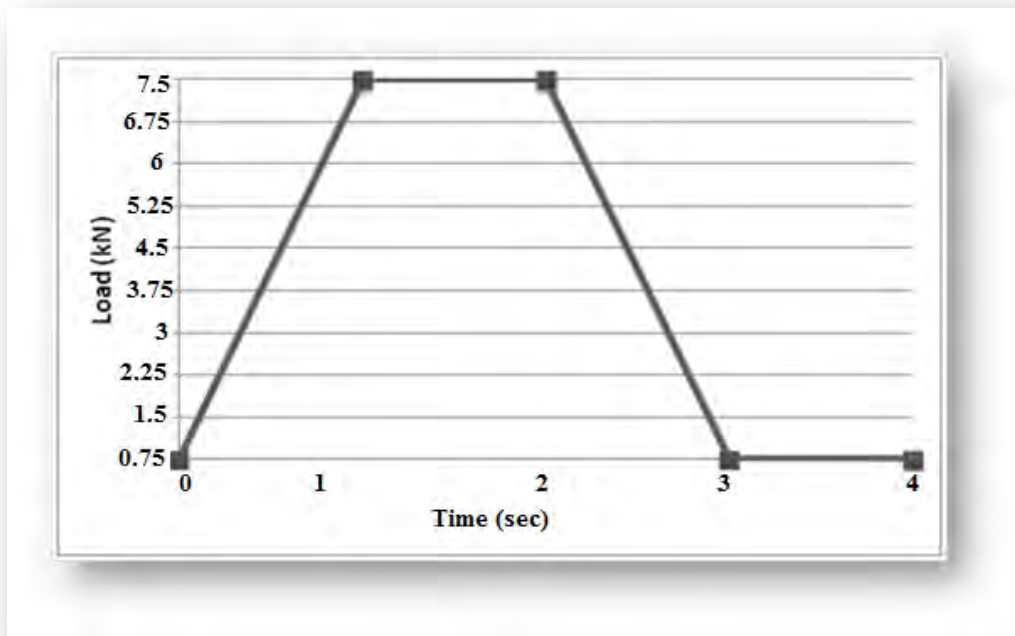


Figure 37 Four-point bending test using trapezoidal loading cycle

Loading changes slowly rather than the Vibrophore machine due to the low frequency work conditions. To observe the applied load level and the number of cycles, the 18 bit Phoenix Alpha digital control system and data acquisition unit is enabled after setting up the specimen. At a later stage, due to a fault in the hydraulic pump of the Dartec, 4-point fatigue bending tests were carried out using an ESH 20kN Servo-Hydraulic Universal Test Machine with an analogue control system. The photographs in Figure 38 illustrate the experimental setup for the 3-point and 4-point bending tests.

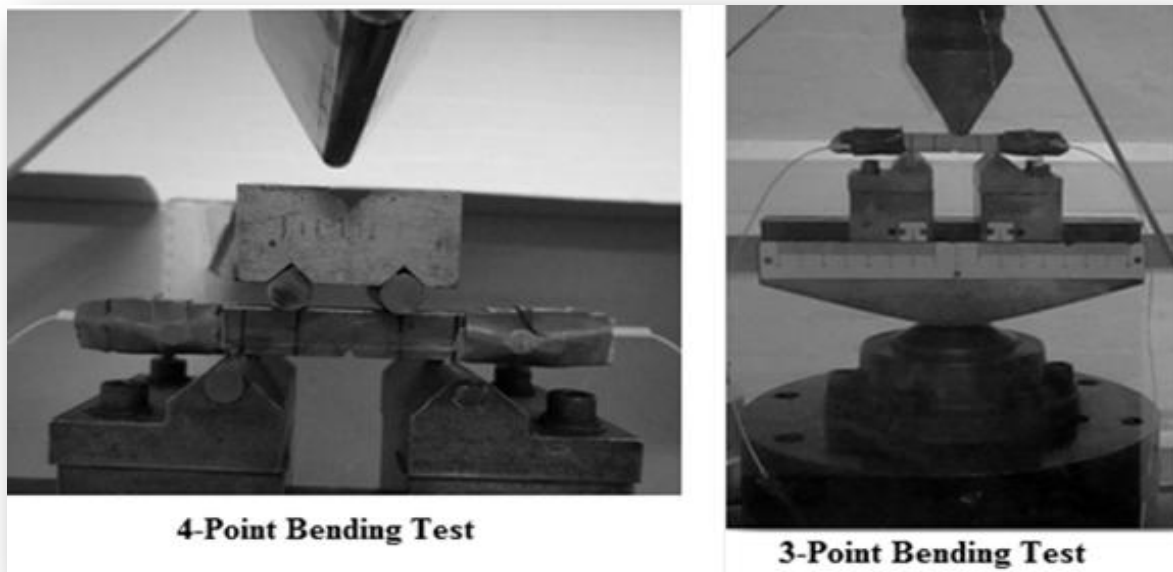
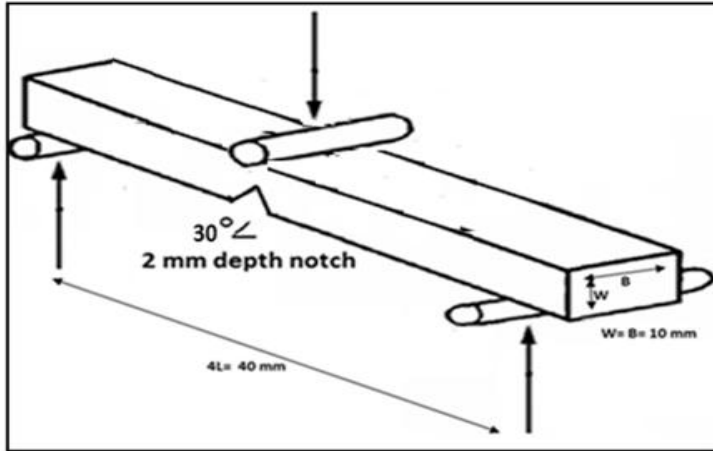


Figure 38 Experimental configuration for three and four point bending test

The reason of using two different types of bending load application was to determine the effect of the stress distribution in the damaged region. In Equation 17 and Equation 18, the geometrical factor  $Y$  is given separately given and then used to determine the maximum and minimum fatigue load. Consequently, the maximum load was determined at 10.695kN for 4-point bending test for the specimen with the smallest crack length 0.2mm. For the specimens with crack lengths around 1mm a maximum load of 7.5kN was determined to be permissible. For 3-point bending tests it was determined that a maximum load of 5kN was permissible. The loading ratio in all cases was 0.1.

Equation 17 Geometrical factor and maximum minimum bearable load calculations for 3point bending test

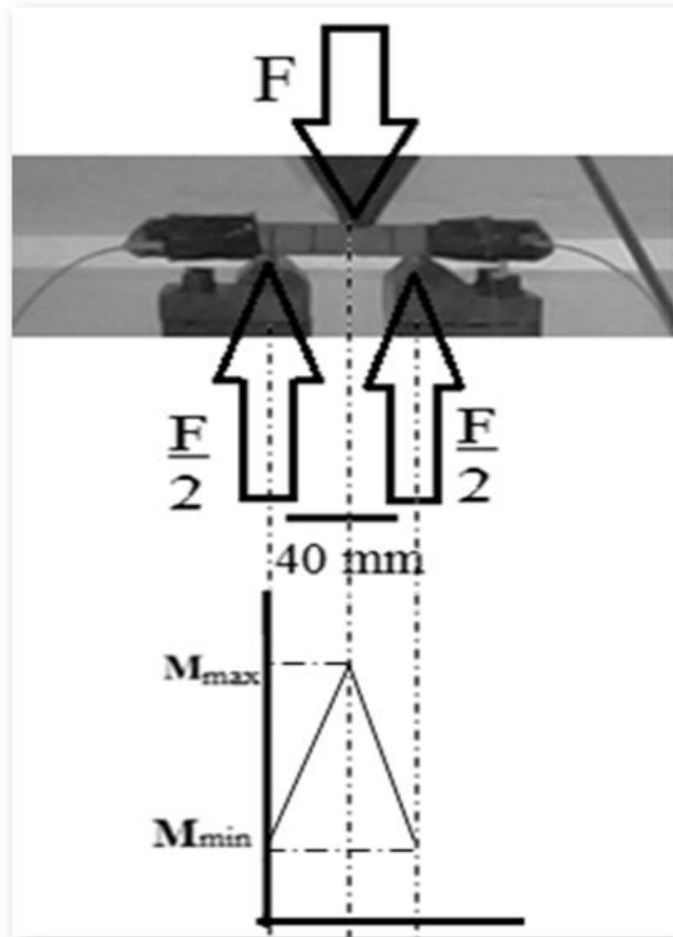


**For**  
**3 – Point Bending Test**

$$K = \sigma Y \sqrt{\alpha_0}$$

$$\sigma = \frac{3PL}{2BW^2}$$

$$K = \frac{6P}{BW} (\alpha_0)^{1/2} Y$$



$$\text{For } K_{max} = 35 \text{ MPam}^{0.5}$$

$$P_{MAX} = 5.0478 \text{ kN}$$

$$\text{For } K_{Min} = 30 \text{ MPam}^{0.5}$$

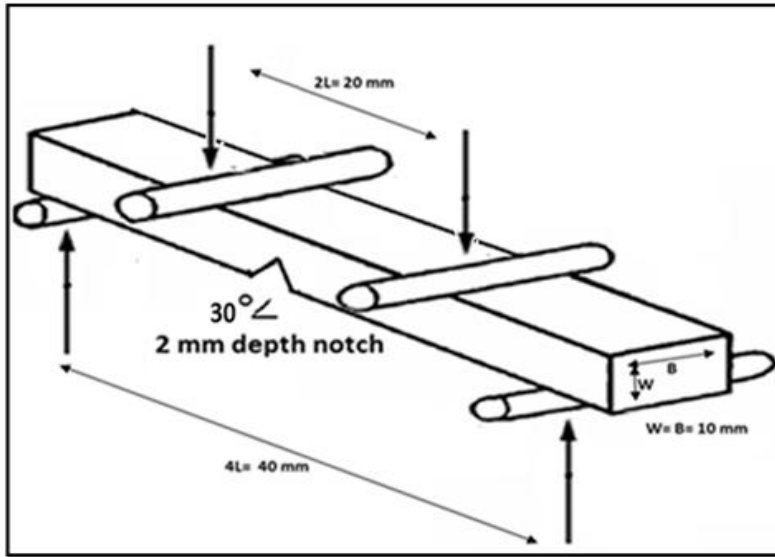
$$P_{Min} = 4.326 \text{ kN}$$

Geometrical factor for 3 – point bending test

$$Y = \frac{1.99 - \left( (\alpha_0/W) (1 - (\alpha_0/W)) (2.15 - 3.93(\alpha_0/W) + 2.7(\alpha_0/W)^2) \right)}{(1 + 2(\alpha_0/W)) (1 - (\alpha_0/W))^{3/2}}$$

$$Y = 1.284$$

Equation 18 Geometrical factor and maximum minimum bearable load calculations for four point bending test

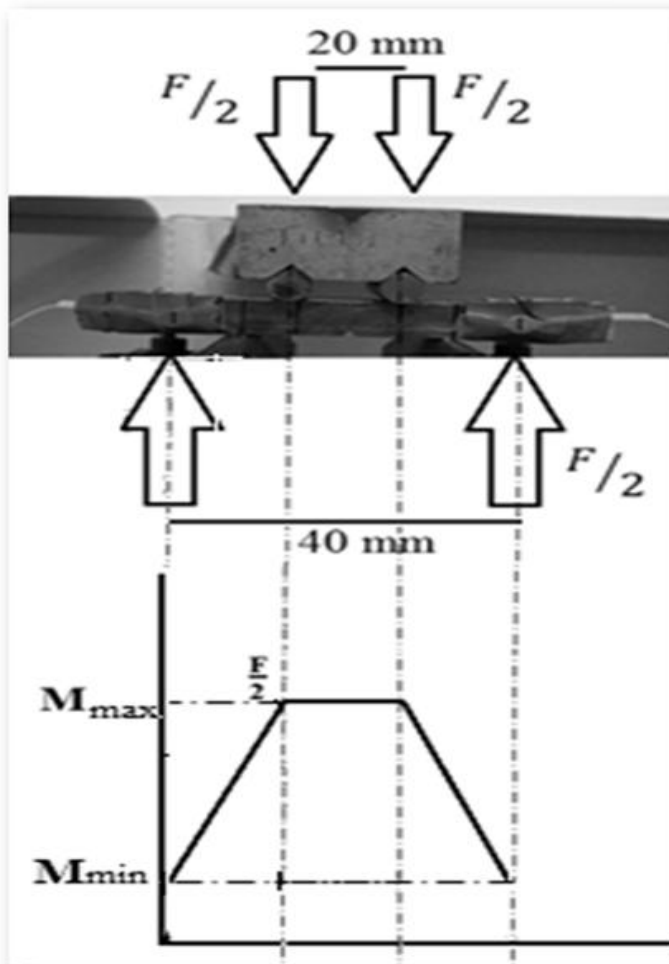


**For**  
**4 – Point Bending Test**

$$K = \sigma Y \sqrt{\alpha_0}$$

$$\sigma = \frac{3P \left( \frac{L - L_i}{2} \right)}{BW^{3/2}}$$

$$K = \frac{3P \left( \frac{L - L_i}{2} \right)}{BW^{3/2}} Y$$



For  $K_{max} = 35 \text{ MPam}^{0.5}$   
 $P_{MAX} = 10.693 \text{ kN}$

For  $K_{Min} = 30 \text{ MPam}^{0.5}$   
 $P_{Min} = 9.165 \text{ kN}$

Geometrical factor for 4 – point bending test

$$Y = 1.99 \left( \frac{\alpha_0}{W} \right)^{1/2} - 2.47 \left( \frac{\alpha_0}{W} \right)^{3/2} + 12.97 \left( \frac{\alpha_0}{W} \right)^{5/2} - 23.17 \left( \frac{\alpha_0}{W} \right)^{7/2} + 24.87 \left( \frac{\alpha_0}{W} \right)^{9/2}$$

$Y = 0.835$

## 5.4 AE setup

A commercial four-channel AE system manufactured by Physical Acoustics Corporation (PAC) was employed during three and four-point bending tests in order to assess the waveforms arising from crack growth events. The sensors used were two Pico wideband sensors with a bandwidth range between 150 kHz-750 kHz. The sensors were coupled to the surface of the sample using grease and held in place using strong adhesive tape. The signal from the sensors was amplified using a PAC preamplifier with the gain set at 40dB. The data acquisition rate was set at  $10^6$  samples per second. The Peak Definition Time (PDT) was set at  $300\mu\text{s}$ , Hit Definition Time was set at  $600\mu\text{s}$  and Hit Lockout Time (HLT) was set at  $1000\mu\text{s}$ . Throughout the tests R was maintained at 0.1. In Figure 39, Experimental configuration of Dartec 50 kN servo-hydraulic universal test machine is presented below.

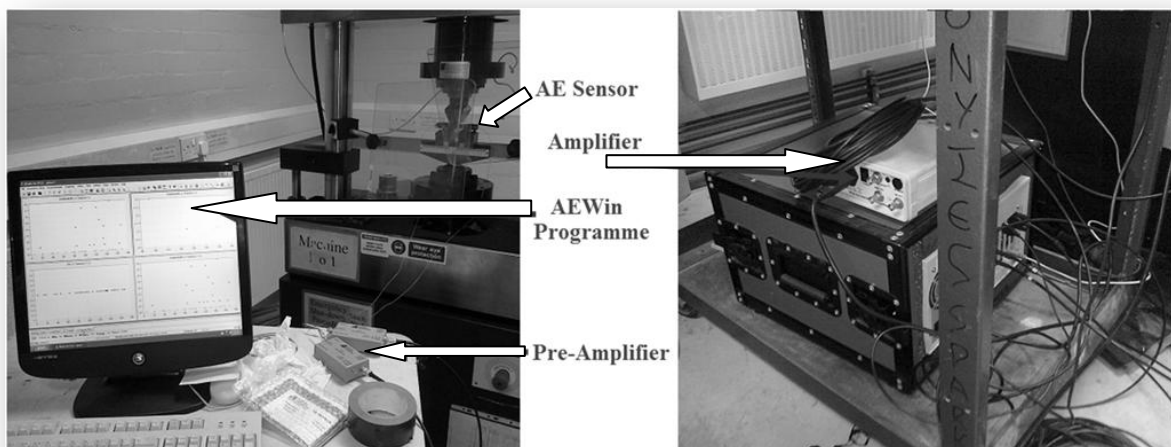


Figure 39 Experimental configuration of Dartec 50 kN servo-hydraulic universal test machine

The above parameters are extremely important in determining what constitutes a hit during the acoustic emission test. If the hit definition time is set too high then certain AE events occurring at very near time intervals from each will be merged in one single hit. On the other hand if hit lockout time is set too high then some hits could be missed if they occur at time intervals within the HLT time limit. If the HLT is too low then it is possible depending the type of the sample in terms of material, shape, size and geometry that echo from the same event might be recorded as lower amplitude hits giving an erroneous AE activity. In a similar fashion PDT will also influence the number of hits recorded. Therefore, the aforementioned parameters need to be carefully selected. These parameters are material dependent so for a different type of material different definition times should be used (Mistras Group Inc, 2009)

The AE sensors were mounted approximately 30mm away from the centre of the sample, one on either side of the cracked region. The AE amplitude threshold during recording was set as 40dB to minimise the number of mechanical noise-related hits being recorded during tests. The AE data were logged and displayed using AEWIn software also supplied by PAC. Raw AE data acquired using AEWIn software were subsequently analysed using NOESIS software supplied by Envirocoustics, member of the PAC Group (now Mistras Hellas).

Table 6 shows the applied cyclic loading range for the 3 and 4-point bending tests carried out. The total number of loading cycles is also reported. Initially, first three specimens were analysed under 3-point bending load, and then the rest of the specimens were loaded under a 4-point trapezoidal bending test.

Table 6 Applied cyclic loading range for the 3 and 4-point bending tests

Specimen	Number of samples		Number of cycles	Time (s)		$P_{MAX}$	Mean load	$P_{MIN}$
						Maximum Load (kN)		Minimum Load (kN)
Grade 260	3-Point Bending	1st	9917	39668	$R = P_{MAX} / P_{MIN} = 0.1$	3.5	1.9	0.35
		2nd	6750	27000		3.5	1.9	0.35
		3rd	8644	34576		Starting from 3.5 until 4.5	-	Starting from 0.35 until 0.45
	4-Point Bending	1st	55248	352992		9	4.95	0.9
		2nd	0.5	1		8.5	4.675	0.85
		3rd	635	2540		10.5	5.775	1.05
		4th	908	3632		10.5	5.775	1.05
		5th	10025	40100		7.5	4.125	0.75

## 5.5 Three-point bending test result

One of the key problems during AE testing is the presence of unwanted noise. For that reason in order to minimise the effect of background noise PICO wideband sensors with less sensitivity were chosen for the detection of AE activity during tests. Furthermore, the thickness of the samples was kept fairly small in order to keep the load levels needed to cause crack propagation as low as possible, minimising the noise generated from the machine motor. Finally, trapezoidal cyclic loading instead of sinusoidal cyclic loading was chosen to further reduce the level of background noise.

In order to verify the level of noise a bar specimen without a notch or crack present was loaded on the machine with the AE sensors mounted on its surface. The specimen was loaded up to 7.5kN using trapezoidal cyclic loading with  $R=0.1$ . AE activity was logged during this test and it was immediately clear that practically the effect of noise on the measurement was negligible. This was obvious since throughout this preliminary test no hits were recorded apart from the range of 40-41dB. In the absence of a notch or crack in the specimen tested any hits recorded would only have been related to machine noise.

Three three-point bending tests were carried out next using pre-cracked samples. The AE results for all three of them were very similar. As it can be seen in Figure 40, the AE activity recorded during testing of one of the three-point bending samples gradually increased as the crack growth rate increased. This is also what is expected since the energy being released as the crack growth rate increases, resulting in more intense AE activity. Also the amplitude of the recorded AE hits increases as the crack length gets nearer to a critical length. Very high amplitude AE signals are recorded at the end of the test once the crack length has reached a critical length and has become unstable followed by catastrophic failure of the sample.

The waveforms shown at the bottom of Figure 40 recorded for almost all hits have a typical burst-type nature which can only be related to crack growth events. The high amplitude events, i.e. above 60dB were predominantly recorded once the crack had grown fairly substantially. Nonetheless, 1A and 1B defects have already reached a substantial size so it is very likely that any further crack growth will generate high-amplitude AE events which will be above the background noise generated in the wheel-rail interface as the train passes over the damaged rail section.

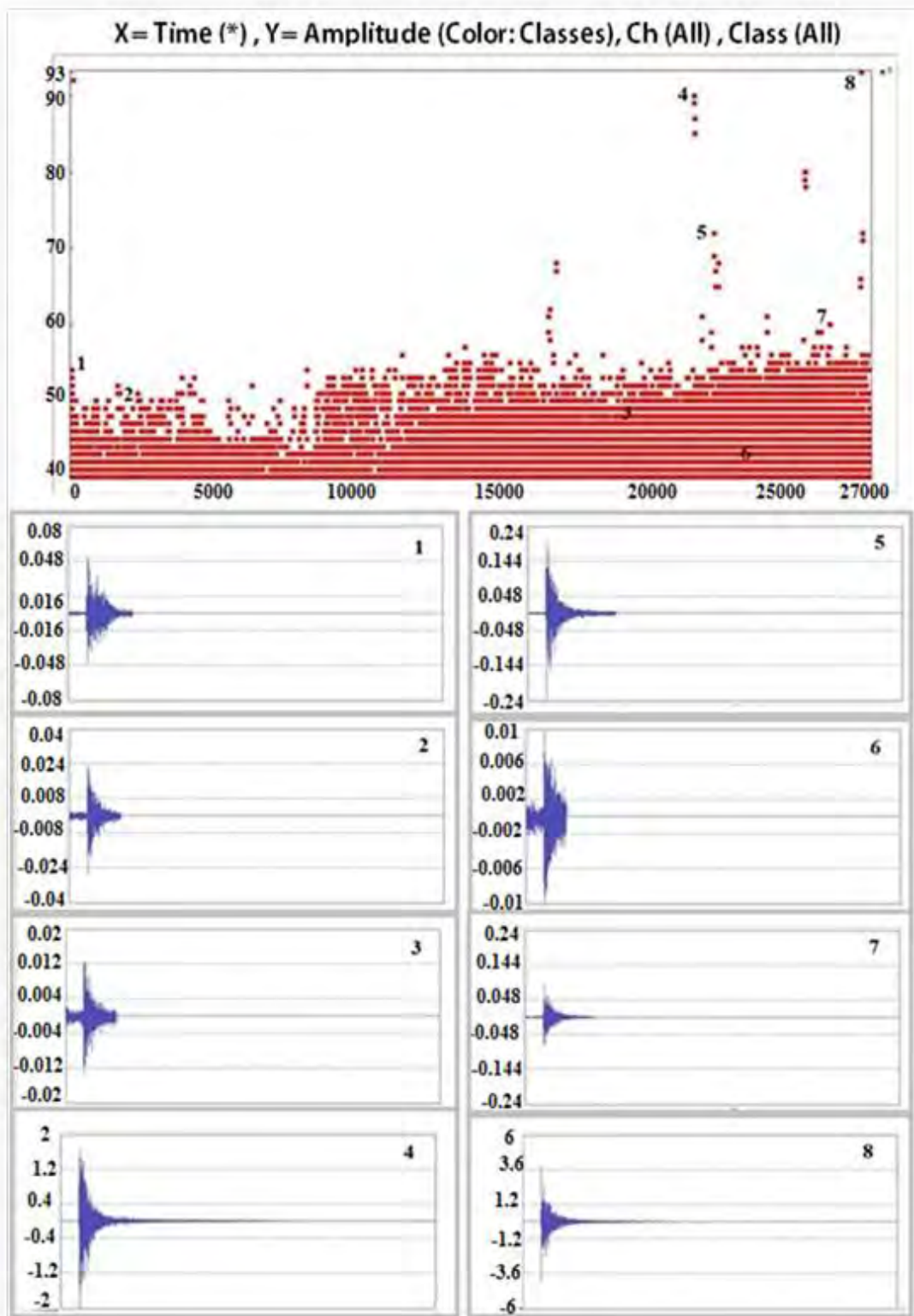


Figure 40 AE hit amplitude versus time and associated burst type waveforms

Figure 41 shows the cumulative distribution number of hits with amplitude level. It can be seen that the majority of hits has been recorded at 40-41dB and is mostly due to machine noise. Hits above that region are practically due to crack growth only.

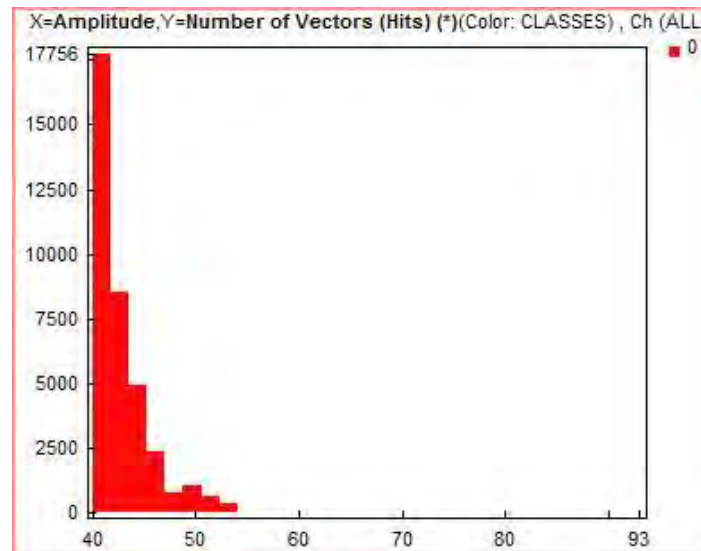


Figure 41 Cumulative number of hits with amplitude

Figure 42 shows the overall increase of AE activity with time until final failure of the sample. It can be seen that as the crack growth rate increases the amount of AE activity also increases exponentially following exactly the same pattern as the crack growth rate. In the beginning of the test AE activity is mostly linear as expected. The AE activity increases dramatically once the crack has reached a critical length.

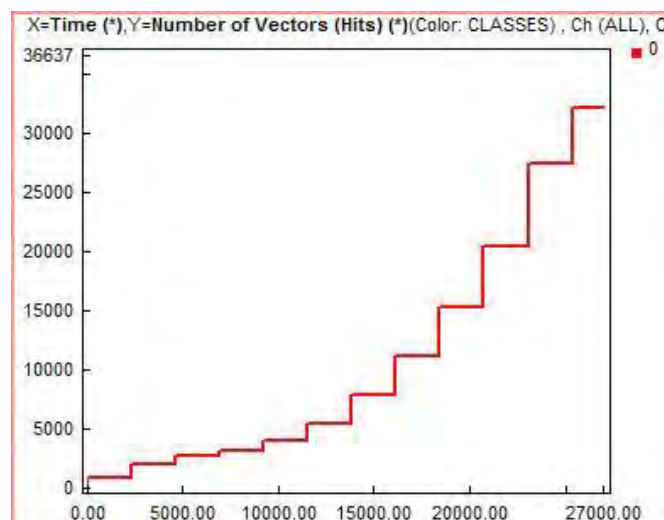


Figure 42 Cumulative number of hits recorded with time for the duration of the test

Figure 43 shows the duration of the recorded AE hits recorded during the whole test time. It can be seen that the overall duration of the recorded hits increases as the crack length and crack growth rate increases, giving rise to longer and more intense AE events.

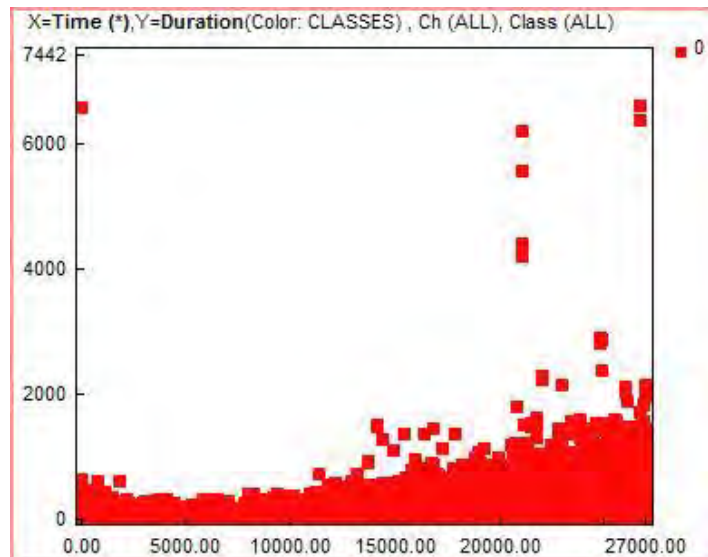


Figure 43 Duration of hits with time

Figure 44 shows the number of counts per hit with time. As expected the number of counts per hit increases in a similar pattern with hit duration. Counts per hit and duration are closely linked.

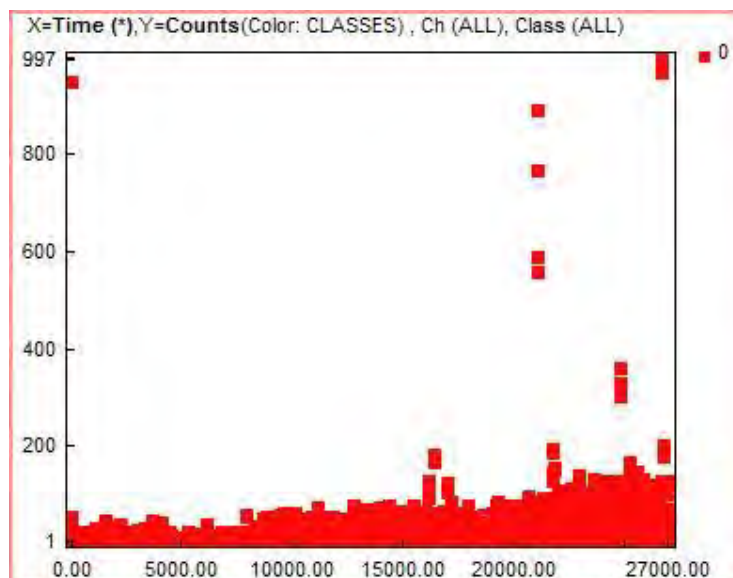


Figure 44 Counts per hit with time

Figure 45 and Figure 46 show the AE activity recorded by each of the sensors.

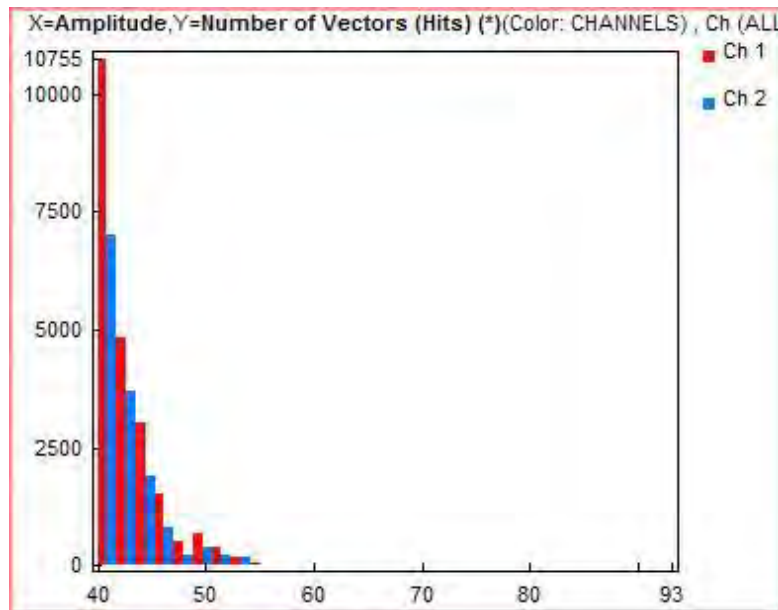


Figure 45 Cumulative number of hits with respect of hit amplitude per sensor

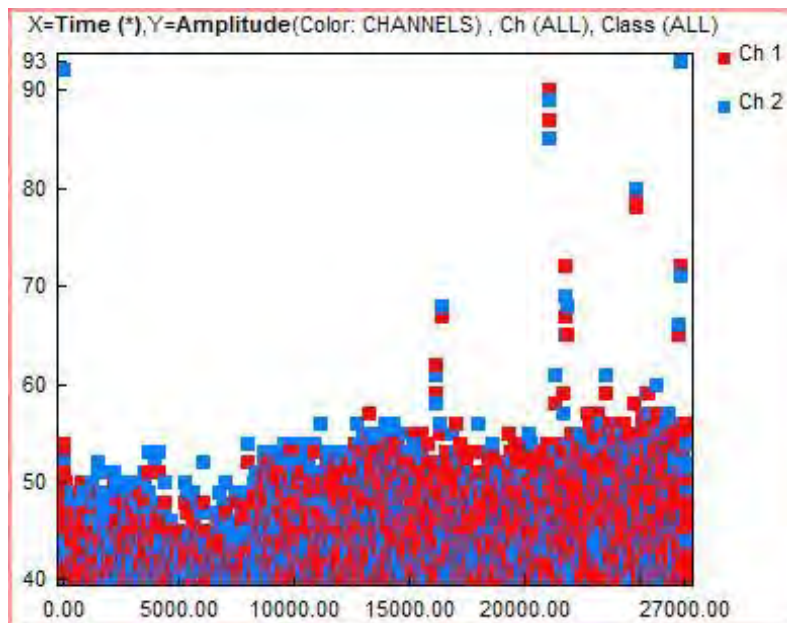


Figure 46 Amplitude of recorded AE hit with time per sensor

Figure 47 shows the increase in AE activity in terms of hit amplitude and hit duration with time per sensor. It can be seen that the amplitude of the hits recorded as well as their duration is gradually increasing. Similar AE activity is recorded by both sensors thus confirming the results.

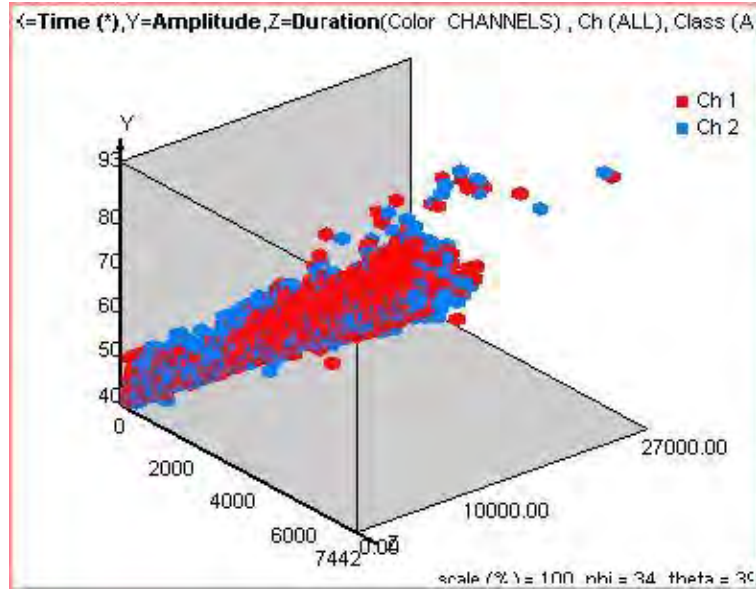


Figure 47 Hit amplitude and hit duration with test time per sensor

Figure 48 shows the density of AE hits with time. It is clear that significantly more AE activity is recorded as the crack growth rate increases. The density of AE hits will be a useful parameter in the field where background noise will have some measurable effect in the quality of the measurement.

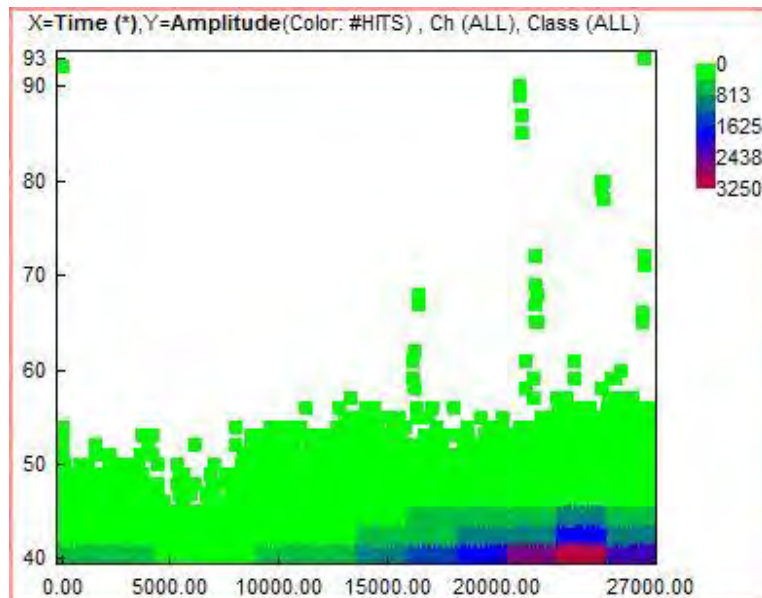


Figure 48 Density of AE hits with time

Figure 49 shows the rise time of each hit with test time. As the crack growth rate increases higher rise times are recorded. This is confirmed by both sensors.

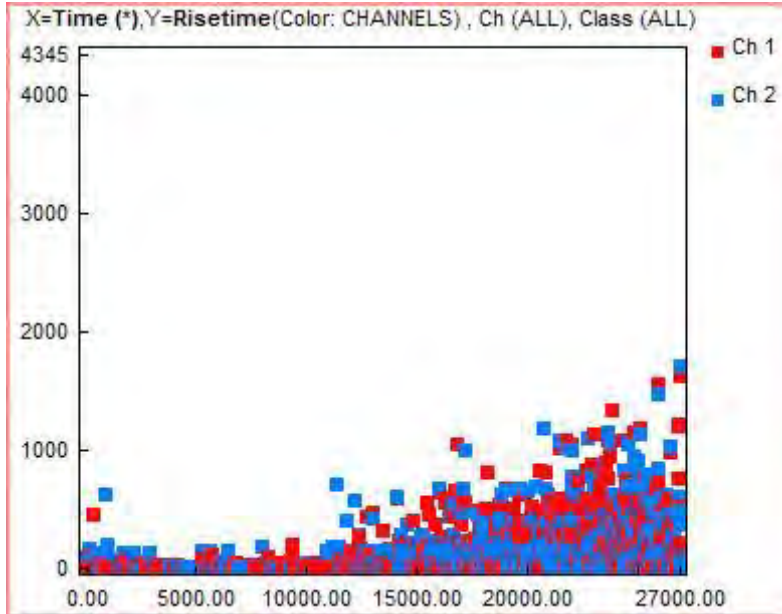


Figure 49 Hit rise time with test time for both sensors

Figure 50 shows the crack length measured. The crack propagation rate ( $da/dN$ ) showed alteration due to the initial pre-crack length. Besides of the pre-crack length, each specimen exposed to the different load. Therefore, a different measured value might be arisen by the number of cycles ( $N$ ) and final length of the crack ( $a$ ).

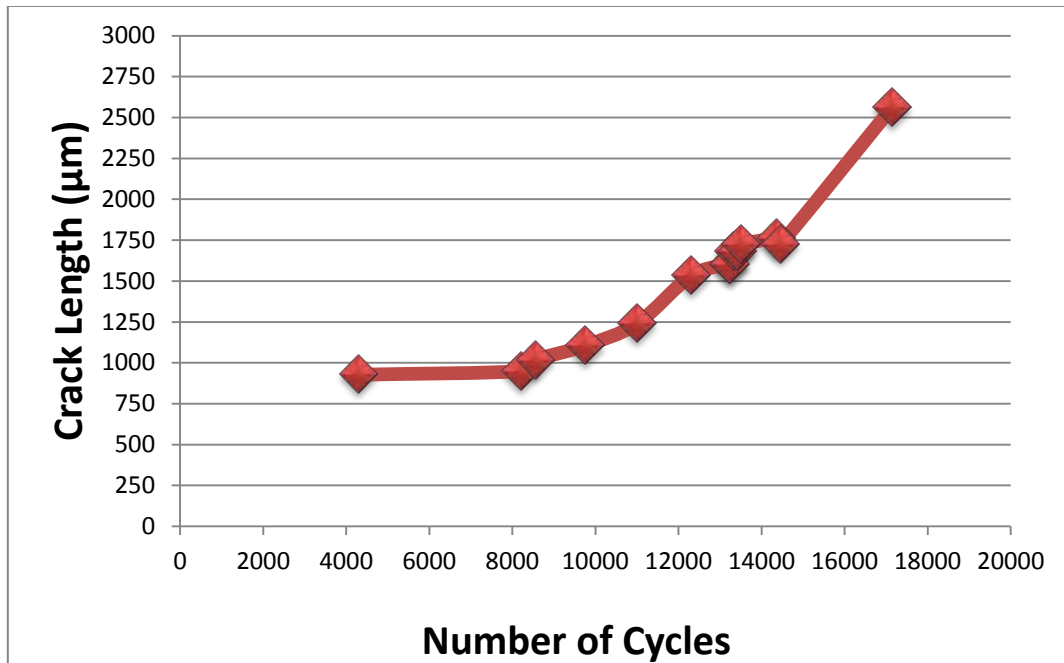


Figure 50 Crack propagation rate depending on the number of cycles for 3-point bending test

Similar AE results were obtained for all three-point bending specimens. The features of the waveforms are listed on the Table 7 High amplitude data coloured with blue. Prior to the failure, more energy was released from the cracked region, thus these signals have high energy. The duration of the hit also increases with higher amplitude hits.

Table 7 Characteristics of hits with increasing amplitude.

<i>Amplitude (dB)</i>	<i>Rise Time</i>	<i>Count</i>	<i>Energy</i>	<i>Duration</i>	<i>Frequency</i>
41	8	1	0	8	125
43	17	8	0	85	94
45	417	7	0	426	16
46	12	8	0	94	85
47	42	22	2	235	9
49	4	19	2	286	66
52	20	49	3	52	161
55	12	46	5	353	130
56	72	60	7	455	132
58	8	89	6	374	238
63	23	114	11	550	207
65	11	151	16	630	240
70	1894	337	62	3413	99
75	1864	461	95	3579	129
76	26	312	88	2182	143
77	44	381	110	2593	147
82	48	406	150	2604	156
83	54	530	207	2873	184
90	14	843	442	5613	150
93	11	844	607	5560	152
95	23	1341	968	7766	173
96	15	1106	865	6589	168
99	16	1391	1722	8412	165
99	72	1878	2064	9263	203
99	24	2017	2301	10322	195

## 5.6 Four-point bending test result

The AE results acquired for the four point bending tests are qualitatively similar to those of three point bending AE test results. Quantitatively there are some variations; however for the nature of this study they are not important. Figure 51 shows the hit amplitude versus time for one of the four point bending samples. The waveforms associated with the hits recorded are burst-type in nature indicating that they are related to crack growth propagation. Loading conditions are  $P_{max}=7.5kN$ ,  $P_{min}=0.75kN$ ,  $R=0.1$ .

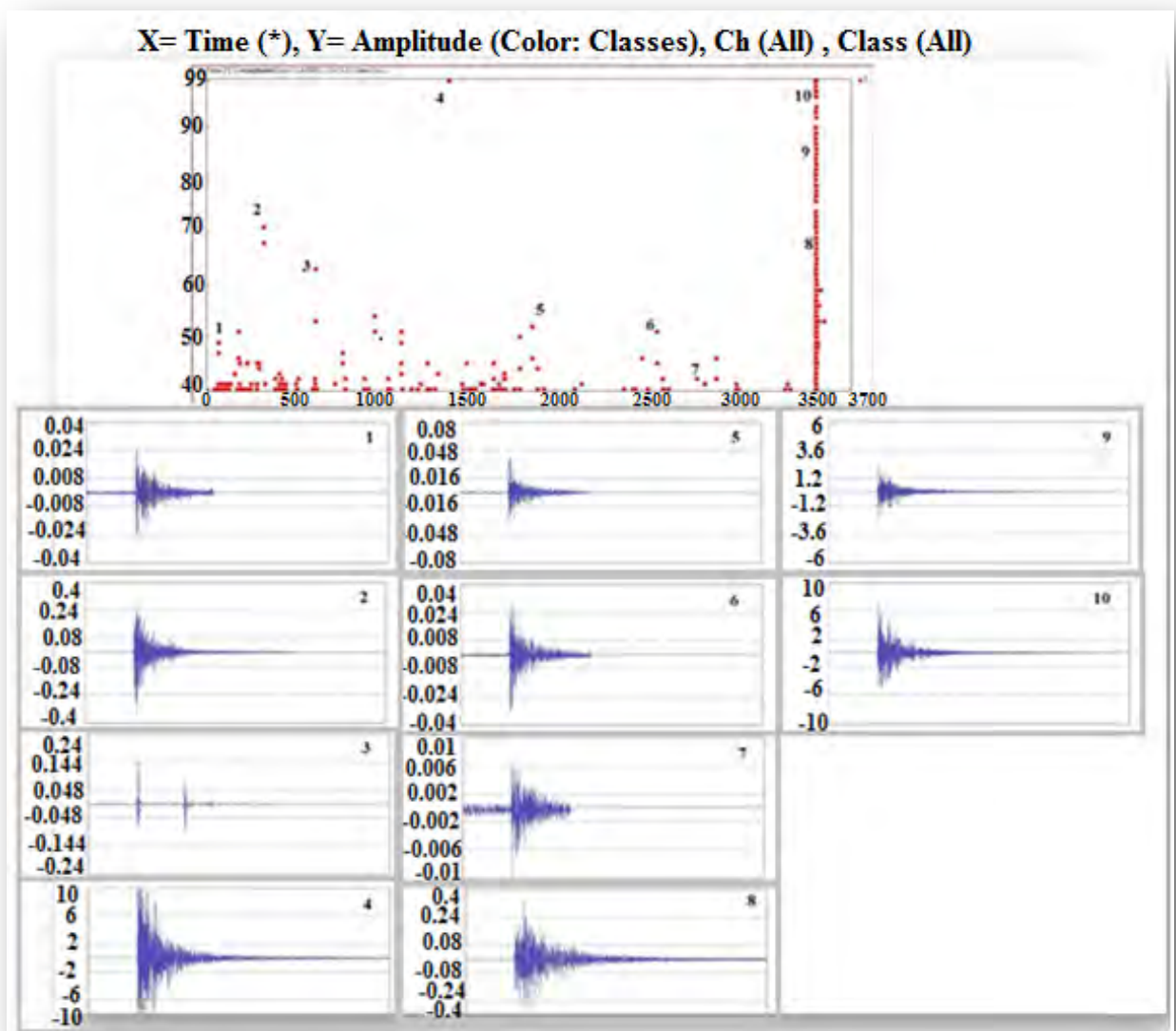


Figure 51 Amplitude versus time diagram. Bottom burst-type waveforms detected above 40dB related to crack growth events

Figure 52 shows the number of vector hits with time. Once a critical crack length has been reached substantial AE activity is recorded. Some high amplitude events are recorded at earlier stages of the experiment but they are few in number. However, the fact that high amplitude events are recorded occasionally is useful since it means that in the real life environment these events could be above the rolling noise of the passing trains.

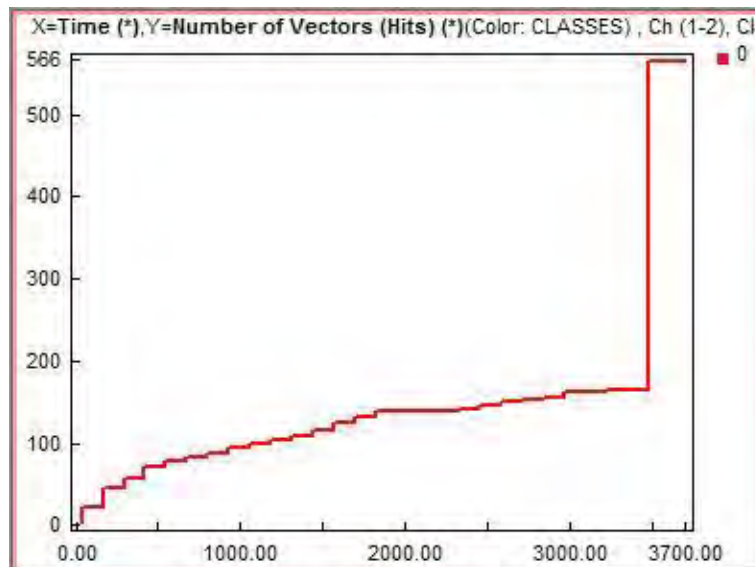


Figure 52 Number of AE vector hits recorded versus time

Figure 53 shows the crack length at 750 cycles using a microscopy replica.



Figure 53 Replica micrograph showing the crack length at 750 cycles

Figure 54 shows the distribution of the total number of vector hits with amplitude. It can be seen that there are several hits which have amplitude of 40dB. These are mostly related to machine noise.

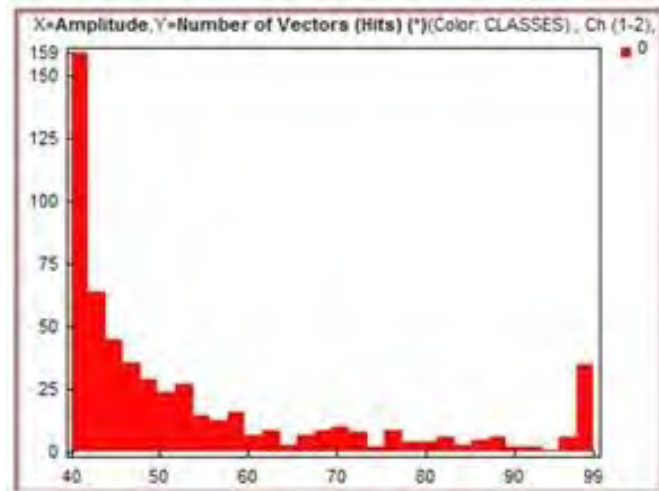


Figure 54 Distribution of number of vector hits versus amplitude

Figure 55 shows the density of hits with amplitude versus time. High density of AE activity is recorded once the crack has reached a critical length

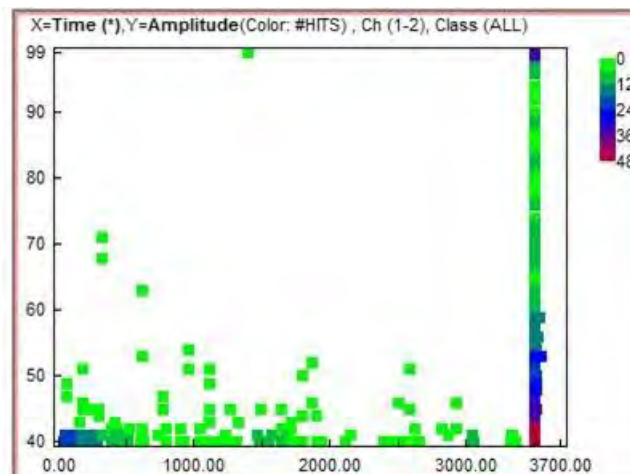


Figure 55 Density of AE hits with test time.

Figure 56 shows the duration of the recorded hits with time. It can be clearly seen that the events recorded after the crack has reached a critical size have the highest duration. In general crack growth-related AE hits have higher duration than those related to noise. This factor can be used to filter out unwanted hits.

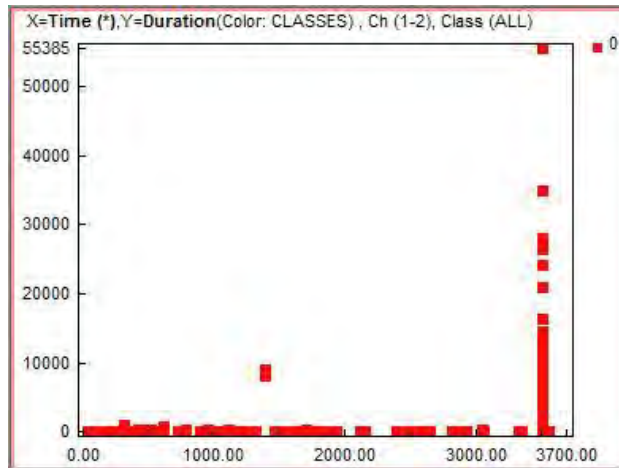


Figure 56 Hit duration versus time

Figure 57 shows the hit duration with amplitude hit. It can be seen that high amplitude hits have the highest duration. Thus the duration is a useful filtering method to remove unwanted background noise.

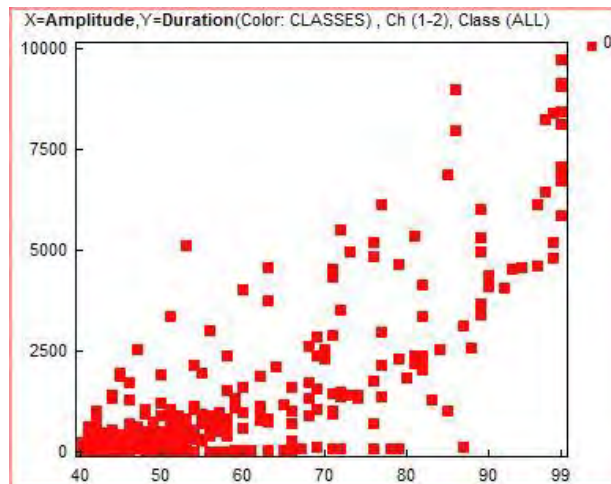


Figure 57 Hit duration with hit amplitude

Figure 58 shows the counts to peak versus hit amplitude. This is not a particularly useful parameter for filtering although higher hit amplitude are occasionally related to higher counts to peak.

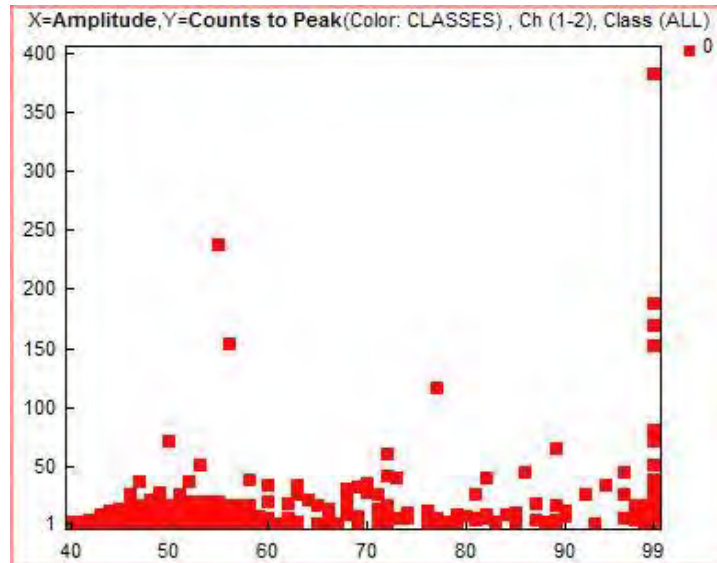


Figure 58 Counts to peak versus hit amplitude

Figure 59 shows the peak frequency of the recorded hits with test time. Low peak frequencies may be related to both low and high amplitude hits therefore peak frequency is not necessarily useful in filtering unwanted noise. The peak frequency parameter needs to be investigated further.

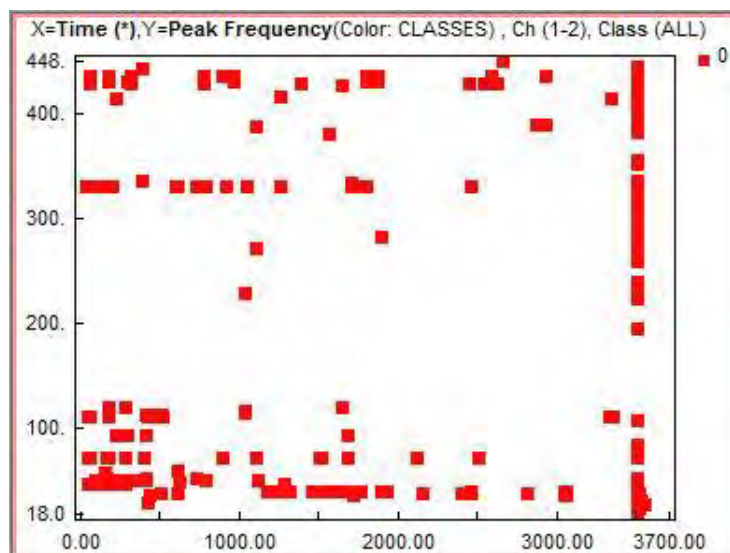


Figure 59 Hit peak frequency with test time

The diagram in Figure 60 shows the hit amplitude and hit duration with test time per sensor. It can be seen that the hit duration increases with higher hit amplitude.

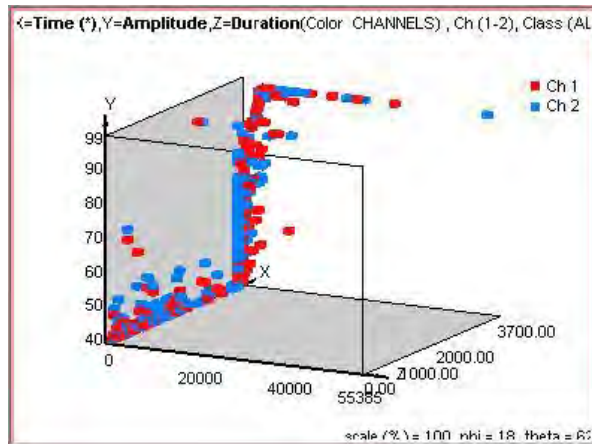


Figure 60 Hit amplitude and hit duration with test time per sensor

Figure 61 shows the four-point bending sample after final failure. The fatigue area at which the crack gradually with every loading cycle grew is clearly visible at the first 3mm. At that point the crack reached a critical size followed by rapid propagation and brittle fracture of the sample.

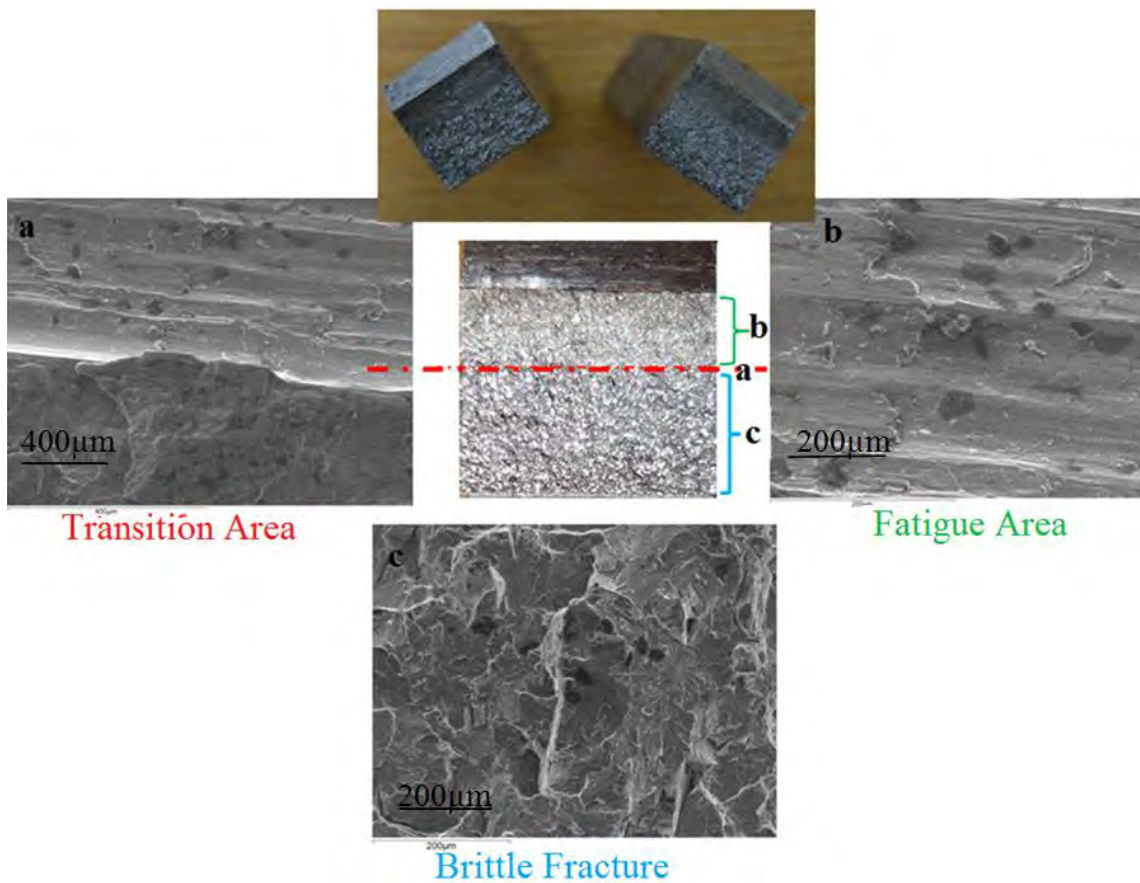


Figure 61 Images of the fractured surface of a four point bending sample

One of the pre-cracked four point bending samples was overloaded on purpose to examine the nature of AE activity during final failure. It can be seen in Figure 62 that various hits of low and high amplitude are recorded.

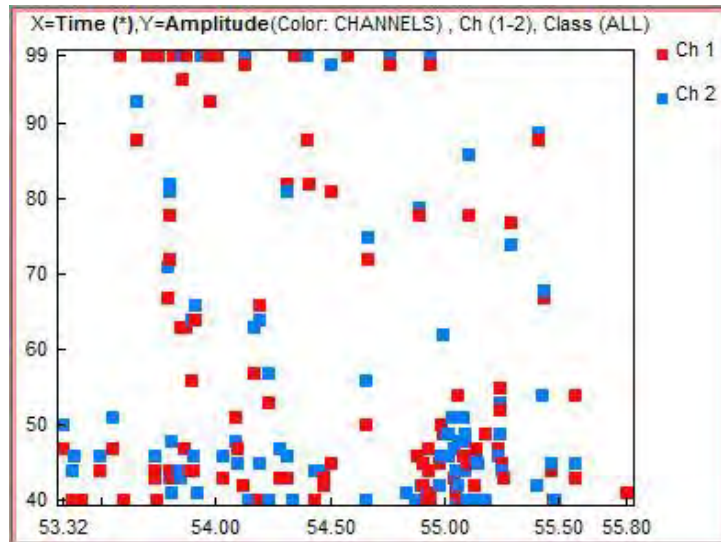


Figure 62 Amplitude with time for overloaded four point bending sample

Figure 63 shows the hit distribution with amplitude level per sensor. It can be seen that most hits are recorded at low amplitude with several also being recorded at the maximum amplitude range (i.e. 99dB). This is an interesting finding since it indicates that both low and high amplitude AE events are present during final failure and rapid crack growth.

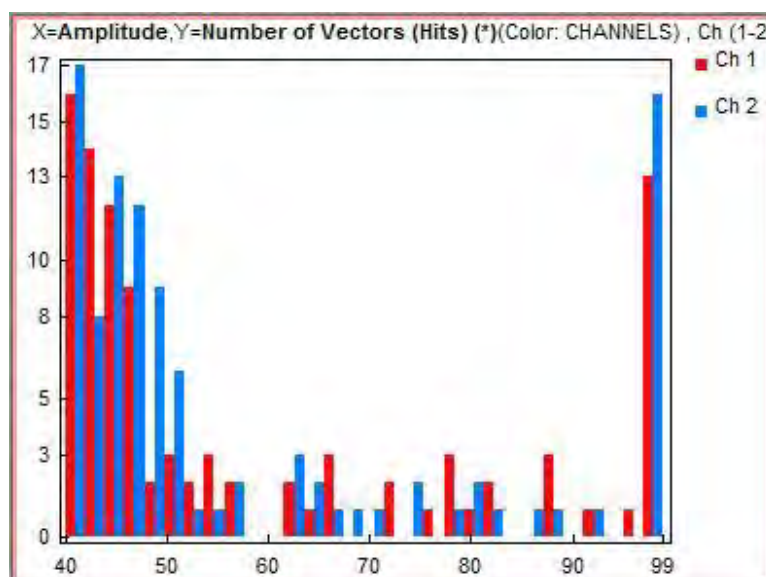


Figure 63 Distribution of hits with amplitude per sensor for rapidly broken four point bending sample

The plot in Figure 64 is in agreement with the results reported earlier, i.e. that the duration of the hit increases as the hit amplitude becomes larger.

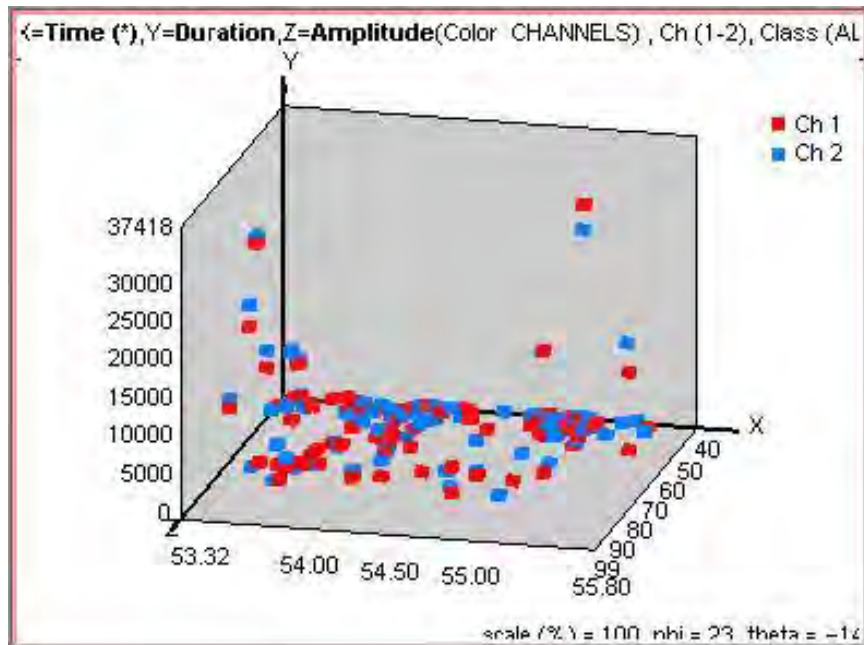


Figure 64 Hit amplitude and duration with test time per sensor

In Figure 65, the peak frequency of the hits recorded varies significantly although all the AE activity recorded is entirely due to the rapid propagation of the crack and subsequent failure of the sample.

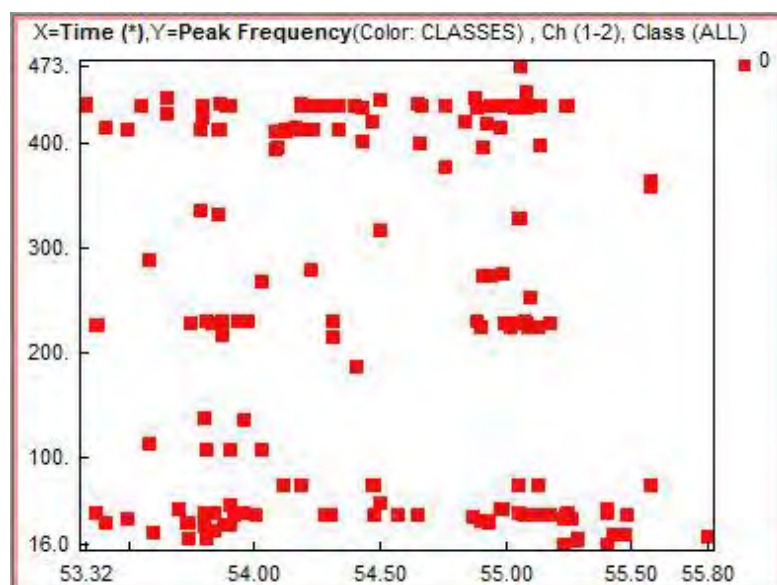


Figure 65 Hit peak frequency with test time

The plot in Figure 66 shows the hit duration with test time. It can be seen that several of the hits recorded have long duration indicating intense crack growth.

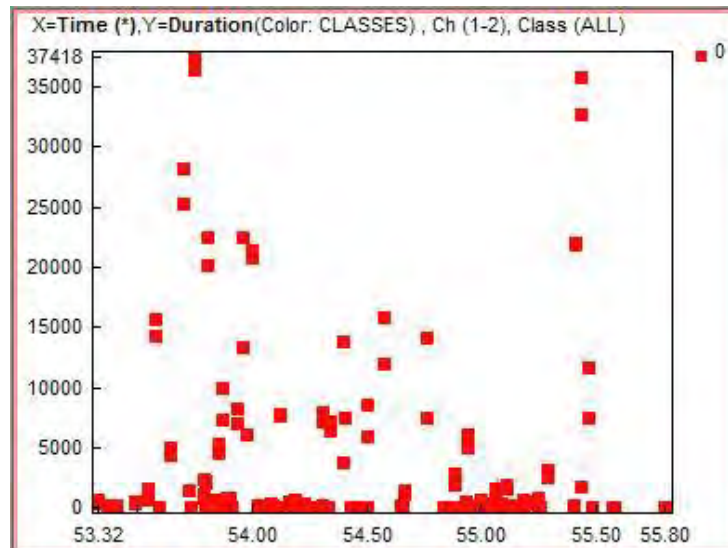


Figure 66 Hit duration with test time for rapidly broken four point bending sample

It can be safely concluded that it is possible with AE to identify the burst-type waveforms associated with crack growth under laboratory condition. Similar burst-type waveforms are expected in the field if a crack is growing in a rail. The question that remains to be answered is whether the background noise from passing rolling stock will be high enough to mask the AE events related to crack growth. Simulated tests discussed in the following chapter indicate that rolling noise may be low enough to at least detect successfully high amplitude AE events related to crack growth. Also in the case that background noise is masking AE events related to crack growth suitable analysis techniques should be developed.

## 6 Experiments under simulated field conditions

### 6.1 Experimental setup

In the field AE is expected to be affected by rolling noise produced from the wheels. Nonetheless, provided that the wheels are free of defects such as flats, metal build-up or rubbing flange then high-amplitude AE events due to crack growth are likely to be detectable even with the rolling noise present. It is also important to recognise the influence of the amplification level employed. Therefore it may be useful to employ several sensors with different gains during such tests to avoid saturation of the signal from rolling noise.

A customised four-channel AE system produced by Feldman Enterprises Limited was used for these tests. One PAC AE wideband sensor with a bandwidth of 100 kHz-1MHz was employed in this case. The signal was initially amplified by a PAC pre-amplifier. An amplifier was used for further amplification of the signal before it was recorded using an Agilent 2531A data acquisition card. The Agilent 2531 data acquisition card has a maximum sampling rate of  $2 \times 10^6$  samples per second and can support simultaneously up to 4 channels at 500kS/s, The data acquisition rate was set at 500 kHz and data were recorded for duration of 5-10 seconds depending on the test. Acquired data during testing were logged by a PC using a customised software data logger also provided by Feldman. AE data acquired were analysed using Feldman's PCM software. Figure 67 shows the experimental configuration employed.

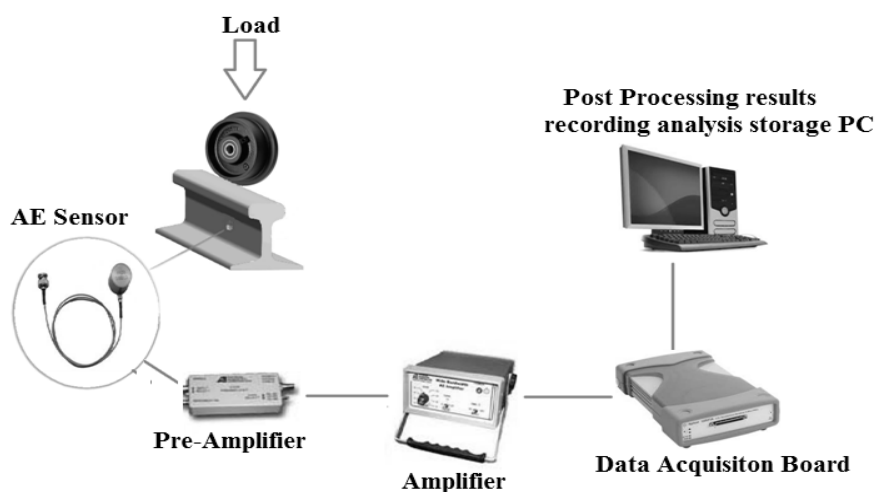


Figure 67 Experimental configuration for simulated AE tests

## 6.2 Manual inspection

During initial tests a single laboratory-sized wheel (0.16m diameter) was rotated manually on a small section of rail as shown in Figure 68

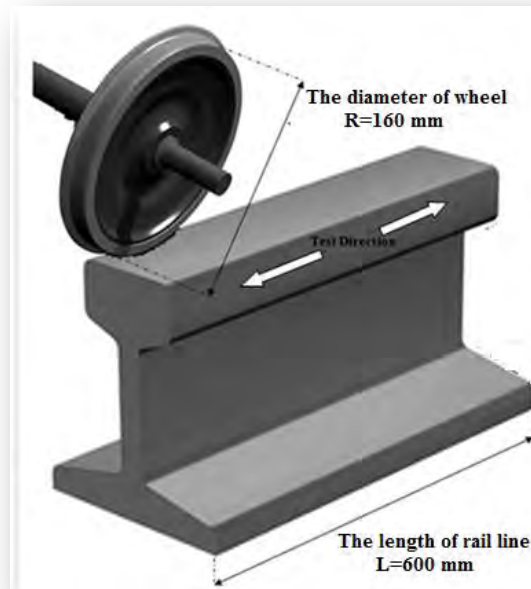


Figure 68 Simplified schematic showing the test concept.

The photograph shows the AE equipment used during tests in Figure 69.

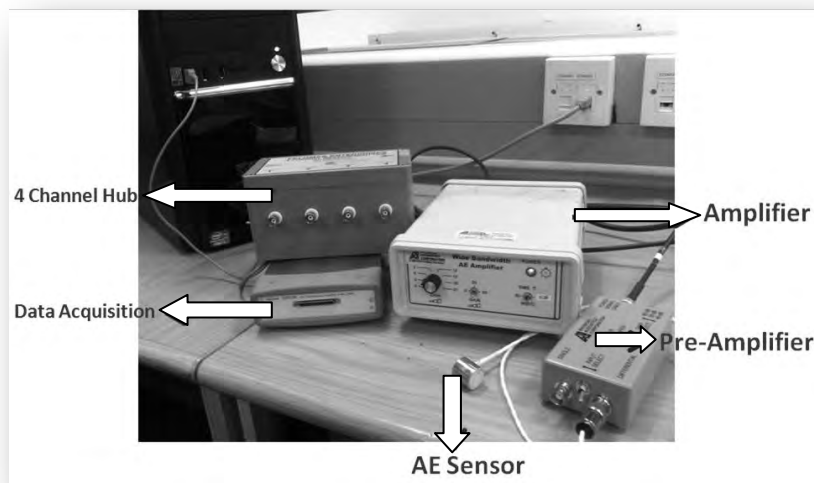


Figure 69 Equipments used in experiment

The average wheel moving speed during manual tests was 1 m/s. The AE sensor was coupled on the rail using grease and kept in place under constant load using a magnetic hold-down.

The test wheel did not contain any surface problems. A burst-type AE event similar to that generated by crack growth was simulated experimentally by breaking a pencil lead tip. The pencil break tip simulates well burst type AE signals and is widely accepted by the scientific community as a means of calibrating the sample. Pencil breaks were executed at various distances from the location of the piezoelectric sensor with excellent results.

Figure 70 shows the raw AE waveform associated with rolling noise from the wheel using very low gain (23dB). The associated moving RMS plot is shown on the right.

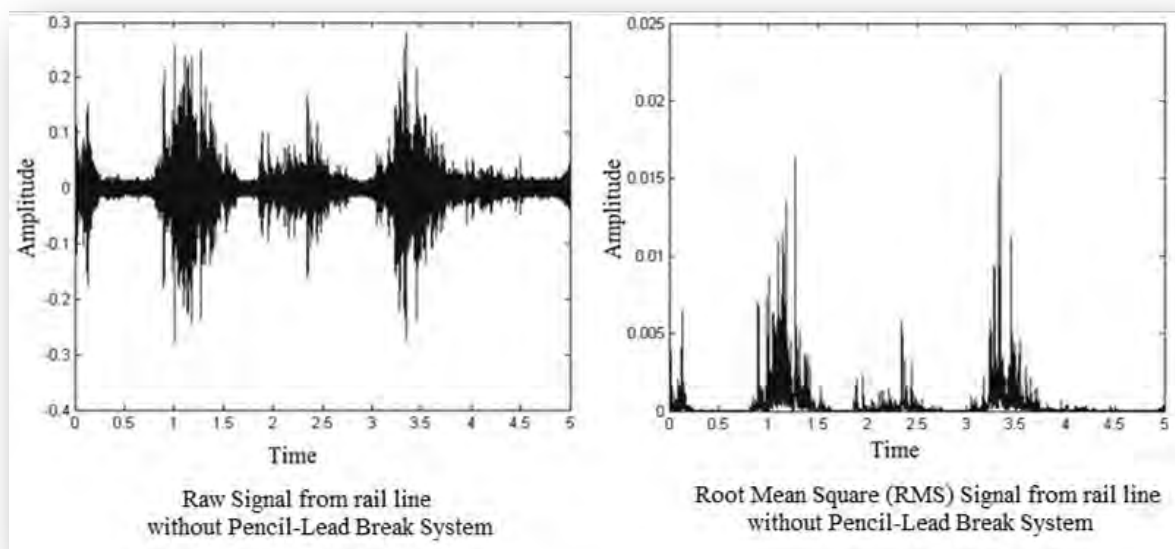


Figure 70 Raw AE waveform associated with rolling noise and moving RMS

During testing, the pencil tip was broken on the rail while the wheel was manually rolled on the rail section as shown in the photograph Figure 71.



Figure 71 The indication of the second experimental technique at the laboratory conditions

A pencil break event without any rolling noise and associated RMS is shown in Figure 72. The test has been carried out using an overall amplification of 52dB.

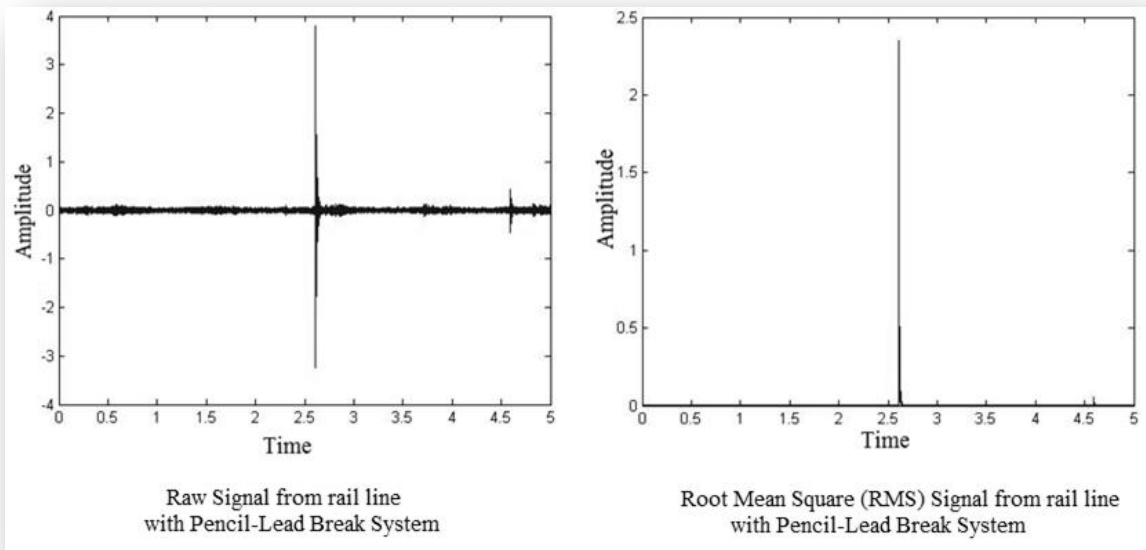


Figure 72 Raw AE signal from a pencil break and associated RMS.

Below is the raw AE data after a repetition test showing in Figure 73 some more intense background noise but the pencil break is clearly visible. The amplification gain remained constant at 52dB.

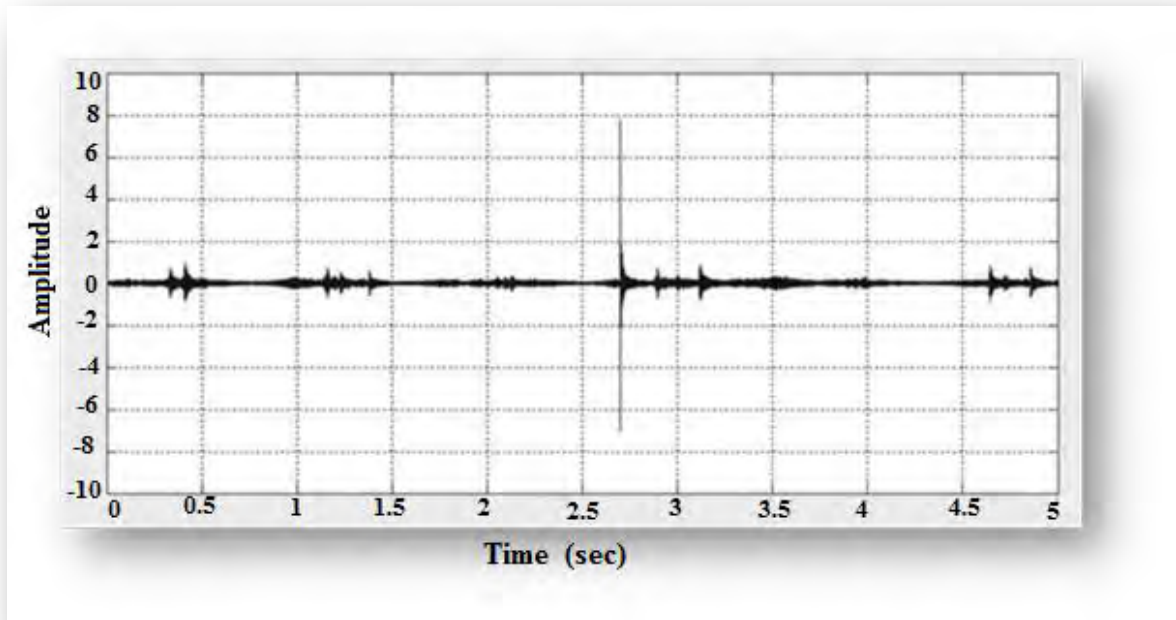


Figure 73 Repetition test with rolling noise present. The pencil break simulating the crack growth event is clearly visible

In the next image (Figure 74), the pencil break amplitude is still visible at 2.1s but some background noise peaks due to occasional contact of the flange with the rail as the wheel rotates also reach similar amplitude to the peak generated by the pencil break. This shows that wheel defects, such as rubbing flange or wheel flats can contaminate the signal significantly. In this case alternatively filtering techniques will need to be investigated.

Also the master-slave technique should also be considered. In this case the master AE sensor near the defects is guarded by slave or guard sensors which can potentially eliminate external noise from rolling stock. However, this could be extremely difficult to apply on a rail due to the proximity of the defect from the rolling noise while the loading axle passes over it.

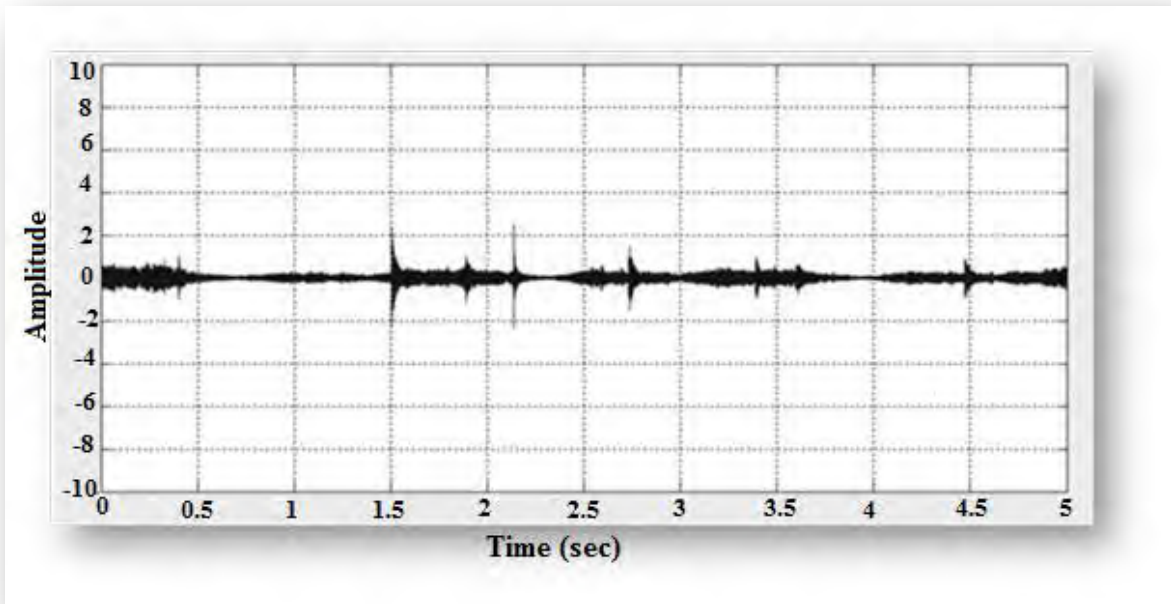


Figure 74 Contaminated signal from occasional contact of the wheel flange giving rise to occasional high amplitude peaks that resemble the one arising from the pencil break... The pencil break is visible at 2.1s.

### 6.3 Simulated trials using a motorised trolley

Further tests were carried out using a motorised rail trolley that has been developed by researchers at the Birmingham Centre for Railway Research and Education (BCRRE). The motorised rail trolley is shown on the photograph of Figure 75. On the front of the trolley an extra wheel similar to the one used for the manual tests was also installed. Tests were carried out on the 7m long Birmingham University's test track located outside the BCRRE laboratory at Gisbert Kapp Building. The rail trolley was pushed manually as well moved along the track using its electric motor. No significant variations were seen in the results of the manual and automated tests. With this experimental configuration it was possible to simulate even better the effect of rolling stock noise on the AE measurement.

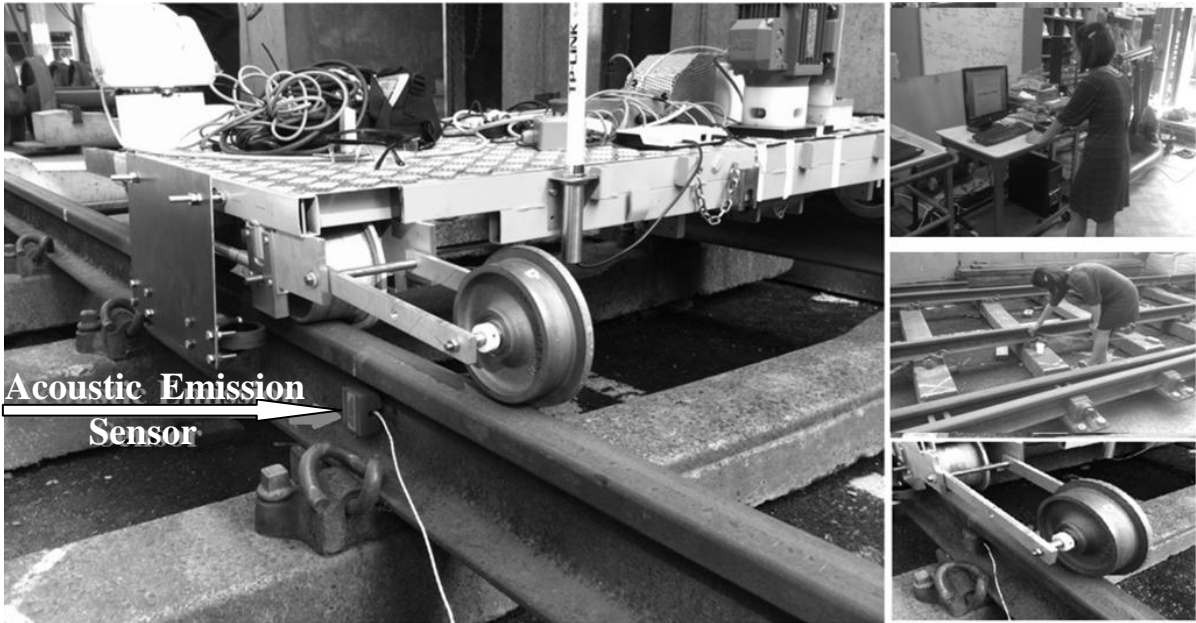


Figure 75 Experimental configuration on the test rail track at University of Birmingham

The test trolley was run at a maximum speed of 3km/h due to the restricted length of the rail track. The recorded raw AE signals and RMS with the pencil break event present are shown in Figure 76.

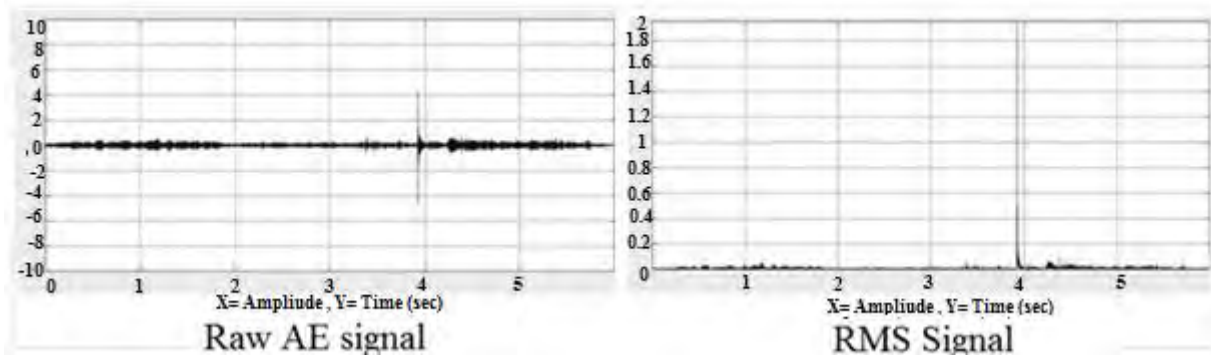


Figure 76 Raw AE signal and RMS with clearly visible pencil break event simulating a crack growth event. Gain is set at 58dB

The plot in Figure 77 shows the resulting FFT spectrum of the raw data arising from the pencil break. The nature of the FFT spectrum can be used to reveal whether the arising AE signal is related to a damage event or from noise.

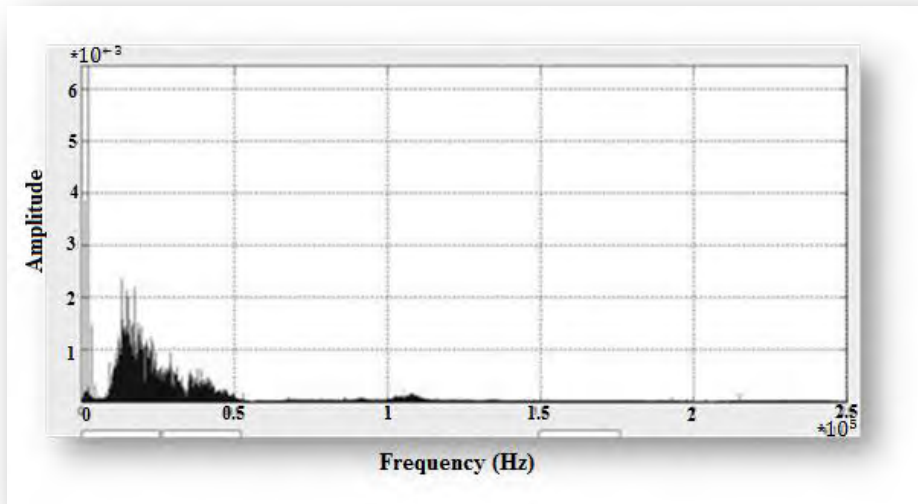


Figure 77 FFT of the raw AE signal arising from the pencil break event.

Tests were also carried out using the electric motor of the trolley to move it along the track automatically during the AE tests to see whether the background noise would vary. As can be seen in Figure 78, it was found that during these tests the background noise was more consistent during the test but its overall amplitude was similar to that recorded for the manual tests. The amplification gain was set slightly higher for these tests at 61dB. The peak generated by the pencil break used to simulate a crack growing is clearly seen at 7.5s.

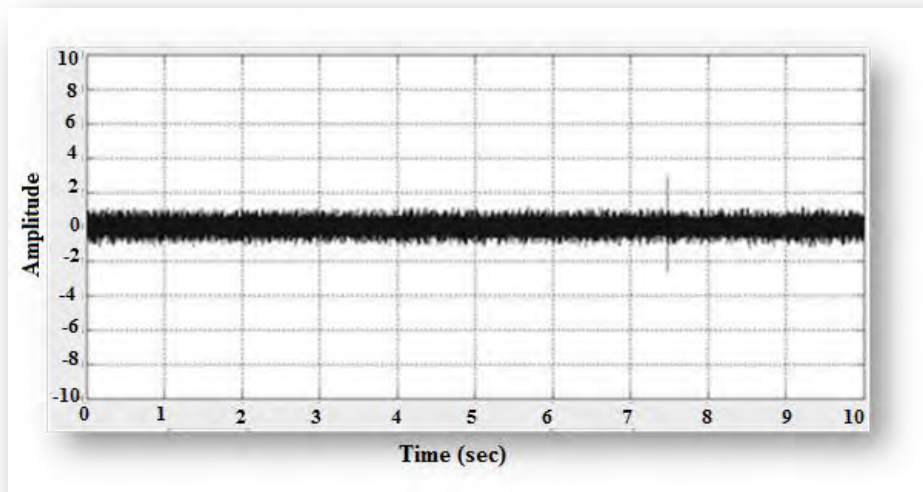


Figure 78 Raw AE signal with pencil break showing at 7.5s during automatic movement of the trolley.

## 7 Conclusions and future work

The results reported in this thesis show that it is possible to clearly identify the nature of waveforms related to crack growth in rail steel. Three-point and four-point fatigue bending experimental setups were selected as more appropriate testing configurations for simulating the cyclic loading conditions that rails sustain while they are in-service.

In order to minimise the effect of the background noise from the machine and thus the load required to cause crack propagation, the samples used had a relatively small cross-section. A trapezoidal loading pattern was used as most appropriate for this type of tests. Also a pico wideband AE sensor from PAC was selected to monitor AE activity as these sensors are less sensitive than normal-sized wideband sensors.

Although this means that some lower amplitude AE events arising from crack growth may have been missed on the other hand those that have been recorded are predominantly due to crack growth. Very few hits that have been recorded are related to machine noise, particularly in 4-point tests. Moreover, the machine noise hits appear to have lower amplitudes and lower durations.

This has enabled the definite identification and evaluation of the waveforms arising from crack growth in rail steel. Some differences were observed between 3-point and 4-point bending AE results. In 3-point bending tests the tests have been slightly noisier although the hits related to machine noise have remained within low amplitude levels as in 4-point bending tests.

Although in 3-point bending tests the recorded hit rate increased as crack propagation accelerated this was not so evident in 4-point bending tests, perhaps due to the lower duration of the tests. The amplitude of the acoustic emission signals recorded also increased as crack neared to its critical size. The final failure was followed by a large number of recorded hits with amplitudes that ranged from 40dB to 99dB in all cases.

Furthermore it has been shown that wheel related rolling noise may not be a barrier for the detection of crack growth in the field. Initial tests have shown that AE is a promising technique for the detection of crack growth in defective in-service rails. The level of

amplification is likely to be of critical importance and therefore variable gain and use of multiple sensors may be needed in the field under actual operational conditions to increase the usefulness of the data obtained. For these tests normal-sized wideband sensors have been used as the waveform from crack growth events has been clearly identified from the bending experiments.

The signal processing of acquired AE waveforms need to be researched further to develop suitable filtering techniques in cases where AE waveforms related to crack growth have similar amplitude to that of background noise produced by wheel rolling.

At the moment the RMS of the raw waveform as well as its Fast Fourier Transform appear to be suitable for analysis of AE signals. Particularly at freight lines where rolling conditions will be similar to those simulated, i.e. relatively lower background noise levels due to lower speeds as well as number of motorised axles, it is expected that the form of analysis employed herewith could enable the detection of crack growth related events. Especially, for high amplitude crack growth events the related acoustic emission signal may even be visible within the raw data.

Future work should focus on establishing the exact data acquisition parameters that enable minimisation of background noise effects and increase the likelihood of identifying acoustic emission signals related purely to crack growth events.

Further research is required in the field of waveform analysis in order to establish the optimum filtering algorithms so as to remove unwanted background noise effects on acoustic emission signals related to crack growth events. Further tests should be carried out on rails which have been identified to contain 1A and 1B defects.

It is likely that the data acquisition in the field should be supported by information related to the exact location and time of the loading axles as they go over the defect and load it repeatedly. This will probably require work to be carried out on the system electronics and data processing methodology. Ideally tests should be carried out on the same defects prior to clamping as well as after clamping in order to clearly identify the effect of the clamping on the acoustic emission signals recorded. The Kaiser and Felicity effects after clamping should also be taken into account during tests in the field.

Finally, during field tests the master-slave technique, where the master sensor is mounted near the defect and surrounded by slave or guard sensors which eliminate noise that is generated from outside the area of interest should also be investigated as a potential means for eliminating external noise arising from the wheel-rail interface.

## 7.1 Word Count

There are 15350 words between sections 1 and section 7.

## References

- Anderson, T. (1995). *Fracture mechanics: Fundamentals and Applications*. Texas: CRC Press.
- Beden, S., Abdullah, S., & Ariffin, A. (2009). Review of Fatigue Crack Propagation Models for Metallic Component. *EuroJournal* , 28, 364-397.
- Bhadeshia, H. (2002). Steels for Rails. *Encyclopedia of Materials Science and Technology* , 1-7.
- Callister, W. D. (2006). *Materials Science Engineering An Introduction*. Utah: John Wiley & Sons, Inc.
- Chaswal, V., Sasikala, G., Ray, S., Mannan, S., & Raj, B. (2004, December 16). Fatigue crack growth mechanism in aged 9Cr–1Mo steel: threshold and Paris regimes. Kalpakkam, India.
- Davis, C. (2003, May). Modelling and Detecting Damage (Wear and RCF) in Rails. Birmingham, United Kingdom.
- Department for Transport (DfT). (2011, February). High Speed Rail: Investing in Britain's Future Consultation. London, United of Kingdom. Retrieved August 31, 2012, from Department for Transport.
- Diener, M. (2009, December 9). Corrosion in the rail environment. Hellemmes, France.
- European Commission. (2011, October 19). Regulation of the European Parliament and of the Council. Brussels.
- Ewalds, H., & Wanhill, R. (1989). *Fracture Mechanics*. London: Edward Arnold.
- Han, Z., Luo, H., & Wang, H. (2011). Effects of strain rate and notch on acoustic emission during the tensile deformation of a discontinuous yielding material. *Materials Science and Engineering* , 528 (13-14), 4372-4380.
- Hertzberg, R. W. (1976). *Deformation and Fracture Mechanics of Engineering Materials* (1st ed.). United States of America: John Wiley&Sons.
- HM Treasury Infrastructure UK. (2010). *Infrastructure Cost Review*:. London: HM Treasury Infrastructure UK.
- Huang, M., Jiang, L., Liaw, P. K., Brooks, C. R., Seeley, R., & Klarstrom, D. L. (1998). Using Acoustic Emission in Fatigue and Fracture Materials Research. Knoxville, Tennessee, United States of America: Jom-e.

- Husin, S., Mba, D., & Hamzah, R. R. (2010). Viability of the Application of Acoustic Emission Technology for the Process and Management of Maintenance in Industries: Defect Detection, On-Line Condition Monitoring, Diagnostic and Prognostic Tools. *International Multiconference of Engineers and Computers Scientists* (pp. 1698-1706). Hong Kong: IMECS.
- Labossiere, P. E., Flores, D., & Vant, C. (2007). *Fracture - ME354a Lecture Notes*. Washington: University of Washington.
- Lehtonen, A., Cosgrove, J., Hudson, J., & Johansson, E. (2012). An examination of in situ rock stress estimation using the Kaiser effect. *124*, 24-37.
- Liu, Y., Stratman, B., & Mahadevan, S. (2005). Fatigue crack initiation life prediction of railroad wheels. Nashville: Vanderbilt University.
- Mechanics and Materials Laboratory. (2008). *Bending Test- Tensile Strength*. Selangor: Universiti Tenaga Nasional.
- Mistras Group Inc. (2009). *AEwin Software User's Manual Rev 3*. New Jersey, USA: Mistras Group Inc.
- Papaelias, M. (2011). *Internal Report on Strategies for Rail Inspection*. Birmingham: Centre for Railway Research and Education, University of Birmingham.
- Papaelias, M., Davis, C., Roberts, C., Blakeley, B., & Lugg, M. (2012). INTERAIL: Development of a Novel Integrated Inspection System for the Accurate Evaluation of the Structural Integrity of Rail Tracks – Implementation of the ACFM Rail Inspection Module. Birmingham, United Kingdom.
- Papaelias, M., Roberts, C., & Davis, C. (2008). A review on non-destructive evaluation of rails: state-of-the-art and future development. *Proceedings of the Institution of Mechanical Engineers, Part F: Journal of Rail and Rapid Transit* , 367-384.
- Pereira, H. F., Jesus, A. M., Ribeiro, A. S., & Fernandes, A. A. (2008). Influence of Loading Sequence and Stress Ratio on Fatigue Damage Accumulation of a Structural Component. *20* . Porto, Portugal.
- Pollock, A. A. (2003). Acoustic Emission Inspection, Technical Report. Cambridgeshire, UK: MISTRAS Holding Group- Physical Acoustic Limited.
- Railway Group Standard, Railtrack PLC. (1998, December). Track Standards Manual Section 2: Rails. London, United Kingdom.
- Reddy, V. (2007). Development of an integrated model for assessment of operational risks in rail track. Brisbane, Australia.
- Smith, R. A. (2002, April). Rolling Contact Fatigue of rail: Review of current understanding. London, United Kingdom.

Steinzig, M. (2000). *Bend Tests of Silicon Ladders to Determine Ultimate Strength*. The Gamma Ray Large Area Space Telescope. Los Alamos: HYTEC Incorporated.

University of Birmingham. (2007). *D4.4.1- Rail Inspection Technologies*. Birmingham: Innotrack.

Vallen System. (2004). *The Use of the Acoustic Emission Technique for Material Research and Structural Integrity Monitoring*. Munich: Vallen Systeme.

Vallen Systeme GmbH. (2002). *AE Testing (AT) Fundamentals- Equipment-Data Analysis (Overview)*. Munich, Germany: Vallen Systeme GmbH.

Vitez, I., Krumes, D., & Vitez, B. (2004, August). UIC Recommendations for the use of rail steel grades. Slavonski Brod, Croatia.

## Website Links

Cyberphysics. (Unknown). *The Young Modulus (E) - the modulus of elasticity*. Retrieved February 05, 2012, from [http://www.cyberphysics.co.uk/topics/forces/young\\_modulus.htm](http://www.cyberphysics.co.uk/topics/forces/young_modulus.htm)

DoITPoMS. (2008, January). *The Ductile-Brittle Transition, Yield Strength and Ductility*. Retrieved August 04, 2012, from Dissemination of IT for the Promotion of Materials Science: <http://www.doitpoms.ac.uk/tlplib/BD6/yield.php>

Hocking NDT Ltd. (2012, May 3). *Rail Inspection The Eddy Current Solution*. Retrieved August 4, 2012, from Krautkramer: <http://www.krautkramer.com.au/Eddy%20Current%20Rail%20Inspection.pdf>

International Atomic Energy Agency. (2000). *Liquid Penetrant and Magnetic Particle Testing at Level 2*. Vienna, Austria: IAEA. Retrieved from <http://www-pub.iaea.org/MTCD/publications/PDF/TCS-11.pdf>

International Union of Railways (UIC). (2011, November 30). *UIC and Network Rail Statistics*. Retrieved March 22, 2012, from Finance: <http://www.uic.org/spip.php?rubrique840>

James, M. N. (2001). *Griffith Theory*. Retrieved February 12, 2012, from [http://www.tech.plym.ac.uk/sme/interactive\\_resources/tutorials/fracturemechanics/Griffith/GriffTheory1.htm](http://www.tech.plym.ac.uk/sme/interactive_resources/tutorials/fracturemechanics/Griffith/GriffTheory1.htm)

Mesteel. (Unknown). *Micro Alloyed UIC 60 Rails Technical Specifications for Acquisition*. Retrieved August 4, 2012, from Middle East and Steel Statistics: [www.mesteel.com/attachments/oi\\_6976\\_1.doc](http://www.mesteel.com/attachments/oi_6976_1.doc)

NDT Education Resource Center. (2001-2012). *Introduction to Acoustic Emission Testing*. Retrieved August 4, 2012, from NDT Resource Center: [http://www.ndt-ed.org/EducationResources/CommunityCollege/Other%20Methods/AE/AE\\_Intro.htm](http://www.ndt-ed.org/EducationResources/CommunityCollege/Other%20Methods/AE/AE_Intro.htm)

Roylance, D. (2001, June 14). *Introduction to Fracture Mechanics*. Retrieved August 03, 2012, from Massachusetts Institute of Technology Open Course Ware: <http://ocw.mit.edu/courses/materials-science-and-engineering/3-11-mechanics-of-materials-fall-1999/modules/frac.pdf>

Texas Tech University. (2012). *Bending Process*. Retrieved 02 10, 2012, from <http://www.me.ttu.edu/ME/Research/advanced/materialsperformance/projects/residualstress/progress/bending>

The University of Southern Mississippi. (2001, September 9). *Introduction to Materials Science and Engineering, MatE 272, Lecture 13&14*. Retrieved August 6, 2012, from School of Polymers and High Performance Materials: [http://www.psrc.usm.edu/org/Courses/mate\\_272/](http://www.psrc.usm.edu/org/Courses/mate_272/)